Unlocking the Imaging Capabilities of Synthetic Aperture Radar Altimetry for Ocean Applications

Altiparmaki, O.

DOI
10.4233/uuid:864fbfef-38f0-4874-bac7-20b99d491e31

Publication date
2025

Document Version
Final published version

Citation (APA)
Altiparmaki, O. (2025). *Unlocking the Imaging Capabilities of Synthetic Aperture Radar Altimetry for Ocean Applications*. [Dissertation (TU Delft), Delft University of Technology]. https://doi.org/10.4233/uuid:864fbfef-38f0-4874-bac7-20b99d491e31

Unlocking the Imaging Capabilities of Synthetic Aperture Radar Altimetry for Ocean Applications

Ourania Altiparmaki

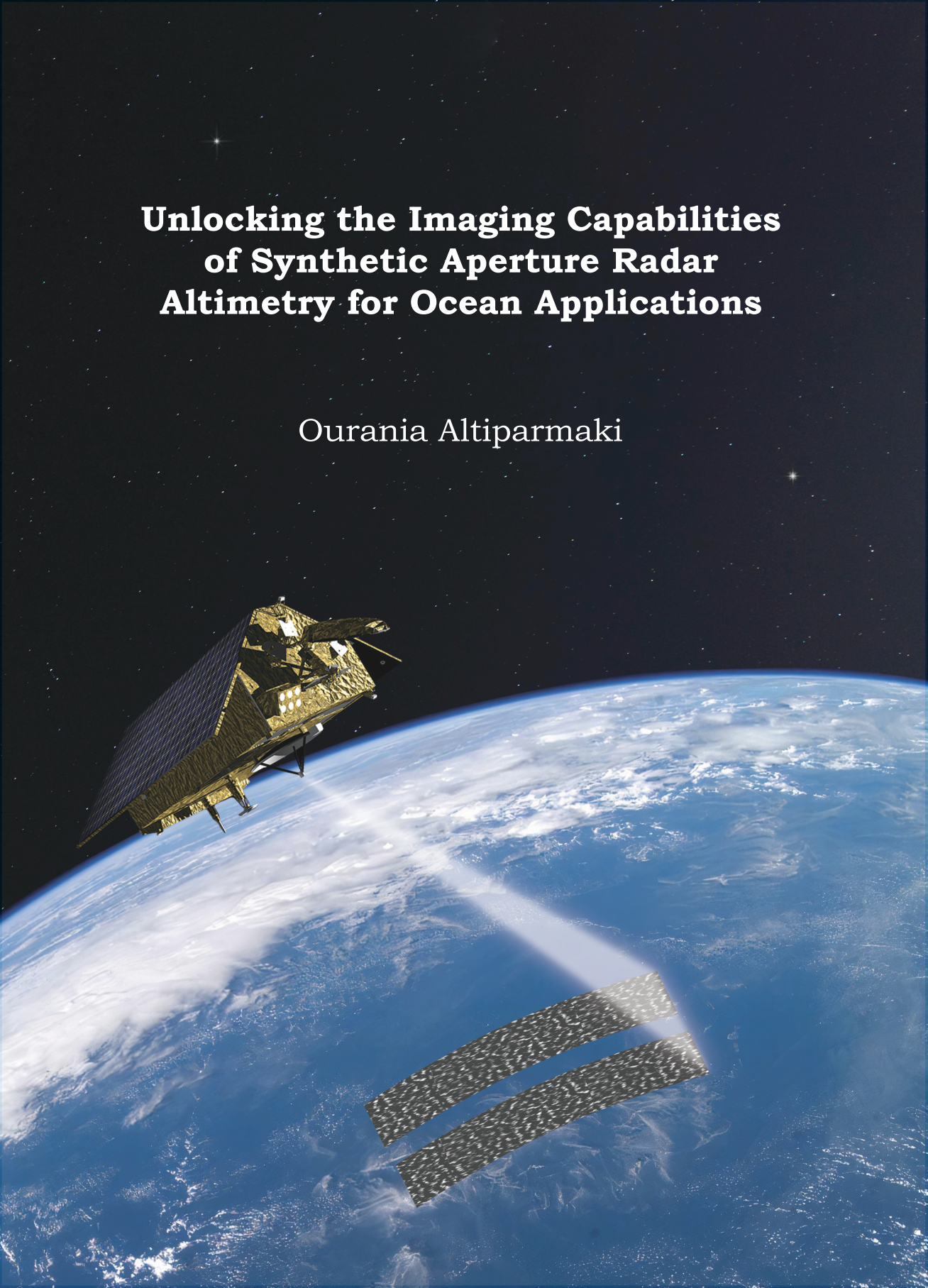

UNLOCKING THE IMAGING CAPABILITIES OF SYNTHETIC APERTURE RADAR ALTIMETRY FOR OCEAN APPLICATIONS

UNLOCKING THE IMAGING CAPABILITIES OF SYNTHETIC APERTURE RADAR ALTIMETRY FOR OCEAN APPLICATIONS

Dissertation

for the purpose of obtaining the degree of doctor
at Delft University of Technology,
by the authority of the Rector Magnificus, prof.dr.ir. T.H.J.J. van der Hagen,
chair of the Board of Doctorates,
to be defended publicly on Friday 11, July 2025 at 15:00 o'clock

by

Ourania ALTIPARMAKI

Master of Science in Rural and Surveying Engineering,
Aristotle University of Thessaloniki, Greece,
born in Mytilini, Greece

This dissertation has been approved by the promotors.

Composition of the doctoral committee:

Rector Magnificus	chairperson
Prof.dr.ir. P.N.A.M Visser	Delft University of Technology, *promotor*
Ir. M.C. Naeije	Delft University of Technology, *copromotor*
Independent members:	
Prof.dr. O.B. Andersen	DTU SPACE, Denmark
Dr. L. Aouf	Météo-France, France
Prof.dr. Ø. Breivik	University of Bergen, Norway
Dr. A. Egido	ESA/ESTEC, The Netherlands
Prof.dr.ir. F.C. Vossepoel	Delft University of Technology
Prof.dr. L.L.A. Vermeersen	Delft University of Technology, *reserve member*

Keywords: Synthetic Aperture Radar (SAR) altimetry, space oceanography, fully-focused SAR, wave imaging, swell waves, wave spectra, azimuth cutoff, wave orbital velocity, wave-current interactions, wave models

Printed by: Ipskamp Printing

Cover design: Constantine Karapanagiotis

ISBN: 978-94-6384-796-4 e-ISBN: 978-94-6518-067-0

An electronic version of this dissertation is available at
`http://repository.tudelft.nl/`.

Like waves shaping the shoreline,
slowly but persistently,
this PhD dissertation is
the result of years of movement;
sometimes steady, sometimes uncertain,
but always forward...

Ourania Altiparmaki
Delft, March 2025

Contents

Summary

As climate change continues to drive an increase in extreme weather events, the need for reliable predictions and observational data has never been more critical. Oceans, playing a vital role in regulating the Earth's climate, are central to understanding these changes. Specifically, accurately modeling ocean wave dynamics, i.e., how waves are generated, evolve, and interact with oceanic processes such as currents, helps track ocean circulation and predict future variations. Thanks to Earth Observation satellites, continuous global observations have been available over the past few decades. Satellite altimeters, active sensors utilizing radar's ranging capabilities, have emerged as pioneers in space oceanography. These instruments measure critical geophysical parameters such as sea surface height, significant wave height and near-surface wind speed along satellite tracks. Recognizing the immense value of these measurements for climate studies and operational activities, continuous technological innovations are essential for optimizing the performance and use of these instruments.

One major breakthrough in satellite altimetry was the incorporation of Synthetic Aperture Radar (SAR) technology in 2010, which enhanced spatial resolution from around 7 km, provided by Low-Resolution Mode sensors, to about 300 m. In 2017, the fully-focused coherent processing of pulse echoes was implemented, a concept widely used in SAR imaging, enabling meter-scale resolution. This improvement led to significant benefits in near-coast applications, improving the quality of geophysical parameters by reducing signal contamination from surrounding land features. Additionally, for the first time, off-nadir signals, previously considered a nuisance, were exploited to map narrow inland water bodies and detect sea-ice leads and floes. Recognizing this imaging potential led to investigating its capabilities over open oceans.

Existing challenges in conventional, or unfocused, SAR altimetry relate to the accuracy of significant wave height estimates, especially when long waves, known as swells, dominate the sea surface. Swell waves, with wavelengths exceeding 150 meters, are often too long to be fully captured within the SAR altimeter's footprint, leading to noisy, multi-peaked waveforms. Recognizing the interference of swell signals in SAR responses, combined with the high-resolution data provided by fully-focused processing, this dissertation first investigated the feasibility of transforming what was previously considered a nuisance into valuable information about the sea surface.

To achieve this, the identification of swell-induced power variations in off-nadir altimeter's signals, representing the so-called trailing edge of the returned echo, was first confirmed. These patterns were analyzed to compute a fully-focused modulation spectrum derived from altimetry. The modulation spectrum is a commonly used Level-2 product provided by satellites designed to measure the wave field, such as Sentinel-1 and CFOSAT, and allows for the estimation of swell characteristics, including wavelength, direction and wave height. The proposed method involved normalizing the signal intensity and

re-projecting the range bins to cross-track ground locations, followed by spectral analysis akin to side-looking SAR systems. The analysis revealed that fully-focused altimetry modulation spectra display power in all four quadrants due to the inherent 180-degree SAR ambiguity, plus two additional ambiguities caused by inseparable signals received from both sides of the radar footprint. The study also identified the main modulation mechanisms, using as reference numerical and analytical models. Range bunching was found to be a dominant mechanism alongside velocity bunching, with their relative strength highly dependent on the wave propagation angle. Fully-focused altimetry modulation spectra, derived from Cryosat-2, were evaluated through comparisons with buoy-derived directional wave spectra, showing good agreement. Furthermore, applying the proposed technique to Sentinel-6A data demonstrated that exploiting its full-beam footprint, which is partially truncated onboard for data volume efficiency, improves swell retrieval. This is particularly true for waves propagating in or near the cross-track direction, due to its extended observational window and higher resolution compared to the operational truncated data. Yet, the development of a method to invert modulation-derived spectra to real ocean wave spectra is necessary to reliably use these instruments as a new source for providing operational global swell observations.

The dissertation further explored the limitations of SAR altimeters in ocean wave imaging, focusing on resolution loss. This was addressed by estimating the azimuth cutoff wavelength, which serves as a proxy for the shortest detectable waves across different sea states and wave directions. The method used to estimate this parameter involved a SAR imaging technique applied in the spatial domain, minimizing residuals between the along-track autocorrelation function of fully-focused SAR radargrams, representing successive waveforms, and a fitted Gaussian function. Sentinel-6A data were then used to evaluate the method's performance through comparisons with model-derived values globally. The analysis revealed that the method performs well under the majority of sea states but tends to underestimate values in extreme wind wave conditions. Furthermore, sensitivity to swell presence was observed, leading to pronounced overestimations, with the magnitude of these errors influenced by the swell direction. To mitigate these errors, an alternative approach was developed in the wavenumber domain. Results revealed an improvement in the correlation between azimuth cutoff estimates and model-derived values by 10%. Given the strong relationship between resolution loss and sea state conditions, the azimuth cutoff was further used to derive a new sea-state parameter: the variance of wave orbital velocities. Wave orbital velocity statistics offer valuable insights into wave climate by isolating wave components associated with developing seas. Comparisons between modeled and estimated wave orbital velocity variances showed similar sensitivities to swell presence and high sea states, suggesting further refinement of the proposed methods. Despite these challenges, the ability to extract these two additional parameters from the radar signal is valuable for identifying sensors capabilities and providing a new geophysical parameter for oceanographic studies.

Lastly, the dissertation assessed the impact of wave-current interactions on wave products derived from both models and satellites, focusing on the Agulhas Current region, one of the most dynamic ocean environments. In situ wave measurements, collected during the One Ocean Expedition in 2023, in which the author participated, served as a reference for this study. The study first examined ocean current products. A clear underesti-

mation of surface current velocities exceeding 0.5 m/s was found for both the Mercator operational model and the altimetry-derived Globcurrent product, with Mercator showing greater variability. Next, wave products, both with and without these ocean current products included in their modeling, were validated. The ECMWF reanalysis v5, known as ERA5, consistently underestimated wave heights above 2.5 m, whereas the MFWAM, which is the Global Ocean Wave Analysis and Forecast system from Meteo-France, showed good agreement with in situ data. This discrepancy was attributed to the lack of ocean current forcing in ERA5, underscoring the need for refinement in areas dominated by currents. Customized MFWAM simulations, including and excluding current data, further supported this finding. MFWAM forced with Globcurrent aligned most closely with drifter measurements, outperforming the operational product that uses Mercator currents. Comparisons between satellite altimeter observations and drifters also showed good agreement in significant wave height, with clear evidence of current-induced wave height variations along satellite tracks. Additionally, a multi-mission analysis of swell-induced modulation spectra from Sentinel-1, CFOSAT and SAR altimeters demonstrated alignment with in situ data and between them, highlighting the potential for synergistic use of these instruments in operational oceanography and climate studies.

Samenvatting (in Dutch)

Naarmate klimaatverandering blijft leiden tot een toename van extreme weersomstandigheden, is de behoefte aan betrouwbare voorspellingen en waarnemingen nog nooit zo kritisch geweest. Oceanen, die een cruciale rol spelen in het reguleren van het klimaat van de aarde, staan centraal bij het begrijpen van deze veranderingen. Het juist modelleren van oceaangolven, d.w.z. hoe ze worden gegenereerd, evolueren en inwerken op andere oceaanprocessen zoals stromingen, helpt ons om de oceaancirculatie in kaart te brengen en toekomstige veranderingen te voorspellen. Dankzij aardobservatiesatellieten zijn afgelopen decennia continue wereldwijde waarnemingen beschikbaar gekomen. Satellietaltimeters, actieve sensoren die gebruikmaken van de afstandsmeting van radar, zijn pioniers op het gebied van ruimte-oceanografie. Deze instrumenten meten cruciale geofysische parameters zoals zeewaterhoogte (zeespiegel), significante golfhoogte, en windsnelheid nabij het oppervlak, langs het grondspoor van de satelliet. Het enorme belang van deze metingen voor zowel klimaatstudies als operationele activiteiten vereist voortdurende technologische innovaties om de prestaties en toepassingen van deze instrumenten te optimaliseren.

Een belangrijke doorbraak op het gebied van satellietaltimetrie was de opname van Synthetic Aperture Radar (SAR) technologie in 2010, waarmee de ruimtelijke resolutie werd verbeterd van ongeveer 7 km (gegeven door Low-Resolution Mode sensoren) naar ongeveer 300 m. In 2017 werd de volledig-gefocuste coherente verwerking van pulsecho's geïmplementeerd, een concept dat veel wordt gebruikt in SAR beeldvorming, waarmee resoluties op meterschaal mogelijk werden. Deze verbetering leidde tot aanzienlijke voordelen voor toepassingen langs de kust, door de kwaliteit van de geofysische parameters te verbeteren door signaalvervuiling te verminderen van omringende landkenmerken. Bovendien werd het voor het eerst mogelijk om off-nadir signalen, die voorheen als hinderlijk werden beschouwd, te gebruiken om smalle inlandse waterlichamen in kaart te brengen en zee-ijsschotsen en -scheuren te detecteren. Het besef van dit beeldvormingspotentieel leidde tot het onderzoeken van de capaciteiten ervan op open oceaan.

Bestaande uitdagingen in conventionele (ongefocuste) SAR-altimetrie hebben betrekking op de nauwkeurigheid van de schattingen van de significante golfhoogte, vooral wanneer lange golven, ook wel deining genoemd, het zee-oppervlak domineren. Deining, met golflengtes van meer dan 150 meter, is vaak te groot om volledig binnen de SAR-altimeter voetafdruk te worden vastgelegd, wat resulteert in aliasing van het signaal gekenmerkt door ruis en velen pieken. Dit proefschrift onderzocht eerst de haalbaarheid van het transformeren van wat eerder als hinderlijk werd beschouwd naar waardevolle informatie over het zeeoppervlak door in de SAR respons gebruik te maken van de interferentie van de deining met de hoge resolutie data die voortkomt uit de volledig-gefocuste SAR altimeter verwerkingstechniek.

Om dit te bereiken, werd eerst de identificatie van deining-geïnduceerde vermogens-

variaties in off-nadir signalen, die de zogenaamde achterrand van het gereflecteerde echo vertegenwoordigen, bevestigd. Deze patronen werden stap voor stap verwerkt, wat leidde tot de berekening van een volledig-gefocuste altimetrie-modulatiespectrum. Een modulatiespectrum is een veelgebruikt level-2 product van satellieten die gericht zijn op het meten van het golfveld, zoals Sentinel-1 en CFOSAT, en maakt het mogelijk om de kenmerken van deining, zoals golflengte, richting en hoogte, te schatten. De voorgestelde methode omvatte het normaliseren van de signaalintensiteit en het herprojecteren van range bins naar cross-track grondlocaties, gevolgd door spectrale analyse, vergelijkbaar met die doorgaans toegepast wordt op side-looking SAR-systemen. De analyse toonde aan dat volledig-gefocuste altimetrie-modulatiespectra vermogenspieken vertonen in alle vier kwadranten vanwege de inherente 180-graden SAR-ambiguïteit, plus twee extra ambiguïteiten veroorzaakt door onscheidbare signalen die van beide zijden van de radarvoetafdruk worden ontvangen. De studie identificeerde ook de belangrijkste modulatiemechanismen, met behulp van numerieke en analytische modellen als referentie. “Range bunching” werd geïdentificeerd als een dominant mechanisme naast “velocity bunching”, waarbij hun relatieve sterkte afhankelijk is van de hoek die het goffront maakt met de richting van het grondspoor van de satelliet. Volledig-gefocuste altimetrie-modulatiespectra, afgeleid van Cryosat-2 metingen, werden geëvalueerd door te vergelijken met door boeien afgeleide directionele golfspectra: deze bleken goed overeen te komen. Verder toonde toepassing van dezelfde techniek op Sentinel-6A metingen aan dat het gebruik van de volledige bundelvoetafdruk, die normaal aan boord is afgekapt voor data volume efficiëntie, een uniek voordeel biedt bij het extraheren van deining. Dit geldt met name voor golven die zich in of nabij de cross-track richting van het satelliet grondspoor voortplanten, vanwege het verlengde observatievenster en de hogere resolutie in vergelijking met de operationele afgekapte gegevens. Toch is de ontwikkeling van een methode om modulatieafgeleide spectra te inverteren naar echte oceaangolfspectra noodzakelijk om deze instrumenten betrouwbaar te kunnen gebruiken als een nieuwe bron voor het verkrijgen van wereldwijde operationele deiningwaarnemingen.

Het proefschrift onderzocht vervolgens de beperkingen van SAR-altimetrie in oceaangolfbeeldvorming, met de nadruk op resolutieverlies. Dit werd aangepakt door de afkapgolflengte te schatten; deze fungeert als een proxy voor de kortst detecteerbare golflengten over verschillende zeecondities en golfrichtingen. De gebruikte methode om deze parameter te schatten, was een SAR-beeldvormingstechniek die werd toegepast in het ruimtelijke domein, waarbij verschillen werden geminimaliseerd tussen de langs-track autocorrelatiefunctie van volledig-gefocuste SAR radargrammen, die opeenvolgende golfvormen vertegenwoordigen, en een gefitte Gaussiaanse functie. Sentinel-6A gegevens werden vervolgens gebruikt om de prestaties van deze methode wereldwijd te evalueren door te vergelijken met model-afgeleide waarden. De analyse toonde aan dat de methode goed presteerde onder de meeste zeecondities, maar de waarden in extreme windgolfomstandigheden onderschatte. Bovendien werd gevoeligheid voor de aanwezigheid van deining waargenomen, wat leidde tot duidelijke overschattingen, waarvan de omvang werd beïnvloed door de richting van de deining ten opzichte van het azimut van de satelliet. Om deze fouten te verminderen, werd een alternatieve benadering ontwikkeld in het golfgetaldomein. De resultaten toonden een verbetering van 10% in de correlatie tussen azimutafkapschattingen en model-afgeleide waarden. Gezien de sterke relatie tussen resolu-

tieverlies en zee-condities, werd de azimut-afkap verder gebruikt om een nieuwe zee-statusparameter af te leiden: de variantie van golforbitale snelheden. Statistiek van golforbitale snelheid biedt waardevol inzicht in het golfklimaat door golfcomponenten te isoleren die verband houden met ontwikkelende zee-golven. Vergelijkingen tussen gemodelleerde en geschatte variaties in golforbitaalsnelheid toonden vergelijkbare gevoeligheden voor de aanwezigheid van deining en hoge zeecondities aan, wat aangeeft dat verdere verfijning van de ontwikkelde methoden nodig is. Ondanks deze uitdagingen is de vaardigheid om deze twee aanvullende parameters uit het radarsignaal te extraheren waardevol, omdat het helpt de sensorcapaciteiten te identificeren en zo een nieuwe geofysische parameter voor oceanografische studies kan bieden.

Tenslotte evalueerde het proefschrift de invloed van de interacties tussen golven en stromingen op golfproducten, zowel afkomstig van modellen als van satellieten, met als aandachtsgebied het Agulhasstroomgebied, één van de meest dynamische oceaanomgevingen. In-situ golfmetingen, verzameld tijdens de One Ocean Expedition in 2023, waaraan de auteur heeft bijgedragen, werden gebruikt als referentie voor de studie. Het begon met de evaluatie van oceaanstromingen-producten, waarin een duidelijke onderschatting van oppervlaktestroom snelheden van meer dan 0,5 m/s werd gevonden voor zowel het Mercator operationele model als het altimetrie-afgeleide Globcurrent-product, waarbij Mercator een hogere variabiliteit vertoonde. Vervolgens werden oceaangolfproducten gevalideerd, zowel met als zonder de invloed van oceaanstroomproducten in hun modellering. Het ECMWF heranalyse v5 model, bekend als ERA5, onderschatte consequent golfhoogtes boven de 2,5 m, terwijl het MFWAM model, het Global Ocean Wave Analysis and Forecast-systeem van Meteo-France, goede overeenstemming vertoonde met de in-situ gegevens. Deze discrepantie werd toegeschreven aan het ontbreken van oceaanstromingsforcering in ERA5, wat de noodzaak benadrukt om het product te verfijnen in gebieden waar stromingen domineren. Aangepaste MFWAM-simulaties, met stromingsdata en zonder, ondersteunden verder deze bevinding. MFWAM, wanneer aangestuurd met Globcurrent, kwam het dichtst bij de metingen van drifters en presteerde beter dan het operationele model dat Mercator-stromingen gebruikte. Vergelijkingen tussen satelliet-altimeter waarnemingen en drifters toonden ook een goede overeenstemming in de significante golfhoogte, met duidelijk bewijs van door de stroming geïnduceerde golfhoogte-variaties langs de satelliet grondsporen. Bovendien toonde een multi-missie-analyse van de deining-geïnduceerde modulatie spectrums van Sentinel-1, CFOSAT en SAR-altimetrie een sterke overeenstemming met in-situ gegevens en tussen de verschillende systemen, wat het potentieel benadrukt voor synergistische toepassing in operationele oceanografie en klimaatstudies.

1

Introduction

1.1 Background

Oceans play a critical role in regulating the Earth's climate and influencing weather patterns. Their dynamics are shaped by complex interactions between waves, currents, winds and tides, which vary across temporal and spatial scales. Monitoring these dynamics is crucial for understanding the changing climate, managing marine resources and ensuring maritime safety. The need for such monitoring has become increasingly urgent in recent decades as extreme events, such as tropical cyclones and storm surges, have become more frequent and severe due to climate change.

Satellite altimetry has significantly advanced the understanding of ocean dynamics by providing continuous, global measurements of sea surface height (sea level), significant wave height and near-surface wind speed along the satellites tracks [1]. The acquisition of these geophysical parameters is essential for tracking ocean circulation, assessing climate variability and monitoring long-term sea-level trends. Since the launch of Seasat [2], the first dedicated Earth-observing satellite equipped with a radar altimeter, by NASA in 1978, continuous technological advancements have expanded the applicability of satellite altimetry in Earth sciences. A major breakthrough occurred in 2010 with the launch of CryoSat-2, introducing Delay/Doppler or otherwise called Synthetic Aperture Radar (SAR) altimetry. By applying Delay/Doppler processing, SAR altimetry increased the along-track resolution down to approximately 300 meters, allowing the detection of finer ocean surface features [3].

In 2017, the fully-focused SAR concept [4] was introduced, refining along-track resolution even further, theoretically to the order of half the antenna length at approximately 0.5 m. This proved particularly beneficial in coastal altimetry, where returned signals are often contaminated by nearby land reflections. As shown by Schlembach *et al.* [5], fully-focused SAR data improves significant wave height observations near the coast, enabling reliable measurements at distances as close as 1-3 km from it. Moreover, this processing

technique expanded data acquisition capabilities over inland water bodies, enabling the estimation of water levels in small targets that were previously undetectable within the altimeters' field of view [6].

Beyond these advancements, fully-focused SAR altimetry has shown the potential to image ground targets by exploiting off-nadir signals, previously considered as nuisance. Regarding ocean targets, the only documented evidence of wave-like patterns was reported by Rieu *et al.* [7], who observed regular oscillations revealed as power variations in oceans dominated by swells. Swells, long waves generated by distant storms, have been routinely monitored by side-looking SAR systems, specifically designed for imaging applications. Motivated by this discovery, the primary objective of this dissertation is to explore the potential of nadir-looking SAR altimeters as imaging systems for oceanographic applications while addressing their inherent limitations, acknowledging that these instruments were not originally intended for imaging purposes.

Building on this objective, the dissertation broadens its scope by evaluating oceanographic products used operationally for wave forecasts and scientifically for climate studies in dynamic marine environments. A key component of this effort involved collecting in situ measurements during the One Ocean Expedition 2023 in the Agulhas Current region, a dynamic environment characterized by intense wave-current interactions. These data, capturing localized environmental features, serve as a unique independent reference for performance assessment of both wave models and satellite observations.

1.2 Literature Review

1.2.1 Satellite Altimetry: The Path Toward Ocean Surface Imaging

Satellite altimetry is a radar remote sensing technique dedicated to provide near-surface wind speed, significant wave height and sea surface height measurements, key parameters for oceanographic studies. Measuring sea surface height is critical for understanding sea-level variability and is recognized as an essential climate variable by international climate monitoring frameworks. The global coverage and continuous data provided by altimetry have made it a vital tool for studying ocean circulation and climate variability.

The fundamental principle of nadir-looking altimeters involves transmitting radar pulses toward Earth and receiving the reflected echoes from the sea surface. These reflected echoes, known as *waveforms*, form the core measurement for signal processing. A typical waveform consists of two main components: the fast-rising *leading edge*, representing mostly nadir returned signals, and the gradually decaying *trailing edge*, representing off-nadir reflections from both sides of the radar footprint [8]. Geophysical parameter estimation relies on analyzing individual waveforms using specialized algorithms called retrackers. Retrackers fall into two main categories: physical retrackers, based on models that simulate the physical interaction between the radar signal and the ocean surface, and empirical retrackers, which estimate parameters using geometric properties of the waveform without explicit reliance on physical models [9, 10, 11, 12]. In both cases, the

retracking algorithms primarily exploit the leading edge of the radar return, corresponding to signals reflected directly from the sea surface in the nadir direction. Conversely, the trailing edge, which contains off-nadir reflections, is typically less informative for retrieving geophysical parameters.

Satellite altimetry has undergone significant technological advancements since its inception. Early Low Resolution Model (LRM) altimeters offered along-track resolutions of approximately 7 km, restricting their ability to detect fine-scale oceanic features. A major milestone was achieved in 2010 with the launch of the first Delay/Doppler altimeter, also known as SAR altimeter, aboard CryoSat-2 [3]. This innovation enhanced the along-track resolution to 300 meters, enabling the acquisition of finer-scale measurements. It proved particularly beneficial for providing more accurate measurements in coastal and inland waters, where conventional LRM altimeters often underperform due to land-induced signal contamination within the radar footprint [13, 5].

While SAR altimetry's increased spatial resolution greatly improved data quality in coastal and inland regions, it also introduced new challenges when applied to the open ocean, particularly in the presence of swells. Swells are long-crested waves generated by distant storms, with wavelengths exceeding 150 meters. Moreau *et al.* [14] first reported that the approximately 300-meter width of Doppler strips in SAR altimetry often lead to only partial capture of swells. This, in turn, results in distortions and multiple peaks across the waveform. They further demonstrated that this distortion is further influenced by the relative propagation angle due to the asymmetry of the SAR-altimetry footprint. Additionally, their simulations revealed that ocean retracking algorithms, which assume Gaussian statistics for sea surface elevations within the SAR altimetry footprint, fail to produce accurate results under swell-dominated conditions, leading to significant errors in estimating wave heights. Building on these findings, Reale *et al.* [15] conducted further numerical analyses, indicating that when swell wavelengths are comparable to the altimeter's ground resolution, the waveform shape is notably affected by the relative motion between the sea surface and the satellite. Consequently, the accuracy of significant wave height estimates is degraded compared to measurements obtained from conventional LRM altimeters.

The introduction of the fully-focused SAR algorithm in 2017 marked a major advancement in satellite altimetry by achieving along-track resolutions at near-meter scales [4]. This approach involves coherent processing of the entire illumination time of each scatterer on the surface, similar to techniques applied in side-looking SAR imaging systems [16, 17]. This development has enabled, for the first time, precise monitoring of small inland water bodies, including narrow rivers, ditches and small lakes, providing valuable hydrological information [6].

Motivation

Shortly after this development, several studies began examining further the impact of swell interference on Delay/Doppler, also called unfocused, SAR altimetry. Comparative power spectral density analyses between unfocused and fully-focused SAR data demonstrated a clear aliasing of swell-related signals in unfocused SAR due to undersampling, leading to power leakage into lower frequencies [18, 19, 20, 7]. This finding highlighted the potential fully-focused SAR altimetry holds to resolve long ocean waves. Rieu *et al.* [7]

was the first to report regular oscillation patterns in fully-focused SAR data acquired over swell-dominated ocean regions. Interestingly, these oscillations appear as regular power variations in off-nadir signals, i.e., in the trailing edge, resembling similar intensity modulations to those observed in side-looking SAR images. This raises a compelling research question:

Could nadir-looking SAR altimeters be repurposed as imaging systems over ocean surfaces?

The principles of ocean wave imaging from radar sensors have been extensively studied using side-looking SAR systems, such as Sentinel-1, which has been providing valuable oceanographic data for nearly a decade [21]. These systems exploit wave-induced signal patterns, caused by various intensity modulation mechanisms, to map the ocean wave field. Key processes driving these mechanisms include tilt modulation, range bunching, hydrodynamic modulation and velocity bunching [22, 23]. Among these mechanisms, velocity bunching plays a dominant role in determining the radar response in side-looking SAR systems due to its sensitivity to the relative vertical motion of ocean waves and the satellite. As vertically moving scatterers shift within the radar's imaging footprint, they create characteristic modulations that can be analyzed to extract swell properties, including wavelength, direction, and wave height, through spectral analysis [22, 23, 24, 25]. Furthermore, SAR imagers have demonstrated the ability to provide wave orbital velocity statistics through the estimation of the azimuth cutoff wavelength [26]. The azimuth cutoff wavelength serves as a proxy for the shortest detectable waves [27], providing an additional independent metric for evaluating the imaging limitations of SAR systems under varying wind and wave conditions.

Before addressing the central research question of this dissertation, it is important to acknowledge the complexity of utilizing an instrument beyond its originally intended application. In this context, a critical distinction lies in the measurement geometry: side-looking SAR imagers operate at oblique incident angles, generating a fundamentally different backscatter geometry compared to nadir-looking altimeters, which are dominated by specular reflection [28]. This geometric disparity, coupled with distinct instrument design principles, plays a central role in determining how ocean surface features are observed and interpreted. Recognizing both technological advancements and challenges in SAR altimetry, this dissertation primarily investigates its potential to function as an imager for ocean applications, exploring in depth inherent limitations and capabilities.

1.2.2 Challenges in Modeling Waves in Dynamic Marine Environments

Satellite altimetry's role in space oceanography extends beyond the acquisition of the three main geophysical parameters discussed earlier. Altimetry-derived sea surface height, along with gravimetry and in situ data, is used to derive geostrophic currents [29], enabling global ocean current mapping. Ocean currents have a profound influence on wave evolution, as their interaction with incoming waves can cause refraction, altering wave direc-

tion, wavelength and amplitude through processes such as wave steepening and trapping [30]. These phenomena are key drivers of extreme wave events, particularly in regions dominated by strong currents with velocities exceeding 2 m/s, such as the Agulhas Current [31].

Accurate prediction and monitoring of extreme wave events is crucial for oceanographic studies, maritime navigation, safety and operational planning in both offshore and nearshore environments. However, the reliability of wave datasets is often diminished when ocean currents are omitted or inaccurately represented in models. Studies have shown that inaccuracies in the proper modeling of currents can lead to substantial errors in wave height predictions, especially under extreme sea state conditions [32, 33]. These inaccuracies can be enhanced by insufficient spatial and temporal resolution of available products, limiting their ability to capture the rapid variability of ocean currents and, consequently, their impact on wave evolution. This highlights the ongoing need to improve wave models through advanced data assimilation techniques and robust validation against in situ measurements.

In situ data collection campaigns play a crucial role in addressing these challenges by providing accurate measurements of the wave field. These campaigns range from short-term deployments, aimed often at satellite calibration and model validation, to long-term observations that support climate studies, offshore engineering and coastal management. However, regardless of their duration, in situ campaigns are constrained by limited spatial coverage due to the significant operational and maintenance costs involved. In particular, deploying and maintaining buoys or sensors in remote or deep-sea locations is both expensive and complex, requiring specialized vessels, energy supplies and skilled personnel.

Motivation

During this Ph.D. project, in situ wave measurements were collected in the Agulhas Current region as part of the One Ocean Expedition. The Agulhas Current is one of the most dynamic western boundary currents in the world, flowing in the Indian Ocean along the southeastern coast of Africa. The wave and current environment in this region is highly energetic and presents unique challenges due to its extreme variability and strong interactions between waves, currents and winds [34, 35]. At its southern boundary, the current undergoes retroflection, turning back into the Indian Ocean, shedding large eddies that propagate into the South Atlantic. This process, coupled with frequent intense storms driven by the westerly storm tracks of the Southern Ocean, creates an environment of rapid changes in wave and current strength, direction and eddy activity [36]. It becomes clear that such dynamic conditions make wave model predictions particularly challenging. Leveraging the collected in situ data, this dissertation further conducts a comprehensive evaluation of wave and ocean current data quality derived from both numerical models, reanalysis products and satellite observations.

1

1.3 Thesis Objectives

This PhD dissertation presents the first systematic study of the imaging capabilities of SAR altimeters for ocean applications, introducing a novel approach to deriving wave properties that were previously unattainable using existing signal processing techniques. Considering that these instruments are not originally designed for imaging application, inherent limitations are investigated in detail. The scope of this dissertation broadens to assess the performance of satellite altimetry products and wave models, with a particular focus on dynamic ocean environments where waves interact with strong ocean currents, shedding light on uncertainties in operational products. To address these scientific topics, three key research objectives are defined as follows:

Exploring off-nadir signal modulations in fully-focused SAR altimetry for swell retrieval.

Fully-focused SAR altimetry has demonstrated unprecedented along-track resolutions at meter scales, emerging as a promising tool for advancing ocean and inland-water applications from space. The first spectral analysis of off-nadir fully-focused SAR altimetry data over oceans is presented, focusing on backscatter modulations induced by swells. Building on technological and scientific advancements from side-looking SAR imagers, a method is developed to compute SAR altimetry intensity modulation spectra, enabling the extraction of swell properties such as wavelength and direction. The method's reliability is assessed through comparisons between Cryosat-2 intensity modulation spectra with buoy-derived swell wave spectra under varying wave and wind conditions. To aid in interpreting the results, numerical simulations are built, describing the dominant modulation mechanisms driving wave imaging and providing deeper insight into the underlying processes and differences compared to side-looking SAR imagers. Finally, potential improvements in swell retrieval enabled by the enhanced ground resolution of Sentinel-6A's full-beam footprint are discussed.

Investigating the wave imaging limitations and sea-state characterization in fully-focused SAR altimetry using azimuth cutoff analysis.

Emphasis is then given in understanding and defining the wave imaging limitations of SAR altimeters. To achieve this, the azimuth cutoff wavelength is estimated as an independent parameter from off-nadir fully-focused SAR signals. This parameter represents the shortest waves that can be detected by a SAR system under various wind and wave conditions. Its estimation is achieved using the radar signal's along-track autocorrelation function, applying two distinct methods developed in the spatial and wavenumber domains. The limitations of both methods, including the effects of relative wave propagation angle, extreme sea states and the presence of swells, are thoroughly examined. Additionally, the azimuth cutoff wavelength is utilized to extract valuable sea-state information through the characterization of wave orbital velocity statistics. The analysis is conducted using Sentinel-6A data from a full 10-day repeat cycle, aiming to assess the global applicability of these methods by comparing the results with model-derived parameters.

Assessing the reliability of wave and ocean current products from models and remote sensing observations in current-dominated oceanic environments.

Given the critical importance of accurate wave data in both forecasting systems and climate studies, wave height estimates are assessed, with a particular focus on regions dominated by ocean currents. Using as reference drifter measurements collected in the dynamic oceanic environment of the Agulhas Current, the impact of wave-current interactions on wave parameters is examined by comparing models including and excluding ocean current forcing. The analysis further investigates the compatibility of different remote sensing sensors in capturing swells within such a complex oceanic environment. In particular, swell observations from operational satellite products, including Sentinel-1 and CFOSAT, are compared for the first time with the SAR altimetry-derived swell product developed during this PhD project. All three satellite-derived swell products are then validated against in situ measurements.

1

1.4 Outline of the Thesis

The dissertation is organized into five chapters, beginning with the introduction (Chapter 1), followed by three peer-reviewed journal publications (see List of publications) that cover the aforementioned objectives (Chapters 2-4) and concluding with a chapter presenting the main findings and recommendations (Chapter 5). In more details:

- **Chapter 2** introduces the first spectral analysis of off-nadir fully-focused SAR altimetry data aimed at computing intensity modulation spectra for characterizing swell waves. This work includes a detailed description of the developed method, its implementation and application to CryoSat-2 data as well as comparisons with ground-truth swell measurements. Then, simulations developed to mimic off-nadir SAR responses are presented with the goal to understand the underlying dominant modulation mechanisms. The material covered in this chapter is primarily based on the following publication:

  Altiparmaki, O., Kleinherenbrink, M., Naeije, M., Slobbe, C. and Visser, P. (2022). SAR altimetry data as a new source for swell monitoring. Geophysical Research Letters, 49, e2021GL096224, doi:10.1029/2021GL096224

  Chapter 2.4.2 presents an additional analysis conducted after the publication, focusing on the implementation of the swell retrieval method on Sentinel-6 data. The objective is to explore the potential benefits of the satellite's full beam-limited footprint, a portion of which is truncated onboard.

- **Chapter 3** addresses limitations of the swell application from SAR altimeters, particularly with regard to resolution loss. The extent of this loss primarily depends on sea-state conditions, making it a valuable metric for deriving wave orbital velocity statistics. The study introduces two distinct approaches for estimating the azimuth cutoff wavelength and the variance of wave orbital velocities. Both methods are applied globally on Sentinel-6A data to assess their applicability, strengths and limitations under various sea-state conditions and measurement geometries by comparing the results with model-derived parameters. This chapter is fully covered by the following publication:

  Altiparmaki, O., Amraoui, S., Kleinherenbrink, M., Moreau, T., Maraldi, C., Visser, P.N.A.M. and Naeije, M. Introducing the Azimuth Cutoff as an Independent Measure for Characterizing Sea-State Dynamics in SAR Altimetry. Remote Sens. 2024, 16, 1292, doi:10.3390/rs16-071292

- **Chapter 4** focuses on the third research objective. Wave and ocean surface current datasets obtained from drifter measurements in the Agulhas Current region serve as a reference for a quantitative evaluation of model and satellite-derived operational products. Surface current velocities from the Mercator model and the altimetry-derived Globcurrent product are first validated against drifter data to assess the quality of current forcings used in wave modeling. Subsequently, the accuracy of wave height and Stokes drift parameters from wave models and reanalysis products, either excluding or

including the aforementioned ocean current products, is examined. The content of this chapter is primarily based on the following publication:

Altiparmaki, O., Breivik, Ø., Aouf, L., Bohlinger, P., Johannessen, J. A., Collard, F., et al. (2024). Influence of ocean currents on wave modeling and satellite observations: Insights from the one ocean expedition. Journal of Geophysical Research: Oceans, 129, e2024JC021581, doi:10.1029/2024JC021581

Chapter 4.5.2 presents an additional analysis conducted after the publication, focusing on the cross-comparison of satellite-derived swell-induced modulation spectra from various sensors, including SAR imagers, SAR altimeters and wave spectrometers. The objective is to evaluate their performance against in situ measurements and investigate their compatibility for future synergistic use.

- **Chapter 5** summarizes the main conclusions of this PhD dissertation and provides recommendations for future research.

2

SAR Altimetry Data as a New Source for Swell Monitoring

This study shows the first spectral analysis of fully-focused Synthetic Aperture Radar (FF-SAR) altimetry data with the objective of studying backscatter modulations caused by swell. Swell waves distort the backscatter in altimetry radargrams by means of velocity and range bunching. These swell signatures are visible in the tail of the waveform. By locally normalizing the backscatter and projecting the waveforms on an along-/cross-track grid, satellite altimetry can be exploited to retrieve swell information. The analysis of FFSAR spectra is supported by swell spectra derived from both buoys of the National Oceanic and Atmospheric Administration network and the European Centre for Medium-range Weather Forecasts Reanalysis v5 product. Using cases with varying wave characteristics, we discuss Cryosat-2 and Sentinel-6A altimetry-derived modulation spectra and relate them to what is known from side-looking SAR imaging systems. Besides having a vast amount of additional data for swell-wave analysis, altimeter data can also help us to better understand the side-looking SAR spectra.

2.1 Introduction

Satellite radar altimetry data have been used for more than thirty years to derive sea surface height, significant wave height and wind speed. In conventional low-resolution mode altimetry, the presence of swell has never been considered, because it was an inseparable part of the estimated significant wave height. The advent of delay/Doppler, or unfocused Synthetic Aperture Radar (SAR), altimetry [3] with the CryoSat-2 mission in 2010 improved the along-track resolution from 7 km to about 300 m, and with dedicated fully-focused SAR (FFSAR) processing [4] theoretically up to about 0.5 m. Although the presence of swell is known to deteriorate the accuracy of geophysical parameters derived from delay/Doppler data [37, 38, 39, 40, 41, 14], no attempt has been made to derive swell parameters from these data. Here, we present the first spectral analysis of FFSAR data and discuss how FFSAR spectra can be used to infer swell-wave spectra.

Moreau *et al.* [14] concluded that the degradation of the quality of the altimetry-derived geophysical parameters appears due to the narrow sampling window in the satellite along-track direction that can no longer fully capture long waves in the instrument ground cells, but only a portion of them. This, in turn, results in distorted waveform shapes which vary depending on the captured portion. According to Reale *et al.* [15] this distortion appears to worsen when the ocean wavelengths are of the same order as the delay/Doppler altimeter along-track resolution, which typically occurs if swell systems are present. Recently, Rieu *et al.* [7] showed that in delay/Doppler altimetry data of a higher burst repetition frequency, oscillations are observed on the waveform's trailing edge in locations where swells occur. This, in combination with the fact that swell related SAR signal has been shown to be aliased into other frequencies [18, 19, 20], imply that the high-rate sampling of FFSAR data may be suitable for detecting swell-related information and, therefore, for explaining such distortions in the radar backscatter signal.

Since the seventies the SAR and Real Aperture Radar (RAR) imaging mechanisms have been investigated in detail as they have been useful tools for monitoring ocean surface waves [42, 43, 44, 45]. The main RAR modulations that are responsible for the imaging of ocean waves are the tilt modulation, which is related to local changes to the incident angle by slopes of long waves, range bunching, which is the variation of surface area captured in resolution cells as a consequence of the same slopes, and hydrodynamic modulation, which is triggered by the interaction between short (wind) and long (swell) waves [22]. The SAR processing introduces one more mechanism, called velocity bunching [22], that seems to dominate in most cases [24]. The velocity bunching is the clustering of the signal due to the vertical motion of the waves. In more detail, the phase-history difference of echoes between nearby along-track points is approximately linear. The motion of a scatterer in the range direction, which corresponds to vertical motion for an altimeter, can replicate this linear behavior causing the projection of the scatterer to be misplaced in the along-track direction. As scatterers ahead and behind the crest of a wave move up and down, respectively, they are both shifted in a SAR image in opposite directions. Depending on the direction of the wave with respect to the radar motion, scatterers are clustered either around the crest or the trough. With a spectral model, containing both RAR and the shift due to velocity bunching, a SAR intensity spectrum can be inverted to obtain part of

the wave spectrum [23]. The inversion is limited to long waves as the effective resolution of SAR observations over ocean is far less than the theoretical limit [46, 25], with typical values of 100 m. In contrast to side-looking SAR systems, altimeters are nadir-looking radars. This difference has an impact on the backscatter mechanisms which prevail [28] and also geometrically changes the RAR response. The so-called Bragg, or resonant, scattering dominates for a side-looking system at moderate sea states, while the specular scattering for a nadir-looking system.

This chapter demonstrates the potential of SAR altimetry data to infer swell-wave spectra. We introduce a methodology to process altimetry data to estimate a FFSAR spectrum, which is suitable for an inversion in a comparable way as for side-looking SAR data. Moreover, this study gives a detailed description on the modulation process, shows how this differs from a side-looking system and discusses the adaptions required for a nadir-looking system. Lastly, buoy data are used to support the analysis.

2.2 Data and Methods

This section is divided into two parts. The first part introduces the processing steps to obtain a FFSAR spectrum. The second part shortly discusses the buoy data.

2.2.1 SAR Altimetry Data Processing

A flowchart of the main processing steps is given at the top of Figure 2.1, while an example accompanies it to better understand the behavior of the backscatter altimetry signal. The latter concerns data from a descending orbit of CryoSat-2 over the Channel Islands of California on January 2, 2020. The presence of swell waves, with a period of 20 seconds and direction 281 degrees with respect to North, is confirmed by a nearby buoy of the National Oceanographic and Atmospheric Administration-National Data Buoy Center (NOAA-NDBC) network (`https://www.ndbc.noaa.gov/`). The FFSAR L1b multilooked waveforms used in this study were obtained from the ESA Grid Processing-on-Demand (GPOD) FFSAR service. This service is based on the Omega-Kappa SAR focusing algorithm described in Guccione *et al.* [47]. For the demonstration, we use radargrams of 500 waveforms of 200 Hz multilook posting rate, which corresponds to an along-track sampling of about 34 m, with a total sample length of about 17 km. Note, that if single-look waveforms are available, we may opt a weighted multilooking, because it acts as a filter and this, in turn, may have an impact on the FFSAR spectra. The first panel, *i.e.,* Figure 2.1a, depicts a radargram. A closer look at the tail of it reveals undulations that are caused by swells.

For an accurate application of the method, the waveforms in the radargram should be aligned. A change of the leading edge of one bin leads to a misprojection of tens of meters across track. Small variations of the leading edge location can be dealt with in the ground-projection step, but larger variations can lead to normalization problems. A suitable realignment strategy is a two-step process: i) the waveforms are averaged over a distance larger than the along-track-projected swell wavelength and retracked, and ii)

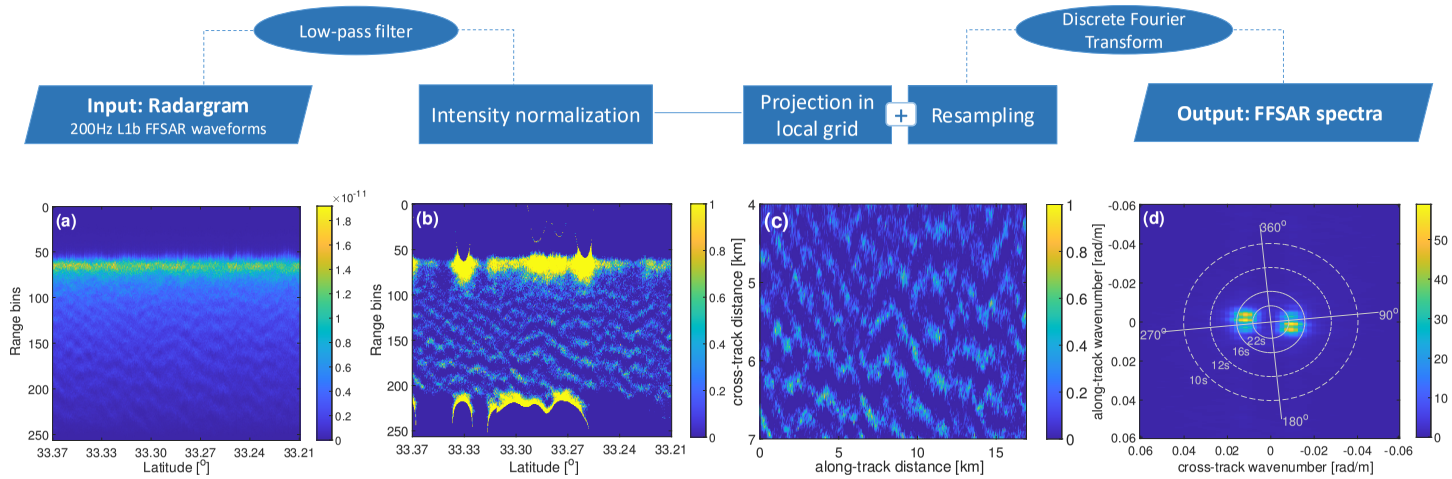

Figure 2.1: *(a)* Radargram: CryoSat-2 FFSAR waveforms of 200 Hz multilook posting rate as a function of latitude. The color gradation represents the echo power variations (Watt). *(b)* The normalized radargram and *(c)* the projected/resampled radargram. *(d)* FFSAR spectra. A flowchart of the processing steps is given at the top.

consecutively a phasor is applied to the complex values in FFSAR processing after the range-residual-phase correction to realign the retracked bin to a pre-defined reference. As for the cases considered in this study the waveforms are aligned to less than a bin and no wave-spectrum inversion is performed, realignment is not applied.

The first step is the normalization of the radargram intensity (Figure 2.1b). This is required to compute the normalized FFSAR spectrum at a later stage so that it can be used in a wave spectrum retrieval algorithm comparable to the one used for side-looking SAR systems, such as Sentinel-1. In the case of Sentinel-1, the intensity of a scene of 20 km × 20 km (wave mode) is normalized by first subtracting the mean intensity and then a division by the mean intensity. However, due to the drop of the power in the trailing edge of the SAR waveforms, such a normalization is not suitable. We overcome this by first computing the expected intensity $\hat{I}$ for each bin in the radargram. The expected intensity is used to compute the normalized intensity I_N, i.e.,

$$I_N = \frac{I - \hat{I}}{\hat{I}} \tag{2.1}$$

where I indicates the radargram intensity. Note that, I should resemble the scaling of a SAR image. The expected intensity $\hat{I}$ is computed from the data by first applying a Gaussian filter in along-track direction with a width (defined as two times the standard deviation) of 25 waveforms. This corresponds to about 850 m along track. The filter length is cut at 51 waveforms (a sensitivity analysis is done in supporting material). Then we fit a polynomial of degree 4 to the tail of each waveform. The tail includes all bins between 4 km and 7 km across track. Finally, $\hat{I}$ is obtained by evaluating the polynomial at the waveform bins, and subsequently used to compute I_N.

In the second step, the normalized waveforms are projected on the ground. The distance between the cross-track points is determined as

$$l_{\text{cross}} = \sqrt{(h + (n - n_{\text{ref}})dR)^2 - h^2} \tag{2.2}$$

where l_{cross} indicates the horizontal distance between the range bins projected on the ground, dR is the range sampling interval of 0.234 m, n is the range bin, n_{ref} the leading edge reference bin and h is the mean satellite altitude for the area of interest. In along-track direction, the distance between successive points is determined by the along-track sampling. To relate each range bin to a unique cross-track location the radargram is projected as if all backscatter is received from the right side. Consequently, the projected normalized radargram contains a correctly projected backscatter signal of the right side and a left-right flipped backscatter signal from the left side. Backscatter distortions, caused by a monochromatic swell wave, are therefore expected to exhibit a crossing pattern.

In the last step, we compute the FFSAR spectrum as the square of the Discrete Fourier Transform (DFT) amplitude [48]. Prior to the DFT operation, the projected data are interpolated to an equidistant grid with a resolution of 10 m. Note that the DFT is only applied to the trailing edge (corresponding to 4-7 km across track) of the waveforms (Figure 2.1c). To suppress the speckle noise in the FFSAR spectra, a Gaussian filter with a width of 4 pixels (two standard deviations) is applied to it. The resulting spectrum for the example track is given in Figure 2.1d. Although the common way to suppress noise is to use cross-spectra

computed by subswath processing [49], this is currently not feasible with the GPOD FFSAR processor.

We have to note that with the transmission of pulses by CryoSat-2 and Sentinel-3A/B, spatial aliases, caused by the closed-burst sampling, appear at approximately 90 meter along track [4]. The spectral response under swell conditions is normally more than one order larger than the spectral response of the ghosts. In case of low sea states, the spectral response of the ghosts cannot be ignored and should be appropriately handled.

2.2.2 Buoy Data

Buoy data from the NOAA-NDBC network are used to verify and discuss the FFSAR spectra. From these publicly available data we collected the swell-wave spectra along with the peak period (i.e., the period with the maximum wave energy) and the direction from which the waves with the corresponding peak period are coming. The data have an accuracy of ± 1 second and $\pm 10^{\circ}$, for the peak period and direction, respectively.

We demonstrate the method for an area in the Northeast Pacific Ocean. This area is chosen because there is often swell present and a buoy is located in offshore waters to limit the effects of coastlines and bathymetry (depth ranges from 100 m to 1100 m). In this area CryoSat-2 operates in SAR mode. CryoSat-2 data were considered within a radius of 50 km from the buoy. Four cases, identified as having swell systems are discussed here. The upper panel of Figure 2.3 illustrates a map with four CryoSat-2 tracks, two descending and two ascending, as well as the buoy location. To limit effects of spatial and temporal variations between the buoy and FFSAR spectra, the time needed for the swell system to cross both measurement locations should be taken into account. This time offset, Δt, was calculated as

$$\Delta t = \frac{\Delta x}{c_g} \cos(\phi_w - \phi_m) \tag{2.3}$$

where Δx indicates the distance calculated from the middle point of each overpass to the buoy, c_g is the group velocity calculated using linear wave propagation theory and considering intermediate conditions, ϕ_w is the wave direction with respect to the North, and ϕ_m the relative direction of the satellite track and the buoy with respect to the North. Then, based on the relative position of the satellite and the buoy with respect to the wave direction, *i.e.*, whether the waves cross first the satellite observation location or the buoy, the time offset was accordingly added or subtracted from the acquisition time of the satellite data in order to select the buoy epoch.

2.3 Hasselmann's SAR spectrum

To support the interpretation of the obtained FFSAR spectra, we introduce the analytical model relating the SAR spectrum to a wave spectrum presented by Hasselmann and

Hasselmann [23]

$$P(k_x, k_y) = \int\int G(x, y, k_x, k_y) e^{-i(k_x x + k_y y)} dx dy \tag{2.4}$$

which is a function of the cross-track wave number k_x and the along-track wave number k_y. This spectral mapping depends on the characteristic function [50]

$$G(x, y, k_x, k_y) = e^{k_y^2(\rho_{yy}(x,y) - \rho_{yy}(0,0))}(1 + \rho_{II}(x, y) + H) \tag{2.5}$$

with ρ_{yy} being the correlation of azimuthal shifts as a function of wave spectrum S, and ρ_{II} the correlation function of linear RAR modulations containing range bunching, tilt and hydrodynamic modulation also as a function of wave spectrum S. Higher-order terms, H, are ignored as it simplifies the equation, and as their contribution is an order smaller than ρ_{II} [51, 49]. The spectral transform and its correlations are further elaborated in Krogstad *et al.* [51], Engen and Johnsen [49], Hasselmann *et al.* [52], Schulz-Stellenfleth and Lehner [53], and others. Note that, as the characteristics function depends on wavenumbers k_x and k_y, the integral Eq. 2.4 is not a Fourier Transform. In fact, the integral should be evaluated for each wavenumber separately. In this study, this simple form of the equation [54] is dissected into separate terms to support the interpretation of FFSAR spectra.

2.3.1 SAR Modulation

First, the $e^{-k_y^2(\rho_{yy}(0,0))}$ term (referred to as 'term A') can be taken out of the integral. The term $\rho_{yy}(0,0)$ represents a scaled velocity variance [53, 26]. At higher sea states, the velocity variance increases. Term A causes a decrease of SAR spectral power with increasing k_y, which represents the reduction of along-track resolution as a consequence of random linear motions of scatterers. Further resolution loss can occur due to higher-order motions of scatterers, which decrease the decorrelation time [26, 46].

Second, the term $e^{k_y^2 \rho_{yy}}$ (referred to as 'term B') represents, together with the first term, the velocity bunching. The second term, which is non-linear, increases with an increasing angle of wave propagation (here the angle is defined with respect to the cross-track direction). Under some circumstances, e.g. weak wind and strong swell, secondary responses appear in the SAR spectrum [53]. The exponential term becomes equal to 1 in case $k_y = 0$, which implies that velocity bunching does not occur with waves travelling in the cross-track direction.

2.3.2 RAR Modulation

The last term, ρ_{II}, (referred to as 'term C') represents the first-order RAR response and can be considered as the response of the ocean surface if it was not moving during the time of overpass. It is affected by range bunching, tilt, and hydrodynamic modulations [22, 25, 55]. It is different for side-looking and nadir-looking systems as described in the introduction. In contrast to the velocity bunching, RAR modulation also occurs with cross-track travelling waves [56]. The discussion on the RAR modulation is supported by simulation results, provided in supporting material.

In Figure 2.2 a geometric representation of a cross-track propagating swell wave is shown. Hydrodynamic interaction of long waves with shorter ones causes an increase of roughness just after the crest, which reduces the specular reflection. The maximum specular reflection caused by hydrodynamic interaction is therefore expected just behind the trough. Tilt causes an increase of returned power where incident signal is close to normal to the surface, which is also close to the point where range bunching is maximal as at that point the largest surface area is captured between two range isolines. Tilt and range bunching are maximal on the slope facing the satellite. For small significant wave heights there is one maximum near the slope maximum (see supporting material, Figures S3.2A/S3.2B), but if the wave slopes are larger than the incident angle, two maxima appear that move towards the crest and the trough (see supporting material, Figures S3.3A/S3.3B). On one side of the satellite, the range bunching and tilt occur on same slope as hydrodynamic modulation, but on the other side not (Figure 2.2b).

For a near-nadir looking radar system the hydrodynamic modulation is considered small compared to range bunching and tilt [57] and is therefore not considered. For swell waves considered in this study, tilt modulation is much smaller than range bunching (see supporting material) and will therefore also be ignored in the further analysis. Note that the range bunching is very non-linear as the slopes of the swell waves are typically larger than the incident angle. Even for a monochromatic wave the spectral response will be smeared as we might have two maxima on one satellite-facing slope of the wave with a distance between them that depends on wavelength, amplitude, and direction (see supporting material, Figures S3.2A-S3.3B). When waves propagate in the along-track direction the range bunching is nearly zero. A small signal, though, remains as crests and troughs are captured in different range bins, which have a different projected cross-track resolution. This complexity is further enhanced by overlay (Figure 2.2a), which makes it difficult to derive a closed-form expression for the spectral response of range bunching. At slopes smaller than the incident angle, the range bunching might be approximated by the equations used for the Chines-French Oceanography Satellite (CFOSAT) [57, 58].

Due to radial velocities the RAR modulated signal are also moved in the along-track direction and get bunched (Figure 2.2b). If only range bunching and velocity bunching are considered and the waves are symmetric with respect to the crest, the expected modulation is out-of-phase left and right of the track whereas the expected spectral power is the same. However, it is a statistical process, which causes a deviation from the expected value (see supporting material, Figures S3.4A/S3.4B and S3.7A/S3.7B) and a difference between the spectral amplitudes left and right. Simulations indicate that velocity bunching and range bunching have the same order of magnitude, with range bunching often dominating (see supporting material S3.5A-S3.6B and S3.8A-S3.9B). However, this ratio depends on the significant wave height, wave direction and wavelength.

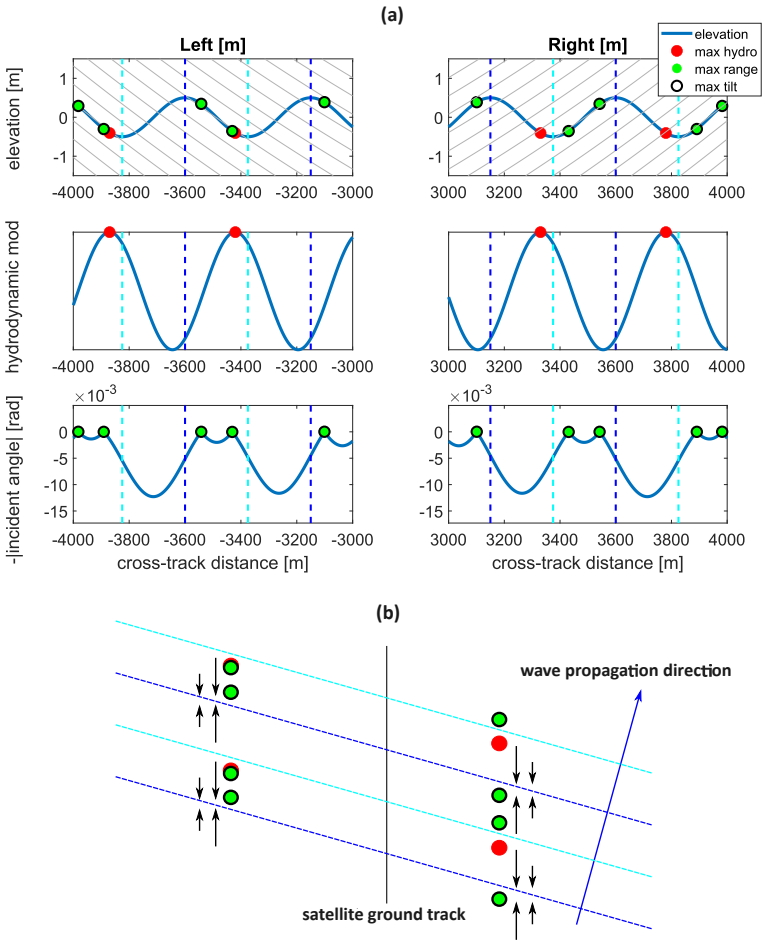

Figure 2.2: *(a)* Geometric representation of the RAR imaging modulations in nadir-looking systems as a function of the altimeter cross-track footprint from ± 3000 to ± 4000 m for a 450 m swell wave system: the light and dark blue dashed lines represent the troughs and crests, respectively, while the light gray lines indicate the range isolines. The maxima of the hydrodynamic modulation, which result from reduced roughness near the troughs, are indicated with red dots. The middle panels show the approximate sinusoidal behavior of the hydrodynamic modulation. The bottom panels show that the maxima of the range bunching (green dots) and tilt modulation (black-outlined circles) coincide with minimum local incident angle. Range bunching is maximal where the surface is aligned with the range isolines. *(b)* Top view of the corresponding RAR and SAR modulations. The SAR modulation, *i.e*, velocity bunching, is maximal either near troughs or crests. The change of focal location due to surface motion is indicated with the black arrows. Therefore for this specific case, the velocity bunching is maximal near the crests.

2.4 Results and Discussion

2.4.1 Cryosat-2

The panels of the second row in Figure 2.3 show the projected radargrams used for the computation of the FFSAR spectra, which are presented in the panels of the third row. Note that the axes of the latter have been reversed to easily compare the FFSAR spectra with the swell-wave spectra given in the bottom panel. Four peaks are observed, one per quadrant. This differs from a SAR spectrum computed by a side-looking SAR system, where only a signal of (k_x, k_y) is mirrored at $(-k_x, -k_y)$. The ambiguity of 180 degrees in a side-looking system is normally accounted for by using the imaginary part of a cross spectrum [49], which can also be done by subswath processing of altimetry data. In FFSAR spectra two additional peaks, albeit with less power, are present in quadrants that do not exhibit substantial wave energy. As the altimeter observes both sides of the ground track at the same time, the expected value will get approximately mirrored around the ky-axis if velocity bunching and range bunching are dominant. In that case, the (double-sided) FFSAR spectrum, $P_{2s}(k_x, k_y)$, is approximated as

$$\begin{aligned} P_{2s}(k_x, k_y) &= \gamma P_r(k_x, k_y) + (1-\gamma) P_l(-k_x, k_y) \\ P_{2s}(k_x, k_y) &\approx 0.5(P(k_x, k_y) + P(-k_x, k_y)) \end{aligned} \tag{2.6}$$

where P_l and P_r the approximated spectra from the left- and right-hand sides of the ground track, and $P(k_x, k_y)$ as in Eq. 2.4. γ is a weighting factor close to 0.5 depending on platform roll, the antenna pattern, but can be also influenced by cross-track waves and the skewness in slope probability distribution function [59].

In three of the four shown cases the signals in two quadrants are substantially weaker than expected. This can partly be explained by a statistical deviation from the expected value (see differences between the left- and right-side spectra in supporting material, Figures S3.7A/S3.7B). There are also other possible deterministic causes for the discrepancy. First, there might be geophysical effects, such as the interaction of waves with currents and bathymetry that cause a cross-track difference in the backscatter modulation between both sides of the track. Second, there are instrumental effects such as the roll of the satellite that cause the gain to vary between both sides of the satellite, which is indicated with the term γ in Eq. 2.6. However, from the four cases shown here and in supporting material S2 (accessible through the digital version of the publication), it appears that the return power in the quadrants the waves are actually moving is higher than in the other two quadrants.

The latter indicates an asymmetric upwave-downwave response. The model for velocity bunching and range bunching alone (see supporting material) is not able to reproduce a deterministic asymmetric response. Therefore either the wave properties are not symmetric and/or mirrored around the crest (i.e., slope and radial velocity) or a substantial hydrodynamic modulation would be required. At the moment of writing this asymmetry is not fully understood. Note that, Li *et al.* [57] also described an up-to-down wave asymmetry in the fluctuation spectrum computed from CFOSAT data with a larger spectral response in the upwave direction.

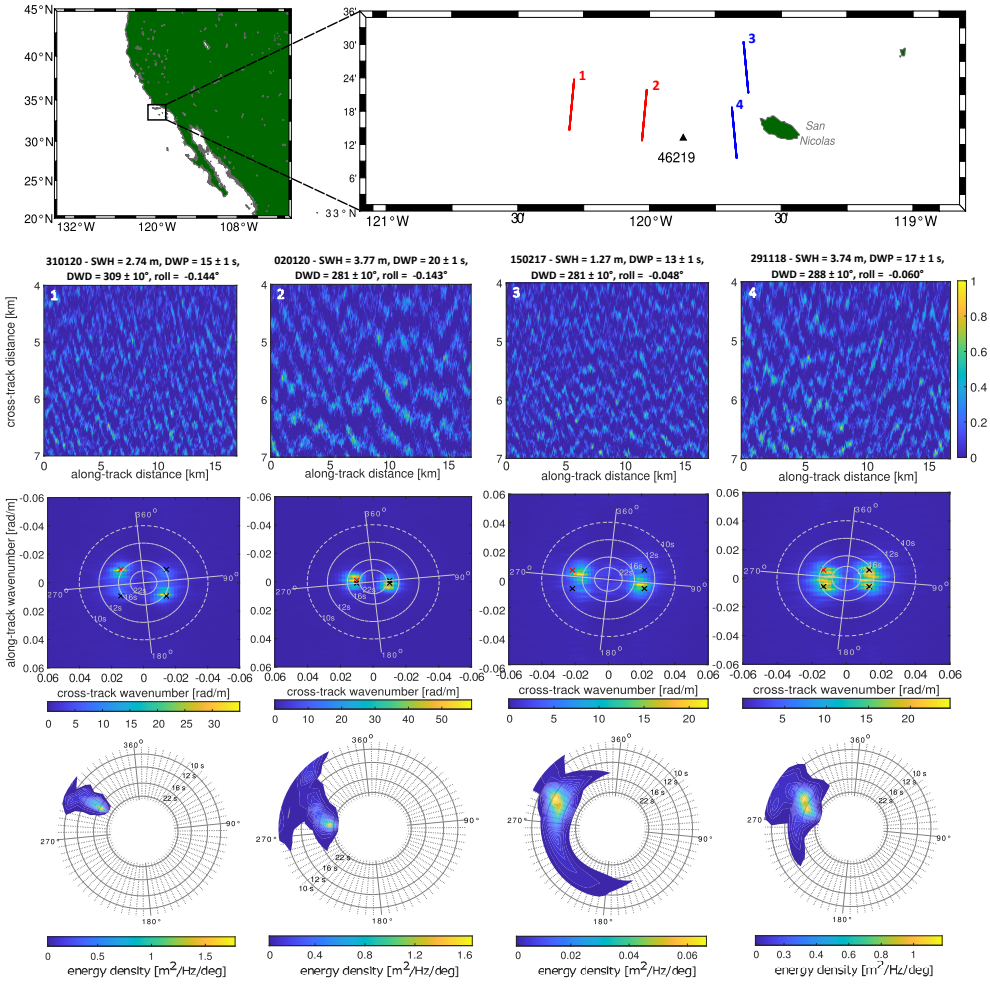

Figure 2.3: A map of the study area is given on the top. The red and blue lines represent the descending and ascending CryoSat-2 tracks, respectively, while the black triangle indicates the buoy with World Meteorological Organization number: 46219). Below, each column of panels show the projected waveform-tail radargrams, the corresponding FF-SAR spectra and the swell-wave spectra obtained from the buoy for two descending (*cases 1 and 2*) and two ascending (*cases 3 and 4*) overpasses. The red crosses, plotted on top of the FFSAR spectra, represent the wavenumber vector with the maximum wave energy based on the buoy measurements. The acquisition date along with the *in situ* observations (SWH = significant wave height, DWP = dominant wave period, DWD = dominant wave direction) and the mean roll angle of the satellite are given at the top. The SWH is calculated as the average of the highest one-third of all of the wave heights.

By comparing the FFSAR spectra with the buoy-derived swell-wave spectra it is observed that the maximum energy closely coincide for all four cases, but the wavenumber difference between ocean-wave spectra and SAR spectra peaks is generally non-zero. Discrepancies can occur due to the non-linear nature of the SAR and RAR responses. A reduction of signal might occur in the cross-track direction, as velocity bunching (term B) goes to zero and the spectral response caused by range bunching (term C) is typically a bit smaller in the cross-track direction as the response smears over more wavenumbers (see supporting material). An approach of the cut-off wavelength (related to term A) in the azimuth direction, decreases the response at increasing k_y. Waves with a relatively high along-track wavenumber will therefore be dampened. The (along-track) resolution depends on the sea state, or more precisely the velocity variance (term A) of the ocean (see section about the SAR spectrum), but also on the coherence time of scatterers [42, 44, 60]. The typical coherence time of a C-band SAR imaging system (e.g., Sentinel-1, Envisat and others) in open water is 50 ms [61]. At 50 ms the velocity variance is the dominant driver for resolution loss. The coherence time for a Ku-band altimeter, with its shorter wavelength, is smaller and therefore the resolution loss is likely more severe. Lastly, small differences between the location of peak energy in the buoy-derived swell-wave and FFSAR spectra may occur because of the non-linear responses of SAR, which are captured by higher order terms in the G-function (Eq. 2.5) for which RAR and SAR are not independent.

2.4.2 Sentinel-6A: RMC versus RAW

Sentinel-6A, launched in 2020, is equipped with the Poseidon-4, a Ku-band nadir-looking SAR altimeter. To ensure continuous ocean observations while minimizing data volume, the satellite employs an onboard Range Migration Correction (RMC) algorithm. This algorithm reduces the data rate by truncating portions of each waveform, effectively halving the transmitted data volume [62]. Figure 2.4 illustrates a FFSAR radargram where the acquisition mode transitions from RMC (truncated operational product) to RAW (full beam-limited footprint prior to truncation) over a calibration zone near the Channel Islands of California. While the loss of the permanently truncated signal does not impact the quality of the retrieved geophysical parameters (sea surface height, significant wave height, wind speed), it is expected to affect swell retrieval, as long waves are more prominently featured in the extended RAW window (see Figure 2.4).

To assess the signal loss impact on swell retrieval, we analyzed cases where both RMC and RAW data are available over the same region during the commissioning phase around the Hawaiian islands, covering repeat cycles 15–17. The RAW and RMC FFSAR L1b data were obtained through the EarthConsole platform with support from the ESA Network of Resources Initiative. Figures 2.5 and 2.6 present two cases: swells with a 15.5 second peak wave period propagating along the track (Figures 2.5) and swells with a 12.4 second peak wave period propagating across the track (Figures 2.6), as derived from data provided by the European Centre for Medium-Range Weather Forecasts Reanalysis v5 (ERA5) [63]. The waveform-tail radargram for RMC spans a cross-track range of 4–7 km, while for RAW it extends from 7–12 km, both measured relative to the retracked range bin at the

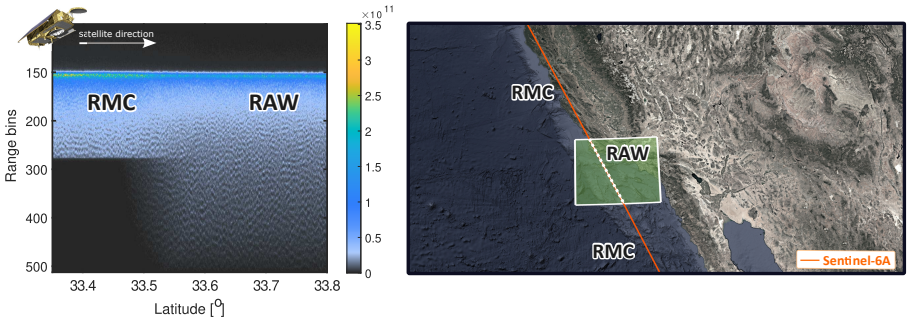

Figure 2.4: Example of a Sentinel-6A FFSAR radargram representing multilooked waveforms with an along-track resolution of approximately 30 m (*left*). The data were acquired over a RAW-to-RMC transition zone around the Channel Islands, California (*right*).

leading edge. With incident angles ranging approximately from 0 to 0.7 degrees across the full waveform, the cross-track ground resolution improves with increasing distance from nadir, as the range isolines become more closely spaced at the edges of the footprint. The RAW waveform-tail radargrams demonstrate this enhanced ground resolution, where wave-like patterns appear more defined and consistent compared to those in the RMC radargrams.

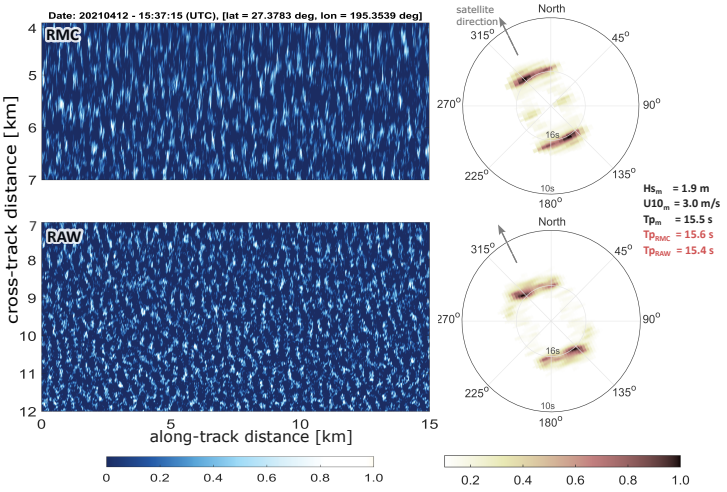

Figure 2.5: Swells in *along-track*: projected waveform-tail radargrams for RMC (*top*) and RAW (*bottom*) acquisition modes, along with their corresponding FFSAR spectra, plotted in polar coordinates for data acquired in the vicinity of the Hawaiian Islands. The gray arrow indicates the satellite's flight direction. ERA5-modeled wave and wind parameters (black) and FFSAR-derived peak wave period (light pink) are also shown.

A comparison of SAR altimetry modulation spectra reveals that for waves propagating

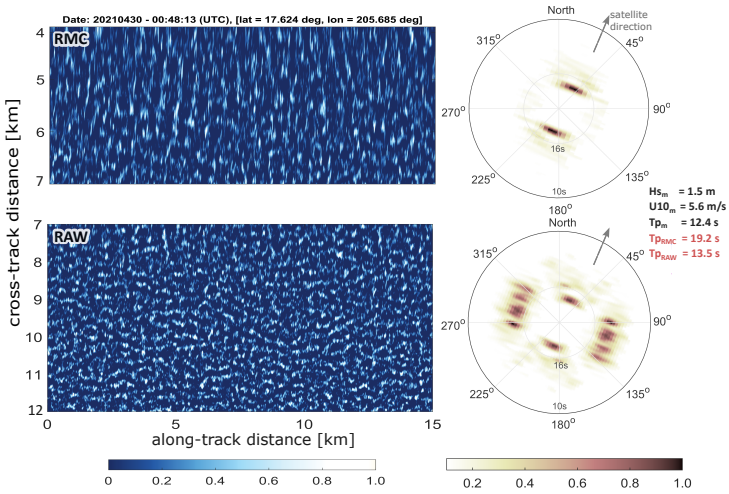

Figure 2.6: Swells in *cross-track*: projected waveform-tail radargrams for RMC (*top*) and RAW (*bottom*) acquisition modes, along with their corresponding FFSAR spectra, plotted in polar coordinates for data acquired in the vicinity of the Hawaiian Islands. The gray arrow indicates the satellite's flight direction. ERA5-modeled wave and wind parameters (black) and FFSAR-derived peak wave period (light pink) are also shown.

along the track, both RMC and RAW modes closely match the ERA5-derived peak wave period. In this scenario, the extended cross-track window of RAW does not provide additional information, as no significant wave energy is expected around this propagation angle. However, for cross-track propagating swells, only the RAW signals capture the dominant swell system, with an estimated peak period of 13.5 seconds, while both RMC and RAW detect a secondary peak at approximately 19.2 seconds.

This finding becomes even more apparent in Figure 2.7, where both cases involve swells travelling cross-track. Under moderate wind conditions (i.e., above 6 m/s), it appears that RMC exhibits noisy low-frequency signals, resulting in an overestimation of peak wave period by approximately 3 seconds compared to ERA5 data. Conversely, the RAW-mode radargrams, where wave modulations are clearly depicted, exhibit significantly reduced noise and peak wave periods that match modeled values within a 1-second margin. This analysis showcases the advantages of the increased ground resolution offered by the full-beam footprint of Sentinel-6A, particularly when waves propagate in or near the cross-track direction. The implications of along-track resolution loss are explored in detail in Chapter 3.

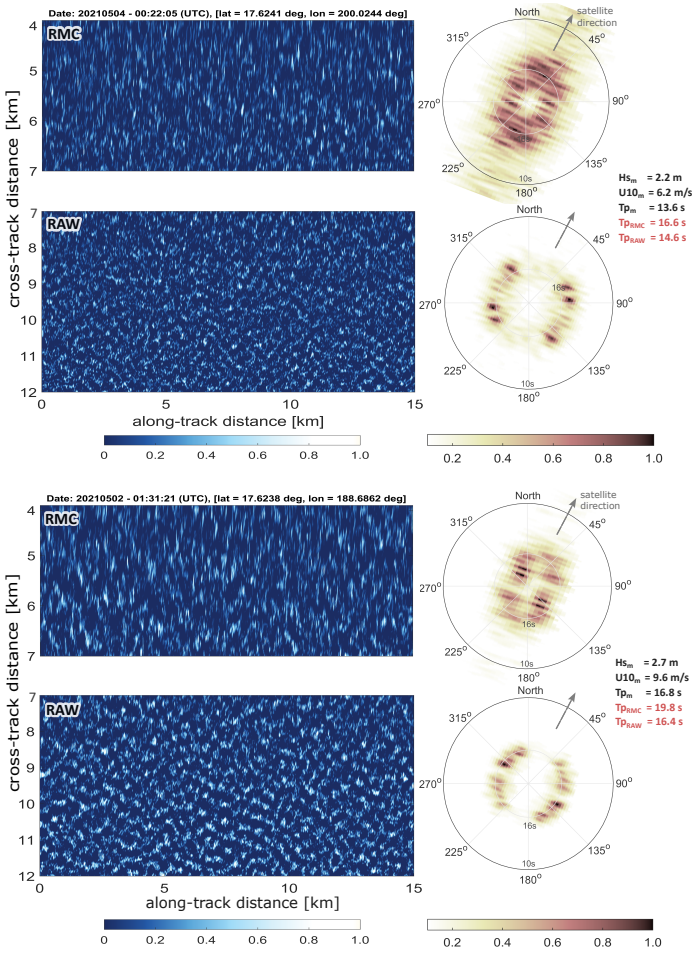

Figure 2.7: Two examples of projected waveform-tail radargrams from RMC and RAW acquisition modes, each accompanied by their corresponding FFSAR spectra, plotted in polar coordinates. Data correspond to acquisitions in the vicinity of the Hawaiian Islands. In both cases, swells are observed traveling *cross-track*. The gray arrow indicates the satellite's flight direction. ERA5-modeled wave and wind parameters (black) and FFSAR-derived peak wave period (light pink) are also shown.

2.5 Conclusions and Recommendations

This chapter presented a method to compute SAR spectra from FFSAR altimetry data and discussed the spectral response with the help of analytical and numerical modeling. FF-SAR radargrams of CryoSat-2 data showed modulations of power in the trailing edge of the waveforms in the presence of swells. A normalization of the intensity and a re-projection of the range bins as a cross-track location allowed for a spectral analysis in a similar way as for side-looking SAR systems. Features of the FFSAR spectra were compared to a model developed for side-looking SAR data.

Side-looking SAR spectra only have an ambiguity of 180 degrees. FFSAR altimetry spectra, however, exhibit power in four quadrants due to signals received from both sides of the ground track. In addition, the RAR response differs from that in a side-looking SAR system in terms of geometry and scattering mechanism. The largest term of RAR, range bunching, appears to be at the same order of magnitude and often even larger than the velocity bunching spectral response, depending on the wave height and direction. The inversion of an FFSAR altimetry spectrum into an ocean-wave spectrum requires a better understanding of the RAR response.

SAR altimeters show potential as an additional means to retrieve long-wave spectra. Having currently four SAR altimeters in orbit, *i.e.,* CryoSat-2, Sentinel-3A/B and Sentinel-6, the dataset available for studying swell will be greatly expanded. Notably, the exploitation of Sentinel-6A's full-beam footprint offers significant advantages for swell retrieval when waves propagate in or near the cross-track direction, benefiting from the extended window and enhanced ground resolution compared to the operational RMC data. As swell waves can be observed from two different instruments operating at different frequencies the SAR and RAR responses can be studied in more detail by looking at cross-overs between side-looking SAR and altimeters. Besides that, the sampling is greatly enhanced, which is especially beneficial for the study of waves radiating from tropical cyclones. Finally, the scaled integral of FFSAR derived long-wave spectra provides an estimate of significant wave height for swell only. In combination with the significant wave height obtained from low-resolution mode altimetry, we can discriminate between swell- and wind-wave heights.

2.6 Supporting Material

This supporting (S) material consist of an extended discussion about the selection of the low-pass filter used to normalize the radargrams as well as a step-by-step description of how the radargrams and the spectra are simulated, accompanied by the corresponding results. S1 and S3 are presented here as published, whereas part of S2, consisting of animated figures, is available in the digital version of the publication (see "Supporting Information": `https://doi.org/10.1029/2021GL096224`).

S1: Low-pass filter evaluation

Figure S1 shows four FFSAR spectra, as computed for case 2 (upper panels) and case 3 (bottom panels) in the main text, showing that a choice of a Gaussian low-pass filter of width ± 10 comparable to that used in the main text (filter width = 51), does not affect the spectra for swell wavelengths ranging from approximately 250 m to 600 m.

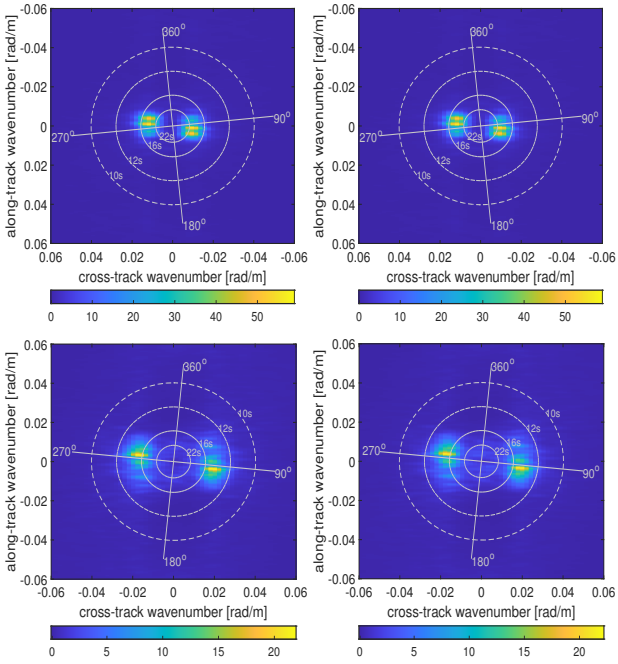

Figure S1: FFSAR spectra for case 2 *(upper panels)* and case 3 *(bottom panels)* of the main text after applying different filters to the radargrams. Left column: Gaussian low-pass filter of width = 41, right column: Gaussian low-pass filter of width = 61.

S2: Successive FFSAR waveform-tail radargrams and modulation spectra of Cryosat-2 along the track

Several altimetry additional observations have been examined across the globe and provided in GIFs. The swell cases were identified using the CMEMS swell monitoring products (`http://satwave-report.cls.fr/`). The chosen locations are shown in Figure S2. Each GIF contains a set of successive normalized/projected waveform-tail radargrams with the associated modulaton spectra.

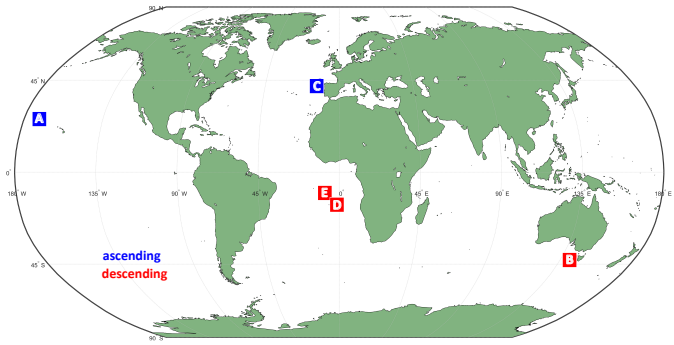

Figure S2: Global map illustrating the locations of 5 (A-E) additional swell cases.

S3: Simulations of FFSAR waveform-tail radargram and modulation spectra

Several simulations have been carried out to better understand the altimeter response. The RAR responses are hydrodynamic modulation, tilt modulation and range bunching. According to Jackson *et al.* [64] and Li *et al.* [57], the hydrodynamic modulation can be considered negligible compared to the other effects for nadir and near-nadir looking systems and, therefore, we do not take it into account in our simulations.

Tilt Modulation

To estimate the magnitude of the tilt modulation we use the geometrical optics approximation [58, 65]. Under an isotropic Gaussian assumption for the sea surface slope distribution, we estimate the normalized radar cross section (NRCS) as given by Nouguier *et al.* [66]:

$$\sigma_0 = \left(\frac{|R|^2}{s^2}\right)(sec^4\theta)\ exp\left(\frac{-tan^2\theta}{s^2}\right) \tag{2.7}$$

where θ is the radar incidence angle, s the mean square slope and R the Fresnel coefficient at normal incidence. Note that both R and s relate to wind speed, and thus we estimate them for 5,10 and 15 m/s wind speeds to investigate its impact in various wind seas. In particular, we estimate R as given by [67] (Eq. 4) and s based on the Cox and Munk clean surface relationship [68, 69]. Note that θ takes values within the range shown in Figure 2.1 of the main text. Figure S3.1 represents the NRCS variations from its mean value

as a function of the cross-track altimeter footprint, for its left and right sides. The dark and light blue dashed lines represent the crest and valleys, respectively, of a monochromatic wave of 2 m significant wave height and 400 m wavelength. The results show that the NRCS variations concern only 1.5-3.0% of the mean NRCS, which implies that the tilt modulation is an order smaller than the range and velocity bunching. Therefore, tilt modulation will be ignored in the further analysis.

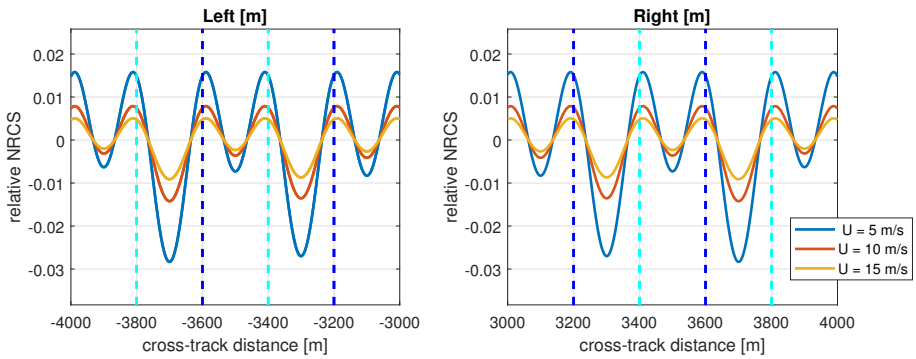

Figure S3.1: NRCS variations from the mean NRCS as a function of the cross-track altimeter footprint for 5, 10 and 15m/s wind speeds.

Velocity and range bunching

In order to understand the velocity bunching and range bunching imaging mechanisms for the nadir-looking altimeter we simulate radargrams for a monochromatic swell wave and a surface generated from a narrow Gaussian spectrum. Note, that we do not include a wind wave spectrum, as it would complicate the interpretation of the results. A wind wave spectrum would increase the velocity variance and therefore effectively reduce the resolution. The secondary peaks, which are present in this analysis, will often be suppressed to the noise level. The swell characteristics are set to be of 400 m wavelength, which is almost equal to a wave period (T) of 16 s, and 2 m and 4 m significant wave height so that they are comparable to those we show in the main text. Four scenes are produced per surface type based on different wave propagating angles with respect to the satellite track (0, 30, 60, 90 degrees). We consider three scenarios, i.e., a) range bunching and velocity bunching, b) velocity bunching only and c) range bunching only to give a first-order approximation of the magnitude of each contribution separately, but also, of their combination.

From sea surface generation to Level-1 FFSAR waveforms

A surface is generated on a square grid of 5 m x 5 m resolution ranging from 2500 to 8000 m across track, which is later cropped from 4000 to 7000 m across track to avoid edge effects. A similar crop is done in the along-track direction. Using the elevation and the cross-track distance, the distance from each scatterer to the satellite is computed. Next to a surface elevation η (Eq. 2.8), we compute vertical surface velocity v_r (Eq. 2.9), which is the derivative of the surface with respect to time and therefore 90 degrees out-of-phase

with the elevation. We multiply the velocity with the reciprocal of the angular velocity $\beta = \frac{R}{V}$ to compute the shift dy of each point in azimuth to simulate the velocity bunching (Eq. 2.10). Then, the scatterers are grouped into batches of 20 m along track to simulate the along-track multilooking. Each 'echo' representing 20 m along-track gets resampled based on the range bin sampling of the altimeter (0.234 m for CryoSat-2) by computing a histogram. Note that this histogram does not replicate the altimeter impulse response function and therefore the results are only a first-order approximation of the response. The normalization, projection, resampling and spectra filtering are done in the same way as in the main text.

$$\eta(x,y) = A\cos(x_k + y_k + \theta) \tag{2.8}$$

$$v_r(x,y) = \omega A\sin(x_k + y_k + \theta) \tag{2.9}$$

$$dy = \beta v_r \tag{2.10}$$

where A is the amplitude, ω the wave angular velocity, k_x and k_y the cross- and along-track wavenumbers, respectively, and θ phases that are taken randomly from the interval $[0, 2\pi]$.

Discussion

Below, Figures S3.2A-S3.3B represent each the simulated radargrams and spectra for propagating angles of 0 and 30 (S3.xA) , 60 and 90 (S3.xB) degrees as obtained from a monochromatic swell of 2 and 4 m significant wave height (Hs), respectively, for the range bunching scenario. Figures S3.4A-S3.6B and S3.7A-S9B represent each the simulated radargrams and spectra for the aforementioned propagating angles as obtained from the Gaussian derived scene with swell significant wave height of 2 and 4 m, respectively, for all three scenarios. Note that expected spectra are computed for the complex Gaussian scenes as well, after averaging 100 spectra derived each by a different Gaussian derived scene.

In general, both range and velocity bunching appear to be significant. In particular, they both reveal strong signals at intermediate angles. The velocity bunching is much stronger than the range bunching for along-track propagating waves, while velocity bunching disappears for cross-track propagating waves (Figures S3.5A-S3.6B and S3.8A-S3.9B). The spectra are a result of a statistical process which can lead to deviations from the expected value. For waves propagating in the along-track direction the range bunching is nearly zero, but a small signal remains as crests and troughs are captured in different range bins, with different projected cross-track resolution. It is also observed that even for a monochromatic wave the spectral response is smeared as we might have two maxima on one slope with a distance between them that depends on wavelength, amplitude and direction (Figures S3.2A-S3.3B). Lastly, for small significant wave heights there is one maximum near the slope maximum (Figures S3.2A/S3.2B), but if the slopes are larger than the incident angle, two maxima appear that move towards the crest and the trough (Figures S3.3A/S3.3B).

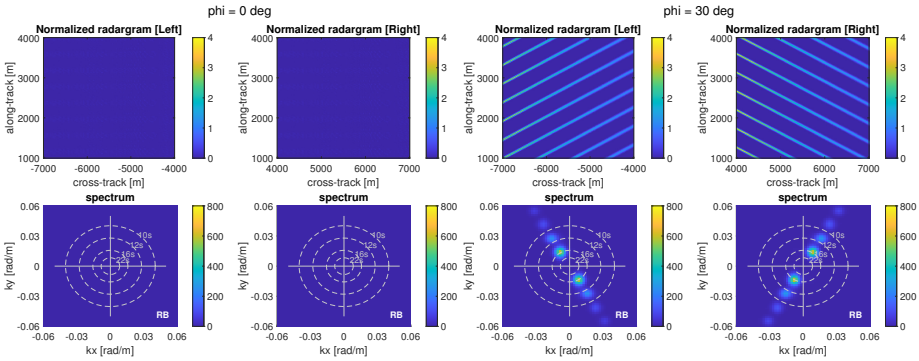

Figure S3.2A: *RB – Monochromatic swell* (T = 15 s, Hs = 2 m): simulated radargrams and spectra for propagating angles of 0 and 30 degrees.

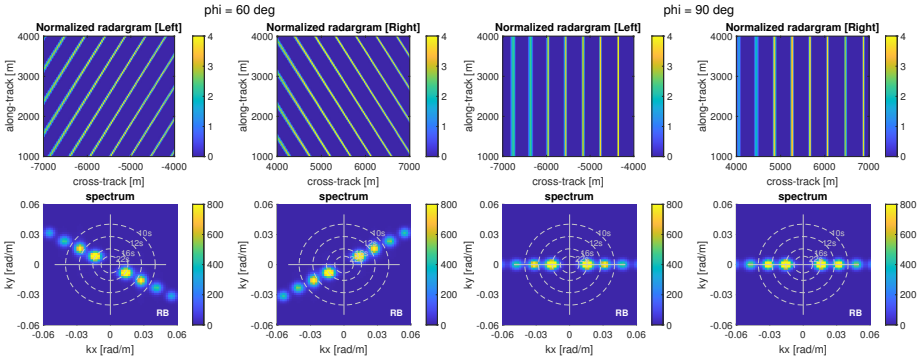

Figure S3.2B: *RB – Monochromatic swell* (T = 15 s, Hs = 2 m): simulated radargrams and spectra for propagating angles of 60 and 90 degrees.

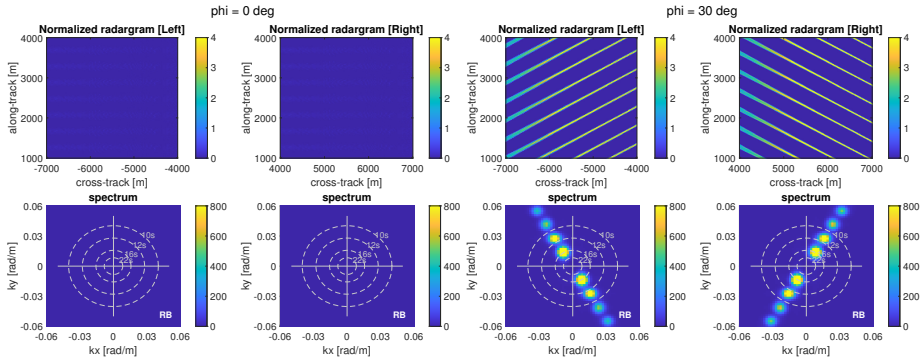

Figure S3.3A: *RB – Monochromatic swell* (T = 15 s, Hs = 4 m): simulated radargrams and spectra for propagating angles of 0 and 30 degrees.

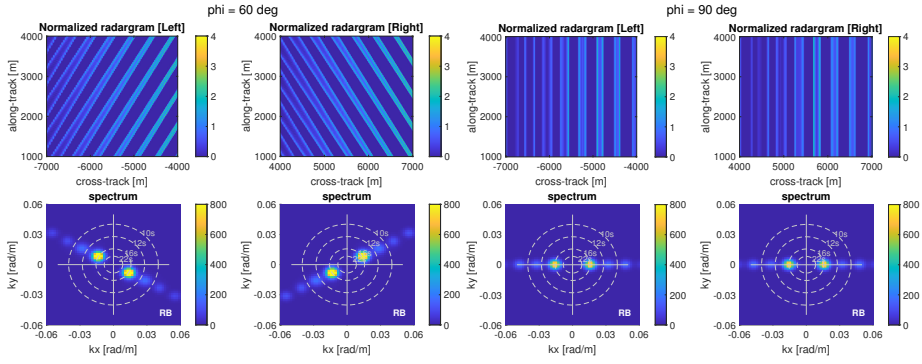

Figure S3.3B: *RB – Monochromatic swell* (T = 15 s, Hs = 4 m): simulated radargrams and spectra for propagating angles of 60 and 90 degrees.

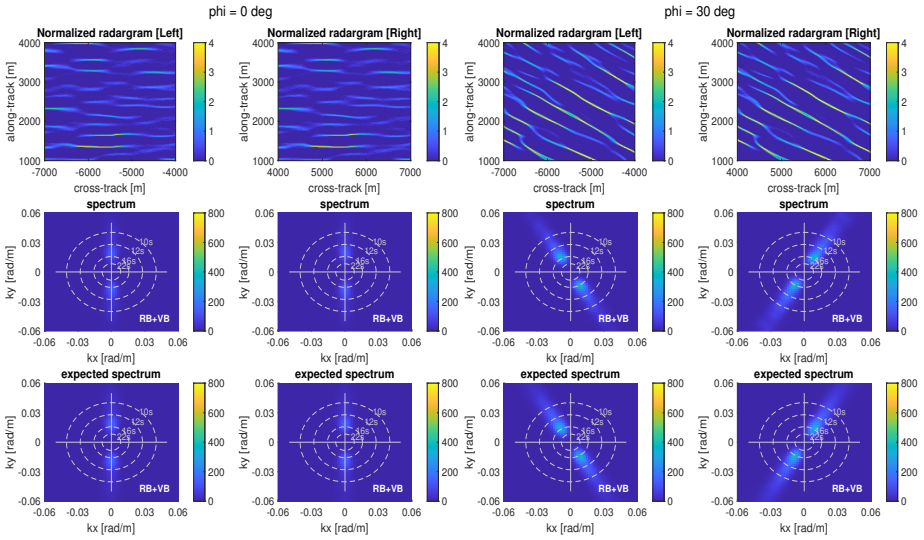

Figure S3.4A: *RB+VB – Gaussian derived scene* (T = 15 s, Hs = 2 m): simulated radargrams and spectra for propagating angles of 0 and 30 degrees.

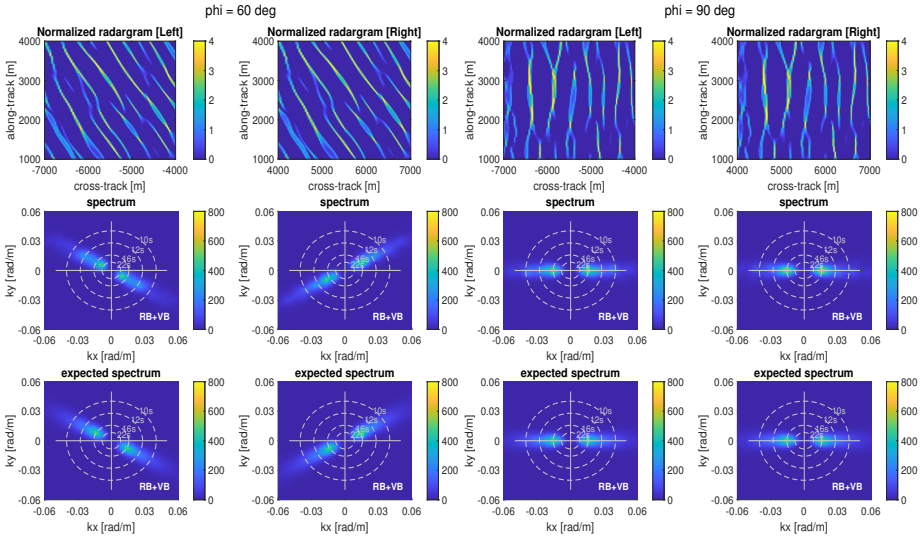

Figure S3.4B: *RB+VB – Gaussian derived scene* (T = 15 s, Hs = 2 m): simulated radargrams and spectra for propagating angles of 60 and 90 degrees.

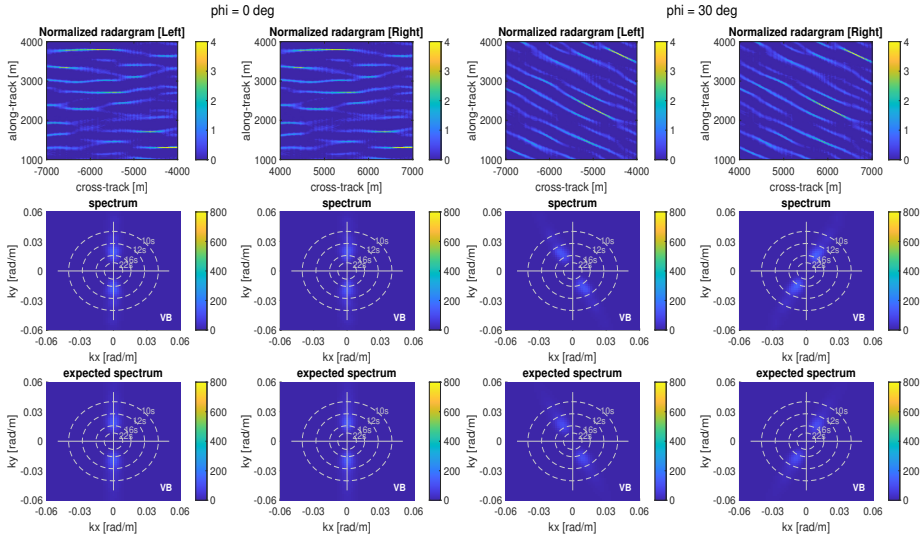

Figure S3.5A: *VB – Gaussian derived scene* (T = 15 s, Hs = 2 m): simulated radargrams and spectra for propagating angles of 0 and 30 degrees.

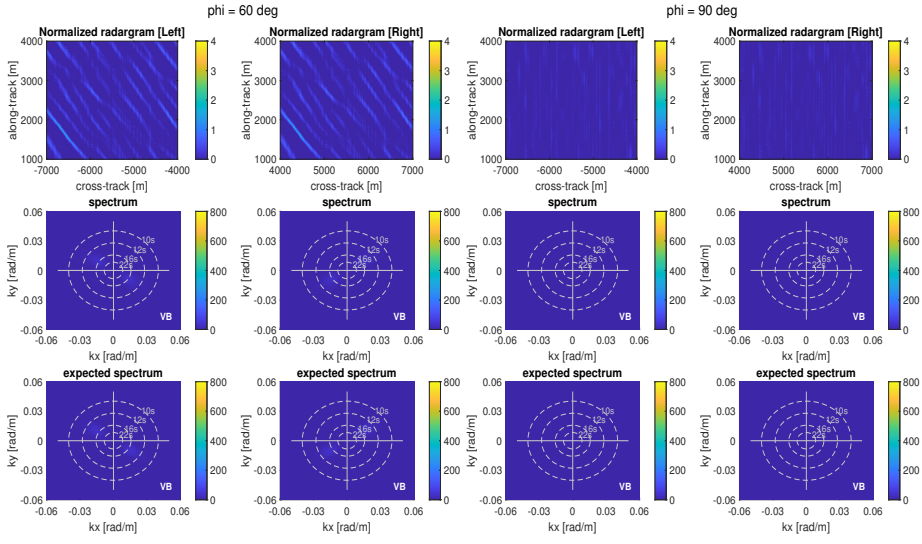

Figure S3.5B: *VB – Gaussian derived scene* (T = 15 s, Hs = 2 m): simulated radargrams and spectra for propagating angles of 60 and 90 degrees.

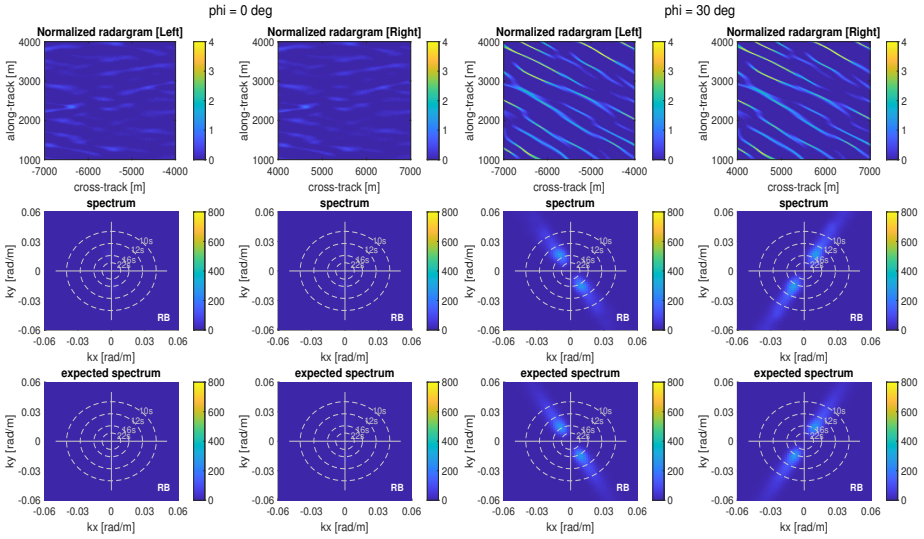

Figure S3.6A: *RB – Gaussian derived scene* (T = 15 s, Hs = 2 m): simulated radargrams and spectra for propagating angles of 0 and 30 degrees.

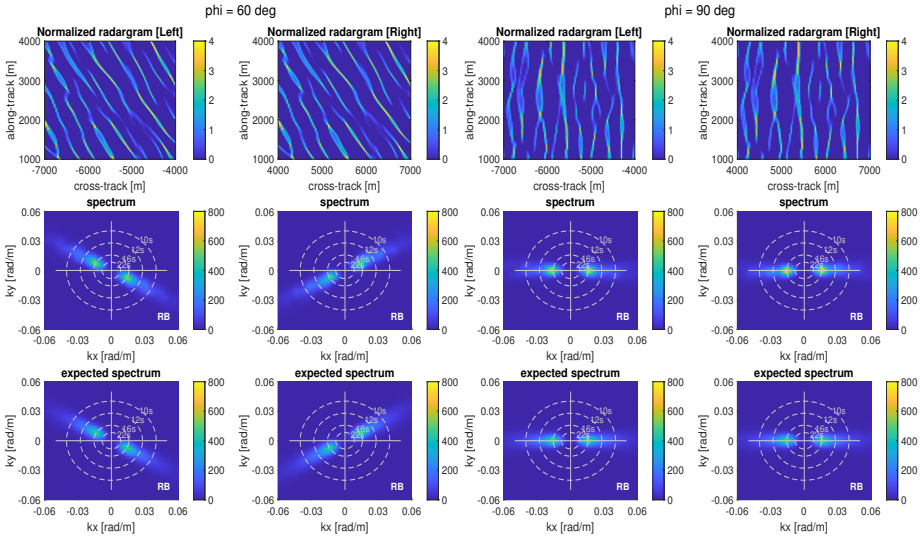

Figure S3.6B: *RB – Gaussian derived scene* (T = 15 s, Hs = 2 m): simulated radargrams and spectra for propagating angles of 60 and 90 degrees.

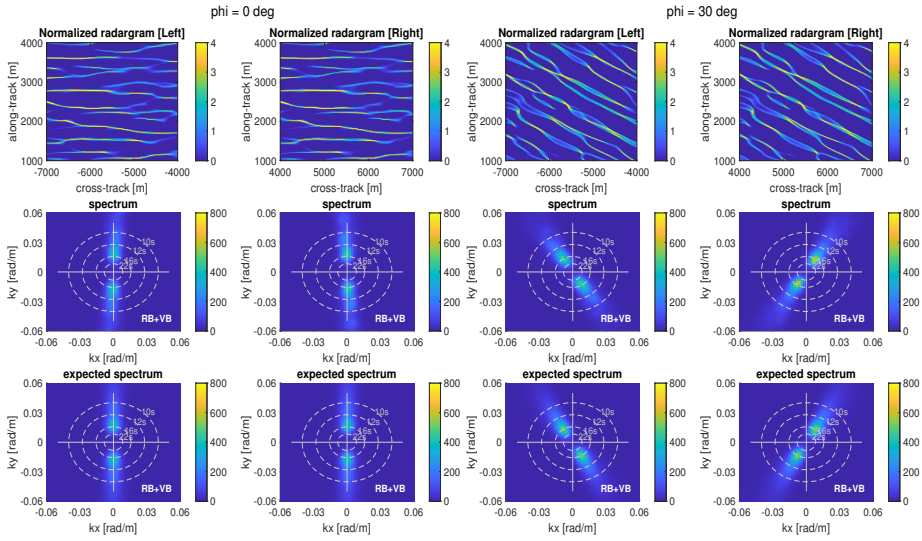

Figure S3.7A: *RB+VB – Gaussian derived scene* (T = 15 s, Hs = 4 m): simulated radargrams and spectra for propagating angles of 0 and 30 degrees.

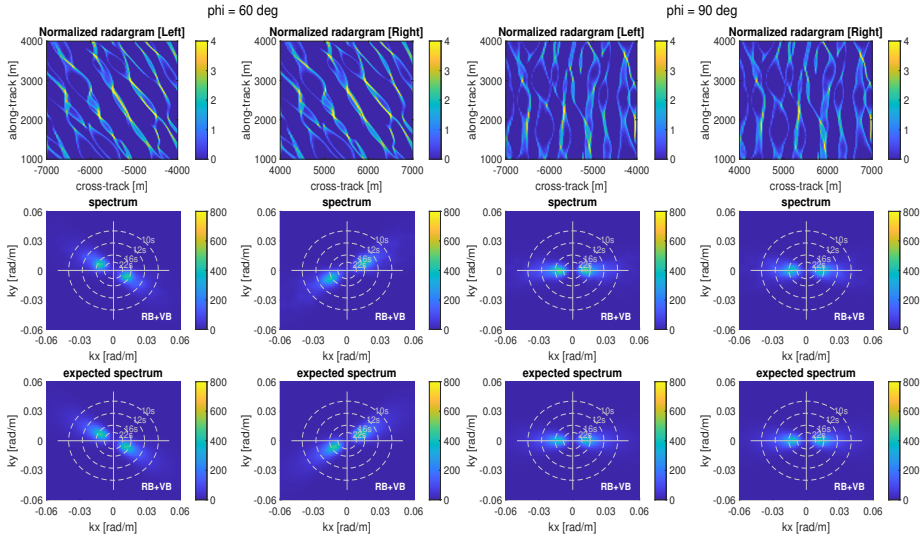

Figure S3.7B: *RB+VB – Gaussian derived scene* (T = 15 s, Hs = 4 m): simulated radargrams and spectra for propagating angles of 60 and 90 degrees.

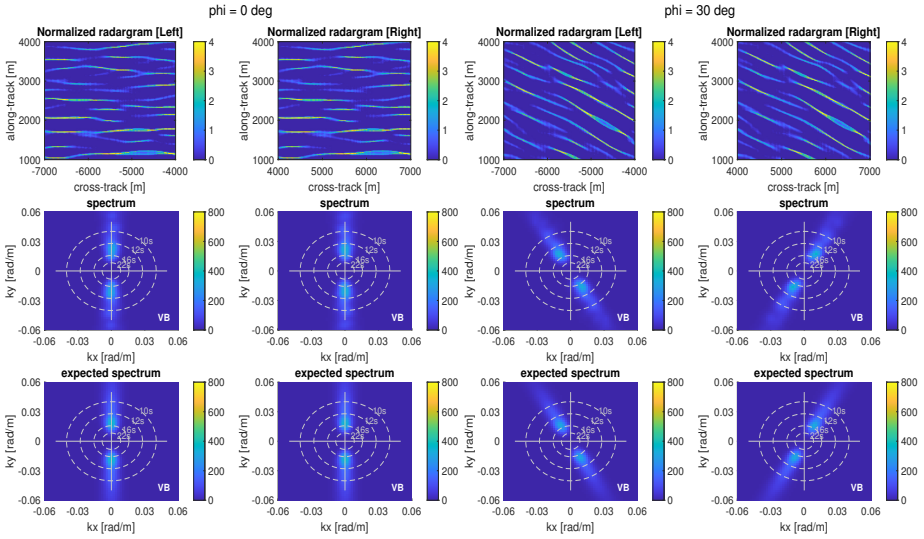

Figure S3.8A: *VB – Gaussian derived scene* (T = 15 s, Hs = 4 m): simulated radargrams and spectra for propagating angles of 0 and 30 degrees.

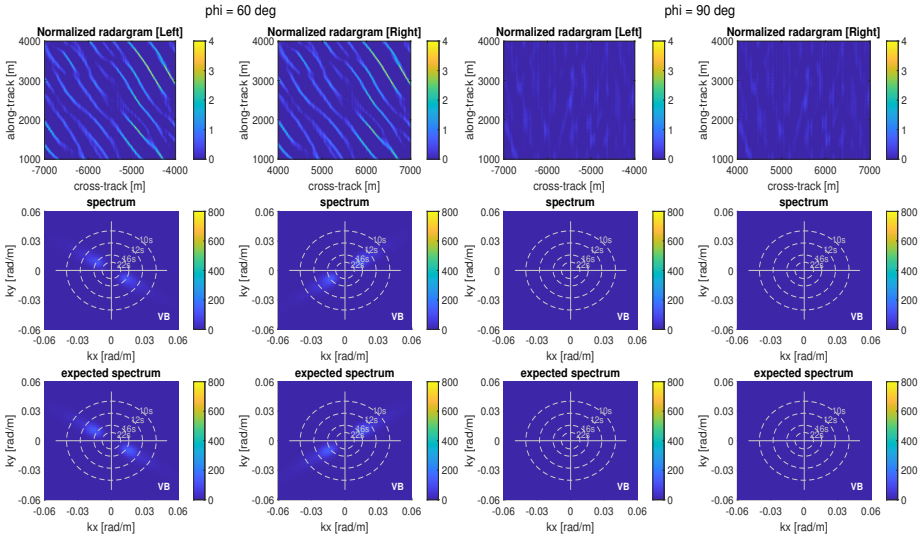

Figure S3.8B: *VB – Gaussian derived scene* (T = 15 s, Hs = 4 m): simulated radargrams and spectra for propagating angles of 60 and 90 degrees.

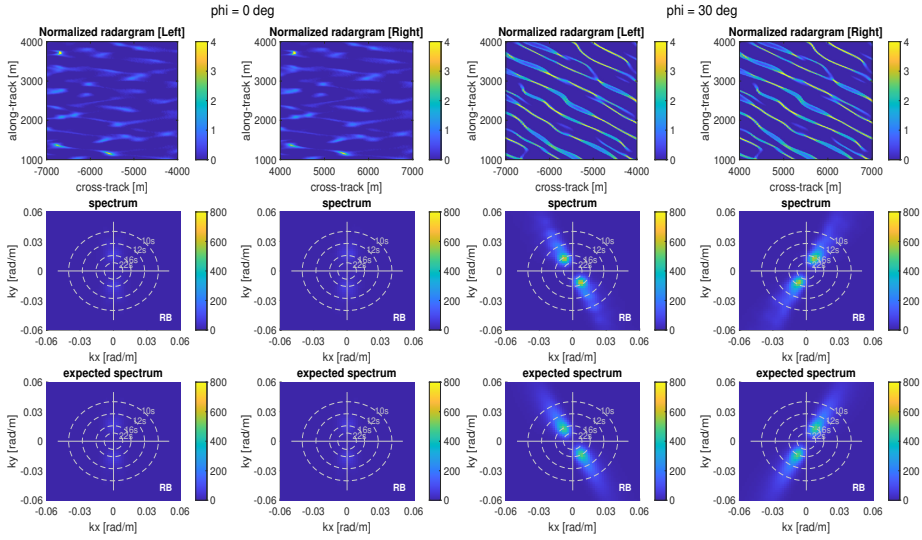

Figure S3.9A: *RB – Gaussian derived scene* (T = 15 s, Hs = 4 m): simulated radargrams and spectra for propagating angles of 0 and 30 degrees.

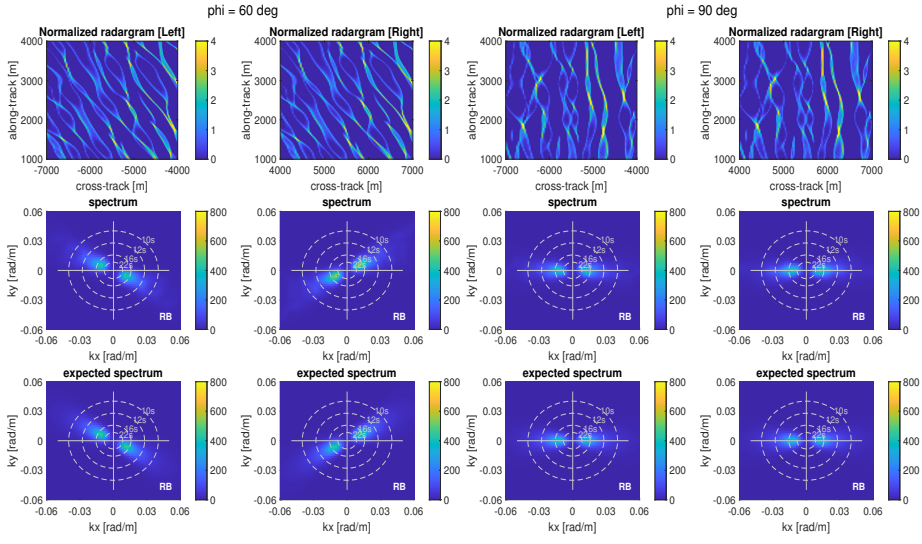

Figure S3.9B: *RB – Gaussian derived scene* (T = 15 s, Hs = 4 m): simulated radargrams and spectra for propagating angles of 60 and 90 degrees.

3

Introducing the Azimuth Cutoff as an Independent Measure for Characterizing Sea-State Dynamics in SAR Altimetry

This study presents the first azimuth cutoff analysis in Synthetic Aperture Radar (SAR) altimetry, aiming to assess its applicability in characterizing sea-state dynamics. In SAR imaging, the azimuth cutoff serves as a proxy for the shortest waves, in terms of wavelength, that can be detected by the satellite under certain wind and wave conditions. The magnitude of this parameter is closely related to the wave orbital velocity variance, a key parameter for characterizing wind-wave systems. We exploit wave modulations exhibited in the tail of fully-focused SAR waveforms and extract the azimuth cutoff from the radar signal through the analysis of its along-track autocorrelation function. We showcase the capability of Sentinel-6A in deriving these two parameters based on analyses in the spatial and wavenumber domains, accompanied by a discussion of the limitations. We use Level-1A high-resolution Sentinel-6A data from one repeat cycle (10 days) globally to verify our findings against wave modeled data. In the spatial domain analysis, the estimation of azimuth cutoff involves fitting a Gaussian function to the along-track autocorrelation function. Results reveal pronounced dependencies on wind speed and significant wave height, factors primarily determining the magnitude of the velocity variance. In extreme sea states, the parameters are underestimated by the altimeter, while in relatively calm sea states and in the presence of swells, a substantial overestimation trend is observed. We introduce an alternative approach to extract the azimuth cutoff by identifying the fall-off wavenumber in the wavenumber domain. Results indicate effective mitigation of swell-induced errors, with some additional sensitivity to extreme sea states compared to the spatial domain approach.

3.1 Introduction

A thorough understanding of sea-state conditions requires accurate measurements of ocean-surface parameters on a global scale. Over the past few decades, satellite altimeters, including both Low Resolution Mode [10] and Synthetic Aperture Radar (SAR) [3], have played a crucial role in providing geophysical parameters, such as wind speed, significant wave height, and sea surface heights. Despite advancements, accurate characterization of the sea state remains challenging. Explicit evidence of this is the primary error source in sea surface height, referred to as sea-state bias [70, 71, 72, 73]. Several methods rely on parametric models expressing this bias as a function of wind speed and significant wave height [74, 75, 76, 77, 78, 79, 73, 80, 81]. Although significant improvements have been reported over the years, persisting errors still exist, typically a few percentages of the significant wave height, a magnitude considered substantial within the sea level error budget [82].

Considering that different scales of ocean waves respond uniquely to variations in wind, currents, and other oceanic processes, including wave breaking, a more diverse set of observations is essential for an accurate characterization of ocean surface dynamics. Several studies have reported the sensitivity of SAR altimeter responses to sea surface motion [83, 60, 15, 84, 85]. Notably, a recent study demonstrated the possibility of extracting vertical wave particle velocity information from the radar signal [86]. Wave orbital velocity primarily results from the fast vertical motions of long and mid-wavelength wind waves and less from swells. For instance, a 500 m swell system with a 3 m significant wave height contributes approximately 0.1 m^2 s^{-2} to the total variance of the wave orbital velocity, while a moderate wind sea system, featuring an 11 m/s wind speed, 80 m wavelength, and 2 m wave height, contributes approximately 0.6 m^2 s^{-2}—six times more than the swell system [53]. On the other hand, the normalized radar cross section (NRCS), derived from waveform power, is mostly sensitive to mid to short-wavelength wind waves which strongly contribute to the mean square slope, a parameter describing the sea surface roughness [87, 88]. Using parametrizations, the NRCS is coupled to near-surface winds [89, 90]. Significant wave height encompasses contributions from long wind waves and swell, yet discriminating between these two wave systems remains a challenge. Given that higher velocity variance is associated with increased wind speed and larger wind waves, it becomes evident that incorporating this parameter can aid in distinguishing between wave components and, consequently, contribute to effectively constraining wind-wave systems.

Side-looking SAR systems have demonstrated their capability to extract wave orbital velocity information from the NRCS using image processing techniques [27]. These instruments image waves by leveraging Doppler misregistrations, resulting from the relative motion of the satellite and surface targets [25]. In side-looking SAR, the primary intensity modulation mechanism, known as velocity bunching, originates from Doppler misregistrations [44, 24, 25]. Scatterers move toward or away from the satellite, causing displacements in the SAR image. The magnitude of these displacements depends on the line-of-sight velocities of the wave particles and the range-to-platform velocity ratio [91, 24, 26]. The relatively high velocities of wind waves lead to large and random scatterer displace-

ments, causing a blurring effect in the SAR images [56] and effectively degrading the resolution in azimuth [92, 93, 25]. By quantifying this resolution loss, the so-called velocity variance of the wave field can be estimated. This quantification is typically realized by fitting a Gaussian function to the along-track autocorrelation, resulting in the estimation of the azimuth cutoff wavelength, a measure for the shortest waves that can be detected [26]. The relationship between azimuth cutoff and velocity variance has been exploited to constrain the wind-wave system using data from SAR imaging satellites, including Sentinel-1, ERS1/2, and Envisat [94, 27, 53, 52].

Although SAR altimeters have not been originally designed for wave imaging applications, recent studies reported their ability to capture long waves, such as swells [7, 84], using focusing algorithms [4, 47]. In particular, the trailing edge of the waveforms exhibits intensity modulations induced by long waves that can be exploited to compute SAR altimetry directional spectra [84], comparable to the methods applied to Sentinel-1 images [23, 46, 95]. Altimeters, however, experience due to their steep incident angles additional strong modulations from range bunching and a cutoff in the cross-track direction, depending on the significant wave height [84, 96]. This leads to a two-dimensional filter with a width and length depending on the significant wave height and velocity variance, respectively. Figure 3.1 displays four Sentinel-6A fully-focused SAR waveform-tail radargrams acquired under different wind and wave conditions. These radargrams are created by considering solely the trailing edge of multilooked waveforms, generated using a posting rate of 680 Hz, where intensity modulations are evident. In relatively moderate sea states and in the presence of swells, wave-like patterns are captured (top panels). As wind and significant wave height increase, the random wave orbital motion induces large scatterer misregistrations, resulting in a blurring effect (bottom panels), the nature of which proved to be more complex compared to SAR imaging due to the different measurement geometry, primarily related to the near-zero incident angle of SAR altimeters [96].

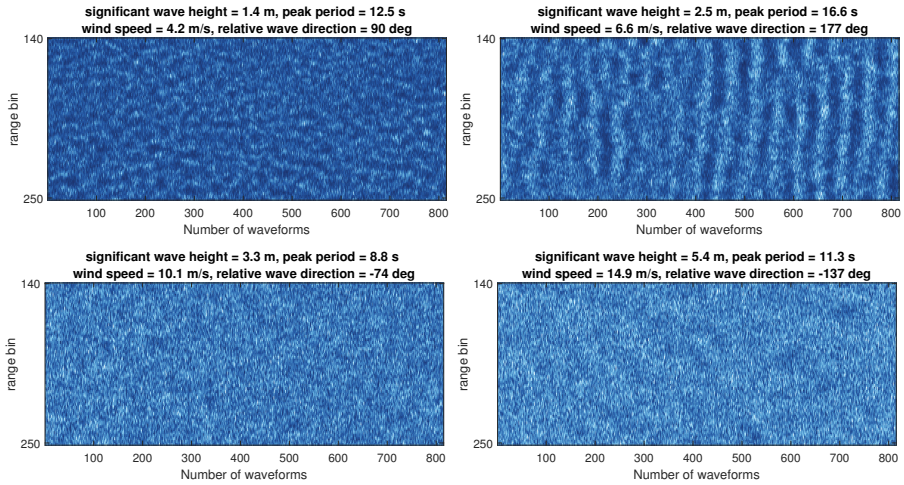

Figure 3.1: Examples of Sentinel-6A fully-focused SAR waveform-tail radargrams. Wind and wave conditions, given in the title of each panel, obtained from ERA5 products.

In this work, we conduct the first azimuth cutoff analysis in SAR altimetry aiming to enhance our understanding of the SAR altimeters' capabilities in providing an additional metric for characterizing sea-state dynamics. This article is organized as follows. Section 3.2 discusses the processing steps of both the altimeter data, from Level-1A products to fully-focused SAR waveform-tail radargrams, and the European Centre for Medium-Range Weather Forecasts Reanalysis v5 (ERA5) [63] and Météo France Wave Model (MF-WAM) [97, 98] data used to evaluate our results. In Section 3.3, we describe the method used for the azimuth cutoff estimation in the spatial domain, evaluate our results against wave models, and identify sensitivities in this approach. In Section 3.4 we introduce an alternative method conducted in the wavenumber domain and perform a comparative analysis between the altimeter and wave model-derived parameters, similar to Section 3.3. In Section 3.5, we proceed with a qualitative comparison of the azimuth cutoff and velocity variance parameters with sea-state conditions and identify associated limitations in both methods. In Section 3.6 we discuss the main findings and provide recommendations for future research.

3.2 Data

This section is divided into two parts. The first part outlines the settings used for the focusing processing of the altimeter radar signal and the post-processing of the fully-focused SAR radargrams. The second part details the wave model parameters used to support our analysis.

3.2.1 Sentinel-6A Data Processing

Our analysis concerns processing of Level-1A data of one Sentinel-6A repeat cycle (No. 77), spanning from 11–21 December 2022. To produce Level-1b fully-focused SAR multilooked waveforms, which are the input for our methods, we use the Omega–Kappa focusing algorithm [47] implemented in an updated version of the Standalone Multimission Altimetry Processor [99]. The Omega–Kappa algorithm has demonstrated a substantial reduction in computational time by operating in the frequency domain, as opposed to the back-projection method that originally introduced the fully-focused processing technique in SAR altimetry [4]. The fully-focused SAR multilooked waveforms are obtained by (a) averaging consecutive single looks (i.e., 13 individual FFSAR waveforms) from a 9 kHz posting rate onto 680 Hz, corresponding to an approximately 12 m along-track spacing, (b) zero-padding in range by a factor of 2 to double the sampling rate of the waveform gate samples, and (c) using a Doppler bandwidth factor of 0.6 to effectively remove the aliased part of the Sentinel-6 spectrum [100].

The azimuth cutoff analysis is performed by considering only the trailing edge, where intensity modulations are observed. It is a fact that the fully-focused SAR processing algorithm enables the generation of high-resolution along-track independent looks theoretically equal to half of the antenna length [4], while the nominal cross-track ground resolution is uneven across the bins and increases as it obtains distance from the nadir. We

generate fully-focused SAR waveform-tail radargrams with dimensions of approximately 10 km in azimuth and 4.5 km in range. The range window corresponds to bins between 140 to 250, with the leading edge being around bin 100, and an off-nadir cross-track distance between 5 km and 9.5 km. Note that considering bins close to the leading edge, where the ground sampling resolution decreases, introduces the risk of averaging out wavelengths of the order of a few hundreds, thus affecting the cutoff estimation. As a last step, we fit a fifth-order polynomial model in the along-track for each range bin separately, and then subtract it from the initial signal, aiming to remove trends related to wind speed anomalies occurring within the 10 km segment in along-track.

3.2.2 Wave Models

Due to the limited availability of in situ data in open oceans, we use ERA5 and MFWAM parameters for evaluation purposes. The use of two different products enables the cross evaluation of the results, taking into account that modeled data of different spatial and temporal resolutions can capture different aspects of oceanic conditions. In particular, we use wave spectra-derived integrated parameters, including significant wave height, peak wave period, mean zero-up crossing period, and mean wave direction obtained at spatial and temporal resolutions of 0.08 degrees every 3 hours from MFWAM and 0.50 degrees every hour from ERA5. To help in the interpretation of the results, we additionally use ERA5 wind speed estimates. The gridded parameters are bilinearly interpolated to the along-track Sentinel-6A measurement locations. Focusing our work on open oceans, we mask out areas where extremely calm sea states are expected, such as gulfs and inland waters. We empirically identify these areas by setting a lower peak wave period threshold at 8 seconds, using as reference the corresponding ERA5 parameter.

Figure 3.2 illustrates the global maps of the interpolated MFWAM (top panels) and ERA5 (bottom panels) significant wave height and mean zero-up crossing period to the Sentinel-6A tracks. These two parameters are used for the estimation of the model-derived azimuth cutoff and wave orbital velocity variance, as shown later. In terms of geographical patterns, the models display a high degree of resemblance. Table 3.1 provides correlation coefficients and statistics of the differences of these wave parameters between the models. Notably, the significant wave height and mean zero-up crossing period reveal a high correlation of 0.96 and 0.88, respectively. MFWAM parameters tend to be slightly higher; on average 0.12 m for the significant wave height and 0.35 s for the mean zero-up crossing period. Moreover, the standard deviation remains at relatively low levels at 0.38 m and 0.59 s, which represent 13% and 9% of the mean significant wave height and mean zero-up crossing period values, respectively, underlining the credibility of the evaluation process.

Table 3.1: Statistics of the differences and correlation coefficients between ERA5 and MFWAM wave parameters.

MFWAM−ERA5	Mean	Std. Dev.	Corr. Coef.
Significant wave height [m]	0.12	0.38	0.96
Mean zero-up crossing period [s]	0.35	0.59	0.88

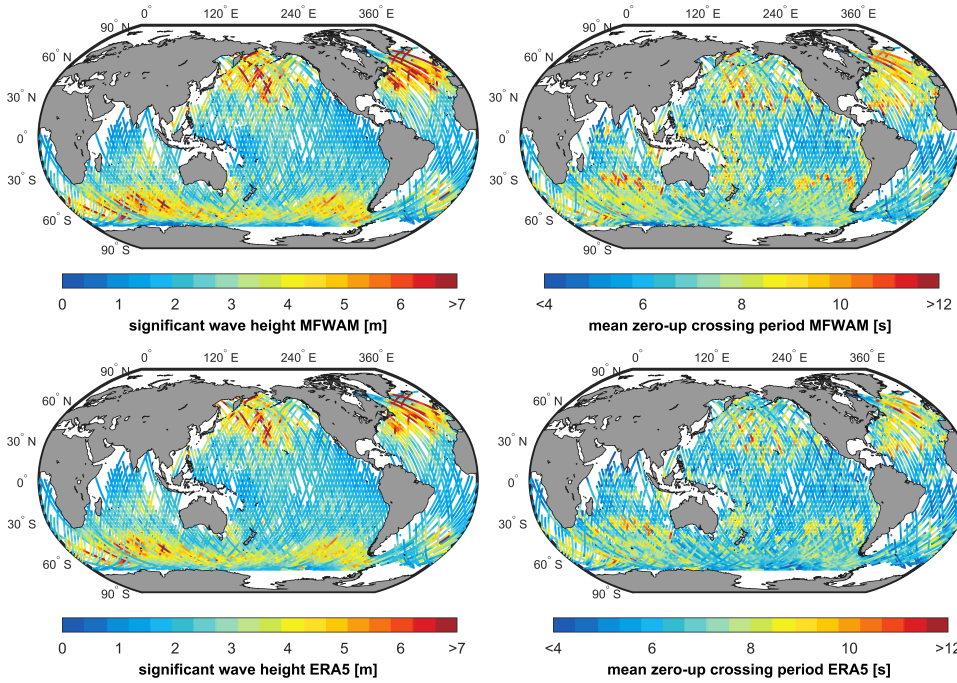

Figure 3.2: Interpolated significant wave height (*left column*) and mean zero-up crossing period (*right column*) parameters of MFWAM (*top row*) and ERA5 (*bottom row*) to Sentinel-6A tracks.

Discrepancies between the models can be attributed to several factors. Firstly, each model is expected to capture different scales of oceanic features based on their spatial and temporal resolutions. Secondly, distinct parametrization techniques contribute to model differences. And, thirdly, assimilation strategies vary significantly. MFWAM assimilates significant wave height observations from the altimeters Jason-3, SARAL, CryoSat-2, Sentinel-3 A/B, CFOSAT, and Sentinel-6A, as well as ocean-wave spectra from Sentinel-1 [101]. The ERA5 assimilates observations from SARAL and CryoSat-2 based on the operational stream [63].

The ocean surface wave orbital velocity variance $\sigma^2_{v,m}$ is approximated as a function of significant wave height, H_s, and mean zero-up crossing period, T_{02}, as [102]:

$$\sigma^2_{v,m} = \left(\frac{\pi}{2}\frac{H_s}{T_{02}}\right)^2 \tag{3.1}$$

To properly interpret this parameter we have to consider that both ERA5 and MFWAM have an upper frequency limit of approximately 0.55 and 0.58 Hz, respectively. This indicates that waves with wavelengths shorter than approximately 5 m are not resolved. To quantify the impact of this limitation, Figure 3.3 shows the ratio of the wave orbital velocity variance for waves exceeding this frequency limit, denoted as $\sigma^2_{v_{ww,hf}}$, to the total wind-driven velocity variance, denoted as $\sigma^2_{v_{ww}}$. These variables have been derived using Elfouhaily wind-generated wave spectra [103] in various fetches, while their ratio is presented as a function of wind speed. The fetch represents the distance over which the wind has been consistently blowing in a constant direction. Wind waves shorter than 5 m appear to have a rather significant contribution to the total velocity variance up to moderate wind conditions, exceeding 50% in cases characterized by relatively low wind conditions (<5 m/s).

Although our dataset mainly features moderate and high sea states, approximately 20% of the instances involve conditions with relatively low winds. In order to ensure a comprehensive representation of the total wave orbital velocity variance across all examined sea states, we incorporate the contribution of waves shorter than 5 m wavelengths into the model-derived estimates by implementing a spectral integration technique. Initially, the high-frequency wave orbital velocity variance (>0.55 and >0.58 Hz for ERA5 and MFWAM, respectively) is quantified using the wind-driven Elfouhaily wave model [103]. Subsequently, this is summed with the estimates derived from the ERA5 and MFWAM wave models.

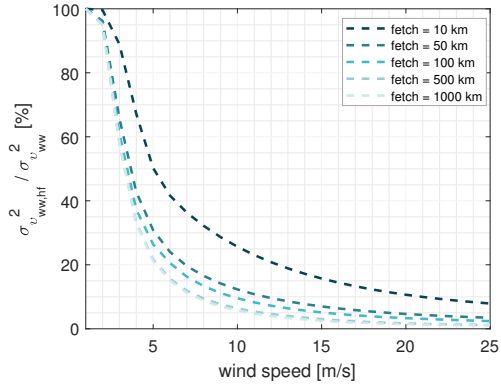

Figure 3.3: Ratio of the $\sigma^2_{v_{ww,hf}}$ wave orbital velocity variance of high-frequency waves (>0.58Hz) to the $\sigma^2_{v_{ww}}$ total wave orbital velocity variance versus wind speed. The colors represent the different fetches.

3.3 Azimuth Cutoff Analysis in the Spatial Domain

As mentioned earlier, random motions in the line-of-sight result in random scatterer displacements. These displacements cause a resolution loss that depends on range, R, and platform velocity, V. The measure describing the shortest detectable wavelength, known as azimuth cutoff λ_c, can be expressed as [95, 26, 104, 27]:

$$\lambda_c = \pi \frac{R}{V} \sqrt{{\sigma_v}^2} \tag{3.2}$$

where σ_v^2 is the line-of-sight-projected wave orbital velocity variance of the ocean surface. Theoretically, the wave orbital velocity variance can be computed using the integral of the two-dimensional wave spectrum, $S(k_x, k_y)$ as:

$${\sigma_v}^2 = \int \omega^2 S(k_x, k_y) dk_y dk_x \tag{3.3}$$

where ω represents the angular frequency computed as $\sqrt{gk}$ assuming deep water conditions, with $k = \sqrt{k_x^2 + k_y^2}$ the norm of the two-dimensional wavenumber (k_x, k_y) and g the gravitational constant. Now, to estimate the azimuth cutoff we implement a method in the spatial domain by minimizing the differences between the along-track autocorrelation function of a fully-focused SAR waveform-tail radargram and a Gaussian function as described in [26] and given as:

$$\Delta\varepsilon = \int dy \left\{ Rxx(y) - e^{-\left(\frac{\pi y}{\lambda_{c,SAR}}\right)^2} \right\} \tag{3.4}$$

where $Rxx(y)$ is the autocorrelation function in the along-track direction y, which is obtained by first computing the along-track autocorrelation for each range bin in the waveform-tail radargram separately and then averaging them over all selected bins.

Figure 3.4 shows the along-track autocorrelation function of a fully-focused SAR waveform-tail radargram. The scene is characterized by moderate wind and wave conditions, featuring long swells with a period of 14.5 s propagating at an angle with respect to the satellite azimuth direction. A closer examination of the autocorrelation shape reveals its decomposition into the summation of two distinct spread functions. In the proximity of zero-lag, the narrow point spread function is associated with speckle noise, while the wider Gaussian function's width is related to the azimuth cutoff [26]. To ensure an accurate estimate of the azimuth cutoff, the zero-lag is excluded from the model fitting process, as illustrated in Figure 3.4. As a last step, we estimate the velocity variance by simply rewriting Eq. 3.2 to

$$\sigma^2_{v,SAR} = \left(\frac{\lambda_c V}{\pi R}\right)^2 \tag{3.5}$$

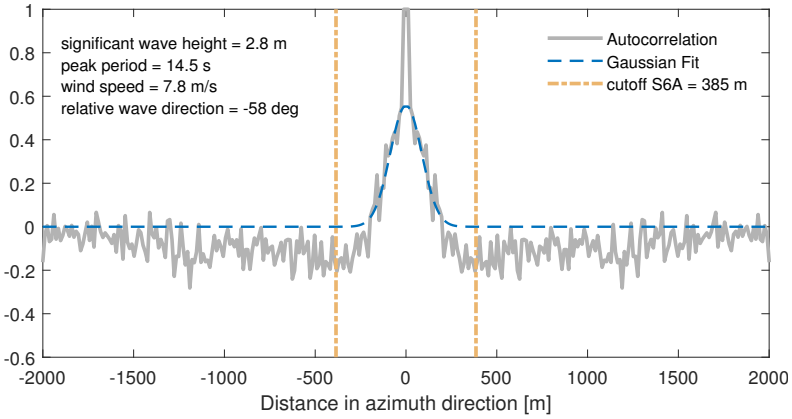

Figure 3.4: Example of the along-track autocorrelation function, depicted in gray color, of a Sentinel-6A (S6A) fully-focused SAR waveform-tail radargram acquired for a scene characterized by moderate wind and wave conditions. The blue dashed line represents the Gaussian function. The yellow dash-dotted lines represent the Sentinel-6A azimuth cutoff estimate. Sea-state conditions are obtained from ERA5 products.

Figure 3.5 provides a comparative illustration of the azimuth cutoff between Sentinel-6A and ERA5 (top-panels) and Sentinel-6A and MFWAM (bottom panels). The azimuth cutoff estimates for the wave models are derived from Eq. 3.2 with the substitution of σ_v^2 by Eq. 3.1. Values below 50 m are excluded as the Gaussian fitting is poorly conditioned. Both models exhibit similarly high levels of agreement with Sentinel-6A, with MFWAM revealing a smaller dispersion, indicating a closer match to the satellite-derived values. The color gradations correspond to wind speed and significant wave height in the left and right panels, respectively. The azimuth cutoff is notably correlated to sea state, exhibiting a clear increase with increasing significant wave height. To aid in the interpretation of observed trends, the altimeter-derived azimuth cutoff estimates are grouped into intervals of 50 m based on the modeled data and then averaged. The binned points are illustrated with the square markers linked with solid gray lines. An overestimation trend for values below 350 m and 400 m for ERA5 and MFWAM, respectively, is observed. This observation is most likely related to the significant amount of sporadic extremes in low azimuth cutoff model-derived estimates, identified for low-to-moderate sea states. For wavelengths above 350 m, the values are consistently underestimated compared to ERA5, while the underestimation trend in the MFWAM comparison is significantly smaller, noticeable only above 600 m. Based on ERA5 estimates, the same trend appears to relate to an increase in wind speed and wave height, in particular, above approximately 10 m/s and 3 m, but this is only confirmed by MFWAM when the wind speed and the wave height exceeds approximately 15 m/s and 5 m, respectively.

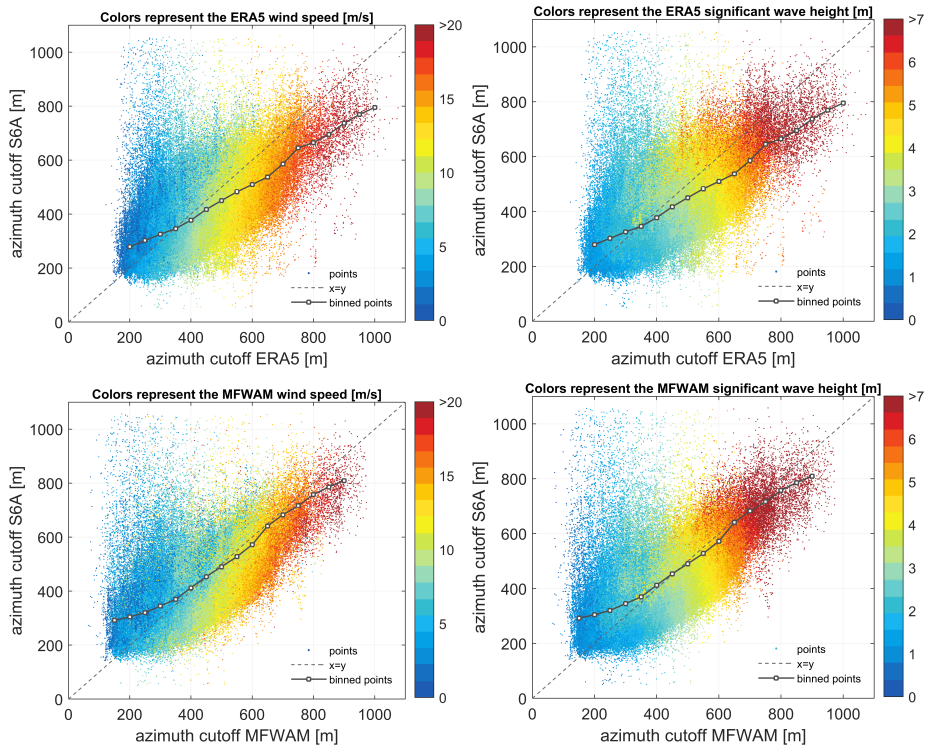

Figure 3.5: Scatter plots of the azimuth cutoff estimated by Sentinel-6A in comparison to ERA5 (*top panels*) and MFWAM (*bottom panels*). In the left and right panels, color gradations correspond to wind speed and significant wave height, respectively. The square markers linked with solid gray lines depict the average value of points grouped every 50 m considering wave model-derived intervals. The gray dashed lines represent the scenario where the azimuth cutoff of the satellite and wave model would align perfectly.

To further support the interpretation of these results we perform a sensitivity analysis based on different wind and wave conditions, the outcome of which is provided in Table 3.2. Overall, the altimeter azimuth cutoff estimates reveal moderate correlations between 0.6 and 0.7 with respect to ERA5 and MFWAM, respectively. The standard deviation of the differences is approximately 100 m, indicating a notable dispersion in the estimates. The method tends to overestimate the azimuth cutoff in relatively calm sea states (positive mean values), while the opposite holds for high sea states (negative mean values), as shown also in Figure 3.5. It is noticeable that for significant wave heights below 2 m and above 5 m there is a weak correlation between model and satellite-derived azimuth cutoff values, indicating the sensitivity of the Gaussian method in these oceanic conditions. It is worth noting that comparable findings have emerged from applying this method to Envisat's SAR images [27].

Table 3.2: *Spatial domain analysis*: statistics of the azimuth cutoff differences and correlation coefficients between Sentinel-6A and wave models based on a sensitivity analysis of the former to changes in wind speed, significant wave weight and a combination thereof. The values outside and inside parentheses represent ERA5 and MFWAM results, respectively.

Category	Points	Mean [m]	Std. Dev. [m]	Corr. Coef.
All data	318,590 (318,541)	−16.47 (−10.59)	101.84 (96.70)	0.67 (0.71)
Wind speed [m/s]				
U10 < 5	68,811 (68,794)	62.18 (63.08)	91.07 (93.67)	0.51 (0.51)
5 < U10 < 15	237,359 (237,327)	−32.65 (−27.71)	90.23 (86.14)	0.65 (0.70)
U10 > 15	12,420 (12,420)	−143.04 (−90.81)	95.64 (88.83)	0.65 (0.72)
Significant Wave Height [m]				
Hs < 2	78,345 (79,377)	12.19 (32.99)	95.17 (107.22)	0.07 (0.01)
2 < Hs < 5	224,755 (217,442)	−22.73 (−23.13)	100.29 (87.98)	0.48 (0.56)
Hs > 5	15,490 (21,722)	−70.62 (−44.83)	117.93 (90.75)	0.29 (0.48)
Significant Wave Height [m] and Wind Speed [m/s]				
2 < Hs and U10 < 5	36,167 (33,907)	52.80 (70.36)	94.28 (104.95)	0.14 (0.03)
2 < Hs < 5 and 5 < U10 < 15	188,088 (178,709)	−35.72 (−36.46)	91.30 (80.13)	0.51 (0.58)
Hs > 5 and U10 > 15	8226 (8043)	−126.12 (−87.94)	98.00 (77.78)	0.51 (0.70)

In order to gain a better understanding of the nature of these observations, we discuss some problematic autocorrelation examples in the following section.

Gaussian Fitting Limitations and Sensitivities

Figure 3.6 presents along-track autocorrelation examples for two cases, each accompanied by the corresponding fully-focused SAR waveform-tail radargram. The top panels illustrate a scenario in which the SAR altimeter underestimates the azimuth cutoff. In this instance, the wave model indicates a significant wave height of 5.2 m and a wind speed of 15.3 m/s based on ERA5 parameters. While the Gaussian function appears to provide a reasonable fit to the autocorrelation, the azimuth cutoff appears to be significantly underestimated by 157 and 204 m with respect to the MFWAM and ERA5 estimates, respectively. Considering that underestimation of wave orbital velocity variance is also expected, given the way we infer it through Eq. 3.2, one possible explanation for this observation is linked to the ocean surface geometry. In particular, a recent study reported that a nadir-looking system can capture only a fraction of the total distribution of vertical wave particle velocities, leading to its underestimation when velocity-slope dependencies are omitted [86], as is the case in our method. Note that, as the examined oceanic conditions correspond to wind seas characterized by large steepness, wave breaking can also contribute to additional errors.

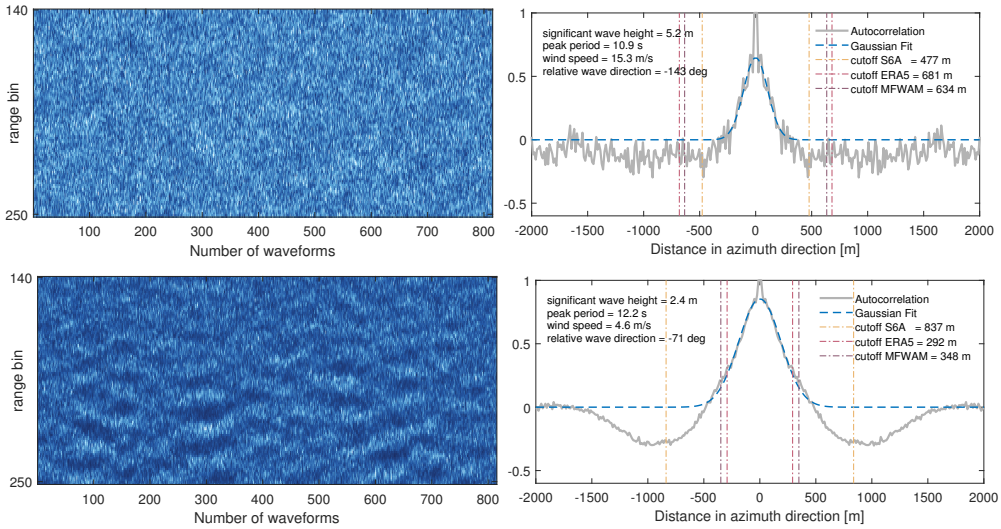

Figure 3.6: Examples of Sentinel-6A fully-focused SAR waveform-tail radargrams (*left panels*) and their along-track autocorrelation functions (*right panels*), illustrated in gray color. The blue dashed line represents the Gaussian function. The yellow, pink, and brown dash-dotted lines represent the Sentinel-6A, ERA5 and MFWAM azimuth cutoff estimates, respectively. Sea state conditions are obtained from ERA5 products.

Conversely, cases of extreme overestimation are mostly observed where the scene is characterized by relatively low wind speed and in the presence of swells. An example is given in the bottom panels of Figure 3.6. This case concerns a scene with significant wave height and wind speed of 2 m and 5 m/s, respectively, while the peak wave period of 12 s indicates the presence of swells traveling at 71 degrees angle with respect to the satellite azimuth direction. These long waves exhibit well-modulated patterns and appear to dominate the shape of the autocorrelation, causing it to widen the main lobe. Again, although the Gaussian function describes well the main lobe, the method cannot determine properly the azimuth cutoff, exhibiting differences on the order of 500 m for both models.

To investigate the sensitivity to swell presence, Figure 3.7 provides four examples where long waves propagate at different angles with respect to the satellite azimuth direction. The autocorrelation appears to become a sinc-shaped function, with the size of the side lobes dependent on the direction and magnitude of swells, leading to either narrowing or stretching the width of the main autocorrelation lobe. The projected wavelength of swell waves propagating near the cross-track direction will cause a signal projected in the along-track that is larger than that of a swell wave propagating in the along-track direction. For a similar cutoff the cross-track propagating swell waves will therefore widen the main lobe more than along-track propagating swell waves. In fact, it is probably unlikely that cross-track waves will make the main lobe more narrow as its projected wavelength is

also substantially larger than the along-track cutoff. In contrast, waves propagating along-track exhibit a more sinc-like behavior. Even though the wavelength of the visible waves must be larger than the cutoff, thus an overestimation might be expected, fitting a Gaussian into the sinc-shaped signal might lead to an underestimation.

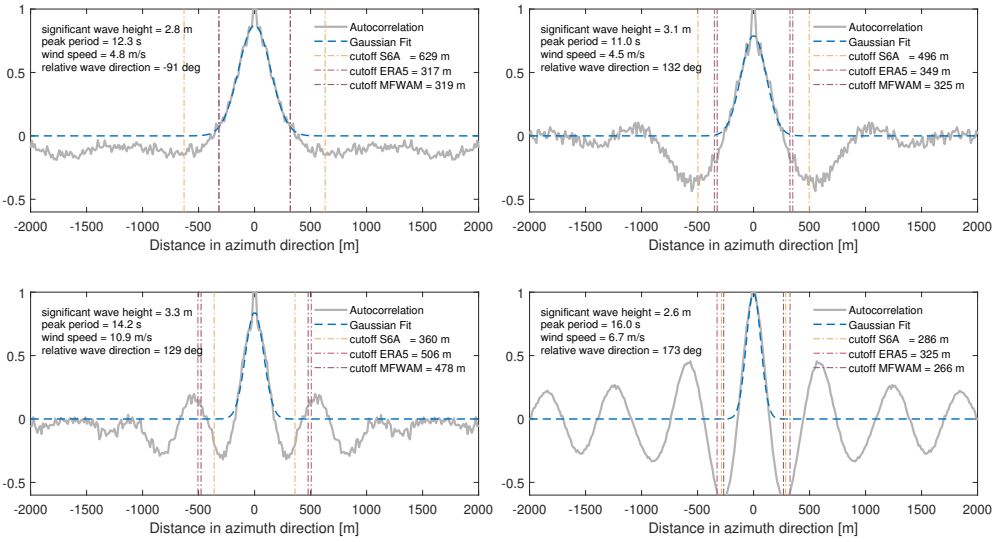

Figure 3.7: Examples of along-track autocorrelation functions, depicted in gray color, concerning SAR waveform-tail radargrams dominated by swells traveling in the cross-track direction (*top-left*), at angle (*top-right* and *bottom-left*) and in the along-track direction (*bottom-right*). The blue dashed line represents the Gaussian function. The yellow, pink, and brown dash-dotted lines represent the Sentinel-6A, ERA5 and MFWAM azimuth cutoff estimates, respectively. Sea-state conditions are obtained from ERA5 products.

The swell sensitivity has also been addressed in an analogous study that analyzed SAR images acquired by Envisat [27]. Note that side-looking SAR systems have a different geometry. The autocorrelation of nadir-looking altimeters is likely more sensitive to swell than side-looking SAR systems. A large fraction of the long-wave variability in backscatter, that causes the cutoff to be visible in the autocorrelation, originates from near-cross-track moving wind waves. The limited cross-track resolution of nadir-looking altimeters filters these short wind waves, while the signals of swell are stronger than those in side-looking SAR system due to the enhanced range bunching. Nevertheless, waves traveling closer to the cross-track direction were reported to cause larger discrepancies compared to those traveling closer to the along-track direction, an observation in line with our findings (refer to Figure 3.7 and bottom panels of Figure 3.6). In the same study, the authors tried to correct the overall errors by applying empirical corrections to the estimates, taking into account parameters such as wind speed, normalized variance, and sigma naught (i.e., backscattering coefficient). Biases could largely be removed with this parametrization,

but the precision remained rather poor. In the presence of swell, the shape of the autocorrelation is contaminated and in most cases not suitable for cutoff estimation through Gaussian fitting. Therefore, we make a first attempt to estimate the azimuth cutoff from the wavenumber domain.

3.4 Azimuth Cutoff Analysis in the Wavenumber Domain

In the wavenumber domain, the azimuth cutoff λ_f is associated with a fall-off wavenumber $k_{y_f} = \frac{2\pi}{\lambda_f}$, a parameter we aim to extract from the one-dimensional spectrum computed from the along-track autocorrelation, which will be referred to as spectral autocorrelation function. Figure 3.8 illustrates an example of how we estimate the fall-off wavenumber. The method constructs as follows. The spectral autocorrelation, shown in gray color, is computed by applying a Discrete Fourier Transform to the along-track autocorrelation function. The fall-off wavenumber, illustrated by the yellow circular marker, is approximated by identifying the intersection point between a model fitted to the spectral autocorrelation function and a threshold, that empirically is defined to be five times the median spectral along-track autocorrelation function. This threshold appears to effectively identify the point where the signal's background noise starts (around $|k_y| = 0.02$ rad/m in Figure 3.8), providing a first-order approximation of the fall-off width [105].

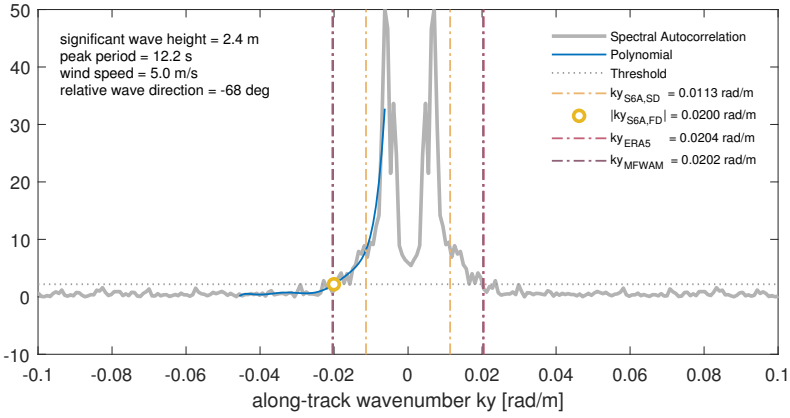

Figure 3.8: Example of the spectral autocorrelation function (gray solid line). The yellow circular marker represents the fall-off wavenumber identified as the intersection point between the gray dotted line, depicting the threshold line equal to five times the median spectral along-track autocorrelation function, and the blue solid line representing the seventh-order polynomial model. The pink and brown dash-dotted lines represent the fall-off wavenumber estimates from ERA5 and MFWAM, respectively. The yellow dash-dotted represents the Sentinel-6A fall-off wavenumber obtained from the spatial domain-derived azimuth cutoff estimate. Sea-state conditions are obtained from ERA5 products.

Table 3.3: Root mean square errors (RMSE) of the azimuth cutoff differences between Sentinel-6A (S6A) and wave model-derived values, calculated for varying numbers of samples considered in the spectral autocorrelation fitting.

Azimuth Cutoff Differences [m]	**RMSE**		
	20	50	100
S6A-ERA5	102.15	93.32	106.69
S6A-MFWAM	99.05	88.63	96.23

A seventh-order polynomial model is fitted to the decaying part of the spectral autocorrelation function. The spectral autocorrelation function exhibits oscillations, that initially reduced the fitting efficiency. To address this issue without altering its shape, a low-pass moving-average filter with a window size of 5 is applied as a pre-processing step. Lastly, we evaluate the fitting performance using 20, 50, and 100 samples, with sample 1 corresponding to the spectral peak. Table 3.3 presents the root mean square error (RMSE) of the azimuth cutoff differences between Sentinel-6A and wave models for all the examined scenarios, identifying the optimal case when 50 samples are used. Consequently, we continue the wavenumber domain analysis with this configuration.

Upon closer examination of the example presented in Figure 3.8, the sea-state conditions are characterized by a significant wave height of 2.4 m and a wind speed of 5.0 m/s. Swell waves with a peak period of 12.5 s are traveling at 68 degrees angle with respect to the satellite azimuth direction. The azimuth cutoff estimate in the wavenumber domain aligns well with the model-derived ones, exhibiting differences of 4 and 7 m with respect to MFWAM and ERA5, respectively. In contrast, the spatial domain analysis exhibits a notable deviation of 253 and 256 m from MFWAM and ERA5 estimates, respectively, which is primarily attributed to the presence of swells, as discussed earlier. To further investigate the applicability of this method in various sea states we conduct a sensitivity analysis, similar to the spatial domain case.

Table 3.4 provides statistics of the differences between wave model and Sentinel-6A derived azimuth cutoff estimates. Azimuth cutoff estimates below 50 m are treated as outliers and excluded, similar to the spatial domain analysis. It is worth noting that this exclusion constitutes about 2% of the total dataset, hence, we do not foresee any notable impact on our comparisons between the methods. Examining the results obtained considering the entire dataset, the azimuth cutoff correlation between satellite and wave models increases by 10%, reaching 0.8 compared to the 0.7 calculated in the spatial domain analysis, revealing a strong positive linear relationship between the variables. The standard deviation dropped to approximately 80 m, indicating a smaller dispersion of the satellite estimates compared to the model-derived ones. Examining the sensitivity of the method on different sea states, we observe that the correlations are higher for low-to-moderate winds, while the estimates agree significantly better for both low, moderate and high significant wave height scenarios. In cases of extreme wind seas, exceeding 15 m/s, the correlation is notably reduced. This observation could be attributed to a weaker linear relationship between the wave model and satellite-derived values obtained in the wavenumber domain.

Table 3.4: *Wavenumber domain analysis*: statistics of the azimuth cutoff differences and correlation coefficients between Sentinel-6A and wave models based on a sensitivity analysis of the former to changes in wind speed, significant wave weight and a combination thereof. The values outside and inside parentheses represent ERA5 and MFWAM results, respectively.

Category	Points	Mean [m]	Std. Dev. [m]	Corr. Coef.
All data	311,640 (311,594)	−41.68 (−38.53)	83.50 (79.98)	0.79 (0.81)
Wind speed [m/s]				
U10 < 5	66,918 (66,902)	−17.93 (−18.94)	58.16 (57.01)	0.68 (0.73)
5 < U10 < 15	232,486 (232,456)	−43.010 (−41.03)	84.24 (82.20)	0.71 (0.73)
U10 > 15	12,236 (12,236)	−146.30 (−98.16)	100.79 (104.69)	0.20 (0.26)
Significant Wave Height [m]				
Hs < 2	75,068 (73,463)	−21.9 (−9.87)	75.83 (71.60)	0.51 (0.52)
2 < Hs < 5	221,198 (216,403)	−40.26 (−38.98)	79.66 (76.09)	0.74 (0.76)
Hs > 5	15,374 (21,728)	−158.71 (−131.49)	79.38 (70.04)	0.58 (0.62)
Significant Wave Height [m] and Wind Speed [m/s]				
Hs < 2 and U10 < 5	34,721 (32,190)	−14.5 (−1.55)	61.11 (58.01)	0.47 (0.47)
2 < Hs < 5 and 5 < U10 < 15	185,075 (177,970)	−42.65 (−40.34)	82.21 (79.52)	0.68 (0.69)
Hs > 5 and U10 > 15	8139 (8050)	−180.21 (−139.01)	83.70 (81.39)	0.33 (0.30)

3.5 Discussion

Figures 3.9 and 3.10 present global maps of the azimuth cutoff and velocity variance parameters, respectively, with the top panels showing estimates from both models and the bottom panels displaying Sentinel-6A results in the spatial (bottom left) and wavenumber (bottom right) domains. The location of each value represents the midpoint of the fully-focused SAR waveform-tail radargram used to estimate the corresponding along-track autocorrelation function. Overall, the geographical patterns observed in the altimeter-derived maps align well with wave models. It appears that the altimeter can effectively capture wavelengths longer than approximately 100 m, with the highest values reaching 1000 m, corresponding to velocity variances exceeding 2.5 m^2 s^{-2}. Knowing that the velocity variance is primarily driven by wind waves, high values are expected in regions where wind seas are generated, such as the Southern Ocean and the North Atlantic. Comparing the level of agreement between the methods and the model-derived estimates, it becomes apparent that the wavenumber domain analysis demonstrates a better performance across the globe, compared to the spatial domain analysis. This applies also in the estimation of the low azimuth cutoff and velocity variance values, implying that the wavenumber domain method is less prone to errors in relatively calm sea-states. However, the opposite holds in the Southern Ocean, where extreme waves are developing. Specifically, the parameters estimated in the wavenumber domain are significantly underestimated compared to those in the spatial domain, which, although also underestimated, exhibit better agreement with wave models.

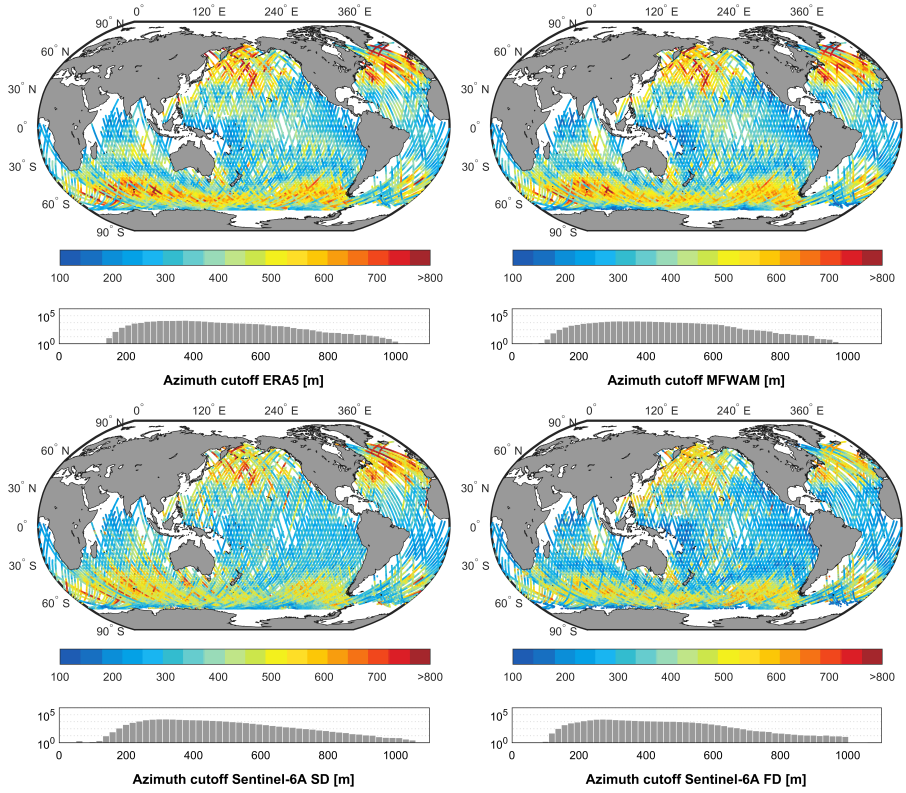

Figure 3.9: Global maps of the azimuth cutoff as derived by ERA5 (*top-left*), MFWAM (*top-right*), Sentinel-6A from the spatial domain (SD) analysis (*bottom-left*), and Sentinel-6A from the wavenumber domain (or Fourier Domain—FD) analysis (*bottom-right*). Each map is accompanied by a histogram showing the distribution of the estimates on a logarithmic scale.

To gain a better insight into the nature of the observed discrepancies with respect to sea-state conditions, Figure 3.11 presents global maps of wind speed and peak wave period from ERA5 in the top panels, while the velocity variance differences between Sentinel-6A and ERA5 and Sentinel-6A and MFWAM are illustrated in the middle and bottom panels, respectively. Note that, as the velocity variance is directly proportional to the azimuth cutoff, we anticipate same sensitivities in the estimation of the latter. Examining the underestimation patterns first, a strong relation with wind speed is observed. As discussed above, both methods tend to underestimate the velocity variance in wind seas, with the wavenumber domain analysis showing larger discrepancies. Here, it becomes evident that this trend increases gradually with rising wind speeds, particularly noticeable above 10 m/s. Note that decorrelation, for example, due to wave breaking, is ignored, leading to additional errors in extreme sea states.

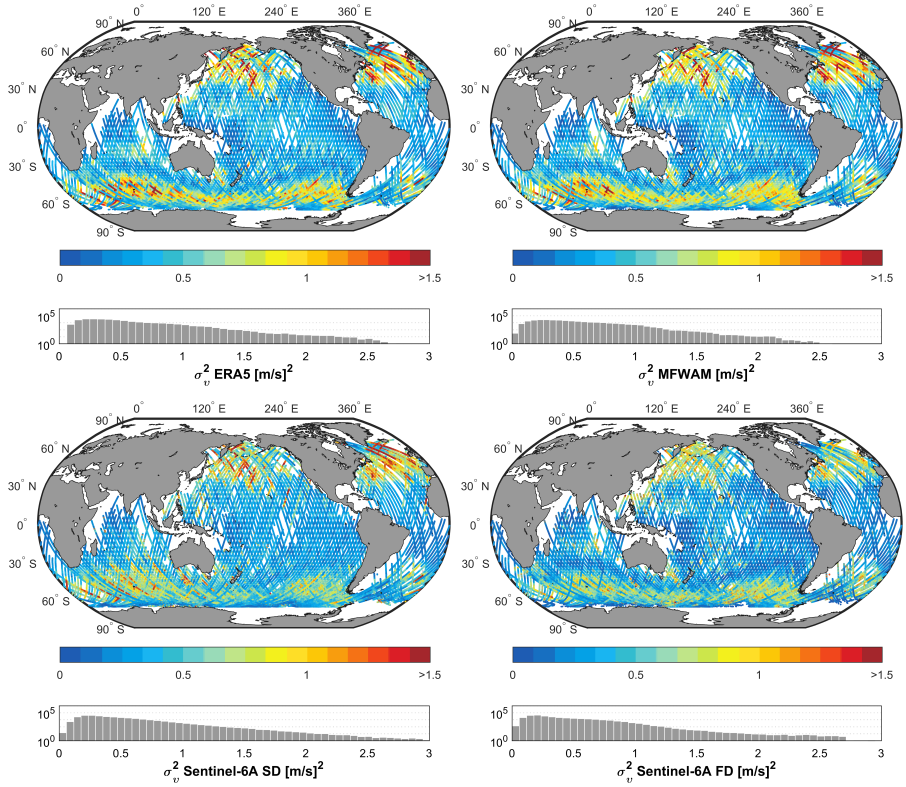

Figure 3.10: Global maps of the velocity variance as derived by ERA5 (*top-left*), MFWAM (*top-right*), Sentinel-6A from the spatial domain (SD) analysis (*bottom-left*), and Sentinel-6A from the wavenumber domain (or Fourier Domain—FD) analysis (*bottom-right*). Each map is accompanied by a histogram showing the distribution of the estimates on a logarithmic scale.

Moving to the overestimation patterns resulted from the analysis in the spatial domain (left middle and bottom panels) first, a significant amount of extremes becomes evident in regions where low wind seas (<5 m/s) and long-period waves (swells >14 s) coexist, such as west of Australia and in the central-east Pacific. As discussed in Section 4.3, the spatial domain method is sensitive to swells as long-wave oscillations alter the shape of the along-track autocorrelation function. This is effectively addressed when the radar signal is analyzed in the wavenumber domain, as shown in the right middle and bottom panels of Figure 3.11. The swell-induced errors are significantly mitigated, leading to a reduction in the overall overestimation errors, as depicted in the accompanying histograms of the differences. The remaining overestimation errors are dispersed and do not exhibit a clear dependency on wind and wave conditions. Instead, they are most likely associated with method sensitivities in accurately identifying the fall-off wavenumber by using a fixed signal's noise threshold for the entire spectrum of sea states. Since the fall-off wavenumber

method is introduced for the first time, additional research is required to enhance the accuracy of fall-off wavenumber estimation through the spectral autocorrelation function.

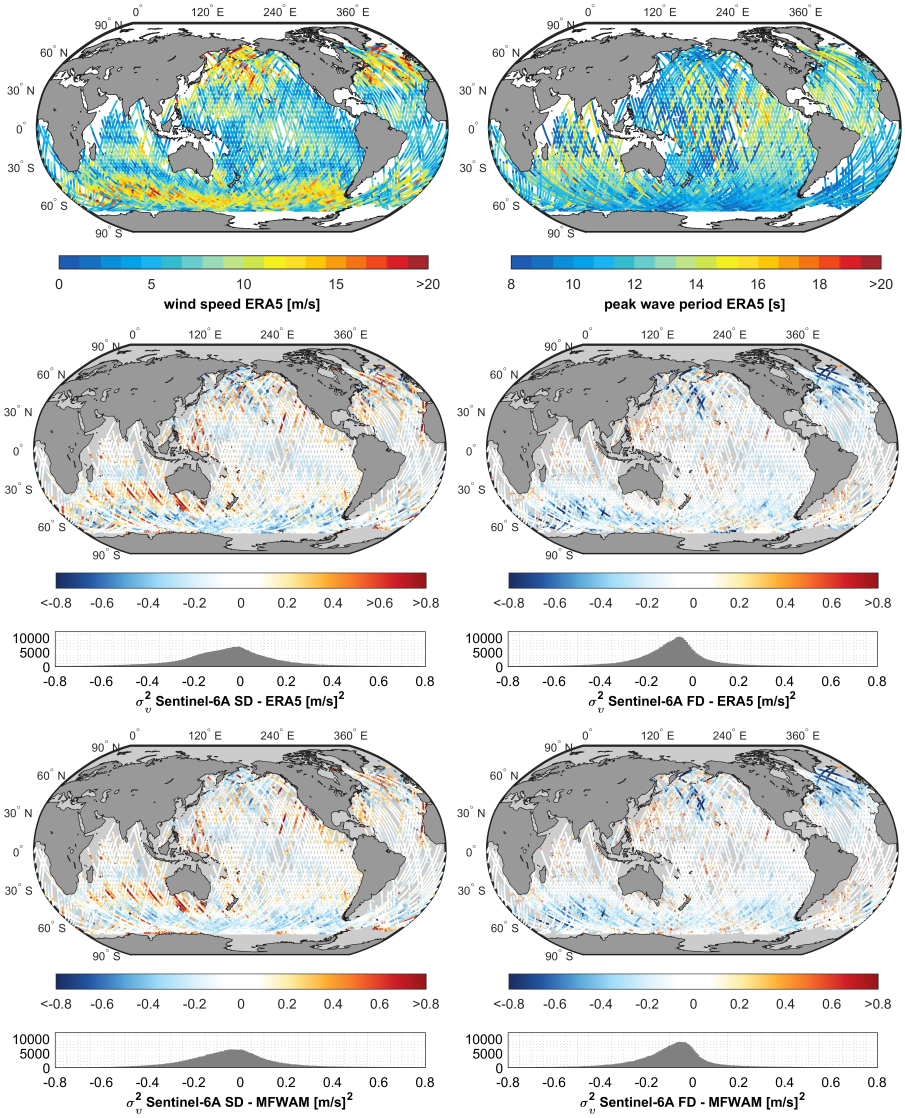

Figure 3.11: Global maps of the wind speed and peak wave period as obtained from ERA5 (*top panels*) and the velocity variance differences between ERA5 and Sentinel-6A in the spatial domain (SD) (*mid-left*) and wavenumber domain (or Fourier Domain—FD) (*mid-right*), MFWAM and Sentinel-6A in the spatial (*bottom-left*) and wavenumber (*bottom-right*) domains. Histograms of velocity variance differences accompany the middle and bottom panels.

Overall, the root mean square error of the velocity variance varies slightly between 0.22 and 0.26 $m^2\ s^{-2}$ across the four examined scenarios, with the smaller error calculated for the comparison between MFWAM and wavenumber domain derived values. It is important to acknowledge that, apart from the errors induced by the methods' limitations, inaccuracies in the wave models are also expected to contribute to the root mean square error. For instance, MFWAM and ERA5 use different modeling strategies to account for the dissipation caused by white capping. The challenge to properly modeling this oceanic process introduces biases to the wave parameters, particularly noticeable in the Southern Hemisphere under high wind conditions [106]. Focusing on this region in Figure 3.11, differences between ERA5 and MFWAM compared to the satellite-derived data are evident, with MFWAM displaying a more consistent behavior with respect to the satellite. Additionally, unlike MFWAM, ERA5 does not incorporate current data, potentially introducing inaccuracies in significant wave height estimates in areas influenced by strong currents. Current-induced refraction can significantly modulate wave properties, occasionally resulting in extreme wave heights [107]. Lastly, the development of swells introduces complexity to the evolution of wave heights, resulting in a more gradual change as they travel towards the tropics (<30 °N/S) [27]. Potential inadequacies in modeling this process could introduce additional errors into our comparisons. Therefore, it is recommended to undertake further efforts to carefully determine the source of errors, including the validation of both methods against in situ data, such as buoys. Moreover, considering that the extraction of wave orbital velocity information is feasible using an unfocused SAR processing technique [86], a comparative analysis could offer insights into the strengths and limitations of each approach. Leveraging their distinct processing characteristics could enhance our understanding of SAR responses to ocean dynamics.

3.6 Conclusions and Recommendations

This study explored the imaging capabilities of Synthetic Aperture Radar (SAR) altimeters in extracting wave orbital velocity information through the estimation of the azimuth cutoff. The azimuth cutoff, a well-established measure for side-looking SAR systems, serves as a proxy for the shortest detectable waves, in terms of wavelength, and is strongly related to the variance of the wave orbital velocity. By extracting this parameter, we aim to provide an additional measure to characterize sea-state dynamics from altimetry.

Initially, the azimuth cutoff was estimated by minimizing the residuals between the along-track autocorrelation function of a fully-focused SAR waveform-tail radargram and a Gaussian function fitted to it. To assess the method's performance across various sea states, a global-scale analysis was conducted using Sentinel-6A data from one repeat cycle, spanning from 11–21 December 2022. Level-1b fully-focused SAR multilooked waveforms were obtained using the Omega–Kappa focusing algorithm implemented in an updated version of the Standalone Multimission Altimetry Processor. The results were compared against two wave models, the ERA5 and MFWAM, for evaluation purposes.

Overall, the spatial domain analysis indicated that the altimeter can effectively capture waves longer than approximately 100 m. The algorithm performs reasonably well for moderate wind and wave conditions, while underestimation trends appeared to gradually increase with increasing wind speed and significant wave height. This observation is most likely to be attributed to the fact that a nadir-looking altimeter tends to capture only a fraction of the total distribution of vertical wave particle velocities, leading to its underestimation when velocity-slope dependencies are omitted [86], as is the case in our method. Moreover, profound impact of swells led to an abnormal overestimation of the azimuth cutoff in relatively calm wind seas. It was shown that the shape of the autocorrelation is significantly affected by swells. The magnitude of these errors was found to depend also on the wave propagation angle with respect to the satellite. Waves traveling closer to the cross-track direction appeared to cause larger discrepancies compared to those traveling closer to the along-track direction (refer to Figures 3.6 and 3.7). Overall, our findings are in line with azimuth cutoff studies conducted for SAR side-looking systems, such as [27].

Considering that swell related errors stem from the shape of the along-track autocorrelation function in the spatial domain, we made a first attempt to mitigate them by implementing an alternative method, conducted in the wavenumber domain. We approximated the fall-off wavenumber k_{y_f} by first fitting a polynomial model of seventh order in the decaying part of the spectral autocorrelation function and then identifying its fall-off width based on an empirically defined threshold, equal to five times the median spectral autocorrelation function. The azimuth cutoff λ_f was then estimated as $\lambda_f = \frac{2\pi}{k_{y_f}}$. Evaluating our method against both wave models again, we achieved to significantly mitigate the swell errors, improving the standard deviation of the differences between altimeter and model-derived azimuth cutoff estimates, from approximately 100 to 80 m. Overall, the wavenumber domain results are by 10% better linearly correlated with wave models (from approximately 0.70 to 0.80 for both models). However, the analysis of the radar signal in the wavenumber domain showed a more pronounced underestimation in wind-

dominated seas compared to the spatial domain analysis. The velocity variance root mean square errors were found to vary between 0.22 and 0.26 m^2 s^{-2} across the four examined scenarios, with the smaller error calculated for the comparison between MFWAM and Sentinel-6A wavenumber domain derived values. Further validation of both methods using in situ data is recommended as wave model inaccuracies are expected to contribute to the overall error.

Moreover, an essential consideration when applying the azimuth cutoff autocorrelation method to other SAR altimeters is that CryoSat-2 and Sentinel-3A/B operate in closed-burst mode, unlike Sentinel-6A which operates in open-burst mode [108]. The former's radar signal transmission-reception configuration was found to introduce ambiguities in the azimuth direction, visible as spatial aliases approximately every 90 m [109]. While these aliases are anticipated to impact the shape of the along-track autocorrelation function, the extent of this effect requires in-depth investigation, a topic beyond the scope of this study.

Lastly, the authors would like to emphasize that imaging ocean waves from SAR altimeters has undoubtedly opened up new applications. Leveraging the combined insights derived from the leading edge analysis (significant wave height and wind speed) and the trailing edge analysis (SAR directional spectra, azimuth cutoff and wave orbital velocity statistics) we anticipate that we will be able for the first time to separate wind and swell wave components in satellite altimetry.

4

Influence of Ocean Currents on Wave Modeling and Satellite Observations: Insights from the One Ocean Expedition

This study leverages in situ wave and positioning measurements collected during the One Ocean Expedition 2023 in the Indian Ocean to evaluate the performance of wave models and satellite observations within the highly dynamic environment of the Agulhas Current. In January 2023, six OpenMetBuoy drifters were deployed in the Agulhas Current region. Their high immersion ratio minimized wind effects, allowing them to follow the current and return to the Indian Ocean by the Agulhas retroflection, collecting data for about two months. Comparing surface current velocities from both the Mercator model and Globcurrent product with drifter data reveals underestimation for velocities over $0.5\,\mathrm{m\,s^{-1}}$*, with Mercator showing greater variability. Significant wave height and Stokes drift parameters from MFWAM and ERA5 were also evaluated against drifters. Both models tend to overestimate Stokes drift, more noticeable in ERA5, indicating sensitivity to wind seas. For significant wave height, both models agree well with drifter measurements, with correlations of 0.90 for MFWAM and 0.83 for ERA5. However, ERA5's lack of surface current data combined with its coarse resolution (0.5°) lead to underestimation of wave heights exceeding 2.5 m. MFWAM products including and excluding currents exhibit root mean square errors of 0.39 and 0.45 m, respectively, when compared to drifter measurements. This confirms that neglecting currents introduces additional errors, particularly in areas with sharp current gradients. Analyzing MFWAM wave spectra, including and excluding currents, reveals wave energy transfer attributed to wave-current interactions. The spatial extent of these interactions is captured by satellite altimeters, revealing wave modulations, with considerable wave height variations when waves cross eddies and the current core. The analysis is extended by evaluating the retrieval of swell parameters derived from various remote sensing technologies, including SAR altimeters (Sentinel-3B, Sentinel-6A), SAR imagery (Sentinel-1A) and wave spectrometry (CFOSAT), against drifter data. Comparisons demonstrated good agreement while also revealing the cross-track imaging limitations of altimeters.*

4.1 Introduction

Understanding the complex interactions between ocean waves and currents is essential for accurate wave forecasts as they significantly affect wave dynamics and energy distribution. Ocean currents, influenced by factors such as wind variations, temperature and salinity gradients, possess the ability to alter wave characteristics, including their amplitude and direction. This phenomenon, known as refraction, instigates energy transfer between currents and waves [110], often leading to the steepening of waves and the emergence of abnormal sea states characterized by extreme wave heights [111, 32, 30]. Such conditions can pose significant hazards to maritime activities and are critical for search and rescue operations, emphasizing the need for high-quality wave forecasts in current dominated regions to ensure safety. Additionally, surface currents affect air-sea interactions, including the fluxes of heat, carbon dioxide and momentum. They also impact coastal ecosystems, making it essential to monitor their strength and variability to understand environmental changes and ensure accurate climate predictions.

In recent decades, satellite remote sensing instruments have radically changed the study of ocean waves and currents on a global scale. Satellite altimetry allows the estimation of detailed maps of geostrophic currents [29], while offering consistent measurements of significant wave height and stress-equivalent wind speed globally [10, 3]. Synthetic Aperture Radar (SAR) altimetry has shown promise in retrieving swell wave spectra [84, 96], while satellites like Sentinel-1 and CFOSAT contribute significantly to global wave spectra products [16, 112]. Studies leveraging these advances have provided insights into how surface currents deflect incoming swell waves, resulting in phenomena such as wave trapping [113, 114, 115, 116, 117]. Despite these advances, accurately quantifying wave-current interaction effects at regional scales requires high-resolution and multi-spectral observations. However, challenges, such as data continuity, spatial resolution and coverage limitations, persist.

Wave models are essential for short-term forecasting (5-10 days) but often fail to capture the complex interplay between waves and currents, particularly when high-quality current data are lacking or currents are entirely neglected. Notably, neglecting currents in the simulations significantly affects wave height predictions, highlighting the need for surface current forcing to prevent major discrepancies, especially in regions prone to developing extreme waves [32]. Once current forcing is considered, several factors contribute to the complexity of accurately modeling its impact on waves. Some of them are related to the complex ocean dynamics in coastal zones, where bathymetry, coastline geometry, wave breaking and tidal variations complicate wave-current interactions [118]. These factors significantly influence the evolution of the wave field, intensifying the nonlinear interactions between waves and currents [119]. Moreover, the spatial and temporal resolution of wave models may fail to capture the rapid variability of currents [32], underlining the ongoing need to improve these models through data assimilation methods and validation activities against in situ measurements.

Undoubtedly, in situ measurements from moored buoys, drifters, and research vessels provide highly accurate data. However, collecting such measurements over large spatial scales is challenging due to high maintenance costs and maritime conditions. Conse-

quently, relying solely on these data limits our understanding of the broader impacts of currents on waves, which extend beyond local ocean processes. For instance, swell waves interacting with strong currents can undergo refraction kilometers away from their initial point of interaction, complicating the monitoring of their evolution [120].

The consideration of various data sources, including in situ measurements and satellite observations, enhances our ability to better understand complex dynamics of ocean circulation and achieve reliable predictions, thereby contributing to more accurate climate models and effective marine resource management. Our study exploits in situ measurements from drifters deployed during the ESA-PECO2 Advanced Ocean Training Course 2023, part of the One Ocean Expedition[1] 2021-2023, in the Agulhas Current region to evaluate the current impact on wave models and satellite observations. The Agulhas Current is considered one of the world's strongest western boundary currents, with surface velocities exceeding $3\,\mathrm{m\,s^{-1}}$ [31, 121]. This feature makes its study essential for understanding the climate system and marine biodiversity of the Indian Ocean. Moreover, its strength and dynamic mesoscale structures provide a unique natural laboratory for studying wave-current interactions.

The study is structured as follows. Section 4.2 details the methods and data acquisition process, including in situ measurements, satellites, and wave models. Section 4.3 presents comparative analyses of drifter-derived surface current speed, significant wave height and surface Stokes drift against wave models and satellite products. Initially, we examine surface current speeds as estimated by the drifters, the altimetry-derived Globcurrent[2] product and the Mercator[3] model. Subsequently, we perform a similar analysis on the impact of currents on significant wave height and Stokes drift products of the European Centre for Medium-Range Weather Forecasts Reanalysis v5 (ERA5) [63] and Copernicus Marine Environment Monitoring Service Météo-France WAve Model (MFWAM) [97, 98]. Section 4.4 extends this analysis by utilizing customized MFWAM wave spectra, computed both with and without current forcing, highlighting the importance of including surface current data in wave modeling. Section 4.5 focuses on the contribution of satellite altimetry in identifying wave-current interactions, emphasizing the critical role of multi-source data in understanding current-induced wave modulations. The wave spectra analysis is extended by exploiting the in situ wave measurements to evaluate the performance of various remote sensing technologies, including the Sentinel-3B and Sentinel-6A altimeters, Sentinel-1 SAR imagers and the CFOSAT wave spectrometer, on providing swells parameters. The study concludes in Section 4.6 with a summary of the key findings.

[1] https://oneoceanexpedition.com/
[2] https://doi.org/10.48670/mds-00327
[3] https://doi.org/10.48670/moi-00016

4.2 Data and Methods

4.2.1 OpenMetBuoy Drifters

During the One Ocean Expedition 2021-2023, six OpenMetBuoy drifters were deployed in the Agulhas Current region as part of the ESA-PECO2 Advanced Ocean Training Course 2023 held aboard the Statsraad Lehmkuhl sailing ship. The drifters, named OpenMetBuoy [122], have lateral dimensions of 16 x 16 cm and a height of 9 cm, with approximately 3 cm of overwater structure. Powered by alkaline batteries, these drifters had an operational period of approximately two months, which could be extended with higher-capacity batteries. Each drifter was equipped with an inertial measurement unit (IMU) with six degrees of freedom, enabling precise high-frequency measurements of acceleration and angular rates in the three spatial dimensions. Wave spectra, covering a frequency range between 0.040 and 0.307 Hz, were acquired at fixed intervals, with measurements taken for 20 minutes every three hours. Additionally, a GPS module was integrated for tracking the drifters' positions every 30 minutes. Over the two-month data collection period, the drifters' trajectories revealed distinct movement patterns. Figure 4.1 depicts these paths, plotted over mean surface current velocities obtained from the Copernicus Mercator product.

Four of the drifters were deployed within the core of the Agulhas Current, following the current towards the retroflection area and then towards the Indian Ocean. In particular, AC-01 and AC-02 were initially deployed together but drifted apart around the retroflection area. AC-05 and AC-06 were deployed approximately 12 hours apart with an initial separation of over 200 km, yet remained relatively close to each other until their power supplies were depleted. The remaining two drifters, ED-03 and ED-04, were deployed with a separation of about 30 km in the anticyclonic and cyclonic part of a vortex pair southeast of the Agulhas Current and quickly diverged from each other. Notably, both drifters exhibited inertial oscillations over periods of days, likely induced by sudden changes in local winds [123].

The observed patterns clearly show that the drifters closely followed the surface currents. Their small size and immersion-to-windage ratio minimized the impact of direct windage effects, which proved especially advantageous in the Agulhas Current, where surface drift is primarily driven by geostrophic currents [31]. As a result, we were able to infer the surface current directly from the drifter trajectories,

$$v_{\mathrm{dr}} \approx \frac{\Delta s}{\Delta t}. \tag{4.1}$$

Here, Δt represents a 30-minute time interval and Δs the distance traveled by a drifter during this period. An outlier removal scheme is implemented in two steps. First, outliers are rejected, setting a threshold for records taken at time intervals of less than 30 minutes. Secondly, records acquired with a time interval exceeding 3 hours were deemed to be of poor quality and subsequently excluded from the analysis. Then, considering linear wave theory, the significant wave height and the Stokes drift velocity are calculated from the

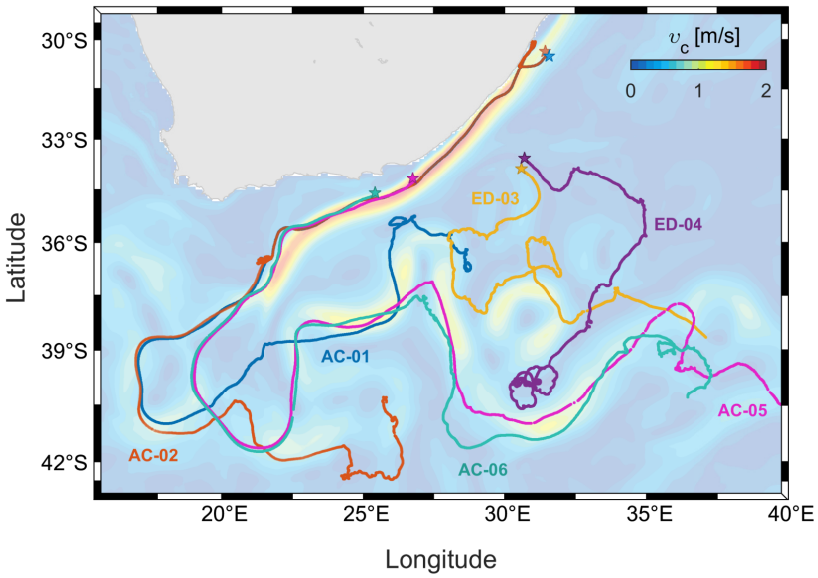

Figure 4.1: Mean Mercator surface current velocities (v_c is plotted in the background using inserted color scale) and drifters' trajectories from 05-Jan-2023 to 28-Feb-2023: Four drifters were deployed in the Agulhas core (AC) and two in the vicinity of eddies (ED). The star-shaped markers indicate the deployment locations.

ocean wave spectrum $F()$,

$$H_s = 4\sqrt{\int_0^\infty F(\omega)\,d\omega} \tag{4.2}$$

$$v_{\mathrm{st,dr}}(z) = \frac{2}{g}\int_0^{2\pi}\int_0^\infty \omega^3 \hat{\mathbf{k}} e^{2kz} F(\omega,\theta)\,d\omega\,d\theta. \tag{4.3}$$

Here θ denotes the direction in which the wave component is travelling, $\omega = 2\pi f$ is the circular frequency with f the linear frequency and $\hat{\mathbf{k}}$ the unit vector in the direction of wave propagation [124]. For the purpose of our study, depth, denoted by z, is set to zero as we are solely interested in surface Stokes drift velocities for our comparisons with the drifter-derived estimates. Given that OpenMetBuoys provide one-dimensional frequency wave spectra, thus lacking directional information, we simplify Eq. 4.3 to [125]

$$v_{\mathrm{st,dr}}(0) = \frac{2}{g}\int_0^\infty \omega^3 F(\omega)\,d\omega. \tag{4.4}$$

Table 4.1: List of the parameters and setup used as the forcing conditions for both satellite and wave model products.

	Mercator	**Globcurrent (NRT)**	**ERA5**	**MFWAM**
spatial resolution	1/12°	1/4°	1/2°	1/12°
temporal resolution	6h	1h	1h	3h
wind speed	N/A	Global Ocean	ERA5	IFS-ECMWF
bathymetry	ETOPO1	ETOPO1	ETOPO2	ETOPO2
current forcing	N/A	N/A	NO	(a) Mercator PSY4 (daily) (b) Globcurrent (daily) (c) NO

Copernicus Product ID:WIND_GLO_PHY_L4_NRT_012_004

4.2.2 Wave Models and Satellite Observations

Table 4.1 outlines the configuration characteristics of the wave and current products used in our study. The operational Copernicus Mercator global ocean analysis and forecast system [126] and the Copernicus ESA Globcurrent product [29] are considered for the surface current analysis. Mercator provides 6-hourly surface current data, whereas Globcurrent provides hourly estimates derived from a combination of Copernicus Marine Service near real-time satellite geostrophic surface currents and modeled Ekman drifts, utilizing European Centre for Medium-Range Weather Forecasts (ECMWF) near real-time wind speed data. Both products ignore the effects of Stokes drift. To maintain consistency with the surface speeds recorded by the drifters, we consider only surface currents by setting depth to zero. Mercator's gridded data are available at a resolution of 1/12°, whereas Globcurrent has a resolution that is three times coarser, 1/4°.

The surface Stokes drift and significant wave height are obtained from the MFWAM model [127, 97, 98], an operational global ocean analysis and forecast system, and the ERA5 product [63]. ERA5 combines historical observational data with advanced modeling techniques to produce reanalysis. This involves the assimilation of data from satellites, weather balloons, buoys and ground stations. Specifically, ERA5 assimilates observations from SARAL and CryoSat-2 based on its operational stream [63]. In contrast, MFWAM incorporates significant wave height observations from altimeters such as Jason-3, SARAL, CryoSat-2, Sentinel-3 A/B, CFOSAT, and Sentinel-6A, as well as ocean-wave spectra from Sentinel-1 [128]. In terms of resolution, MFWAM provides 3-hourly instantaneous estimates with a spatial resolution of 1/12°. In contrast, ERA5 provides hourly data, thus enhancing temporal resolution by a factor of 3 compared to MFWAM. However, ERA5's spatial resolution is six times coarser, at about 1/2°.

Notably, ERA5 does not incorporate surface current forcing, whereas MFWAM uses the operational Mercator forecast product. In particular, the standard MFWAM product is forced by surface currents from the global Mercator PSY4 ocean forecasting system, which provides daily updates. Given the differences in setup and forcing systems between ERA5

and MFWAM, direct comparisons for evaluating current impact on wave evolution could be misleading. To address this, we conduct two additional experiments: one with MFWAM forced by the Globcurrent product and another without surface current data. This setup allows us to investigate the impact of currents on wave height by comparing three different MFWAM runs: one with model-derived currents (Mercator), one with satellite-derived currents (Globcurrent), and one excluding current data, as shown in Table 4.1. Lastly, both the wave models and Globcurrent product are interpolated using the nearest neighbor technique to the drifters' locations accounting for the different sampling intervals of the GPS (30 minutes) and wave (3 hours) measurements.

4.3 A Comparative Analysis Along Drifters' Trajectories: Satellite Observations and Wave Models Against in Situ Measurements

4.3.1 Surface Current Velocity

Figure 4.2 presents maps of in situ-derived surface current speed along the drifter trajectories and those obtained by the Mercator and Globcurrent products. Compared to the drifters' measurements, both Mercator and Globcurrent appear to underestimate the surface current velocities within the core of the Agulhas Current and in areas beyond its retroflection, an observation previously reported for Globcurrent by Hart-Davis *et al.* [129]. The accompanying density plots, which include around 18,400 data points, show that this trend persists in both products when current speeds exceed approximately $0.5\,\mathrm{m\,s^{-1}}$.

Globcurrent aligns more closely with drifter data, exhibiting a linear correlation of 0.84 and an RMSE (Root Mean Square Error) of $0.32\,\mathrm{m\,s^{-1}}$. In contrast, Mercator displays a correlation of 0.51 and an RMSE of $0.52\,\mathrm{m\,s^{-1}}$. The decomposition of the RMSE into bias and standard deviation [130] reveals that bias has a negligible impact on the total error of the examined products (see Table A1, supporting material).

These discrepancies can be partially attributed to the spatial and temporal resolution limitations of the products, which may not capture small-scale dynamics effectively. The observed underestimation of surface currents by the Mercator model aligns with findings in Mercator's Quality Information Document [131]. This document indicates that when compared to in situ measurements from drifting buoys, the underestimation can range from 20% in strong currents to 60% in weak currents. Although the inclusion of Stokes drift, particularly during storms, may improve modeled surface velocities, its magnitude is expected to be relatively small in regions with strong currents, such as the Agulhas. This is because the current speeds in such areas are typically much higher than the Stokes drift, diminishing the latter's impact on the overall surface velocity. Globcurrent's performance, which partially depends on satellites' coverage and revisit period, may be constrained by its tendency to smooth small-scale dynamics affected by local wind variations and current variability [129].

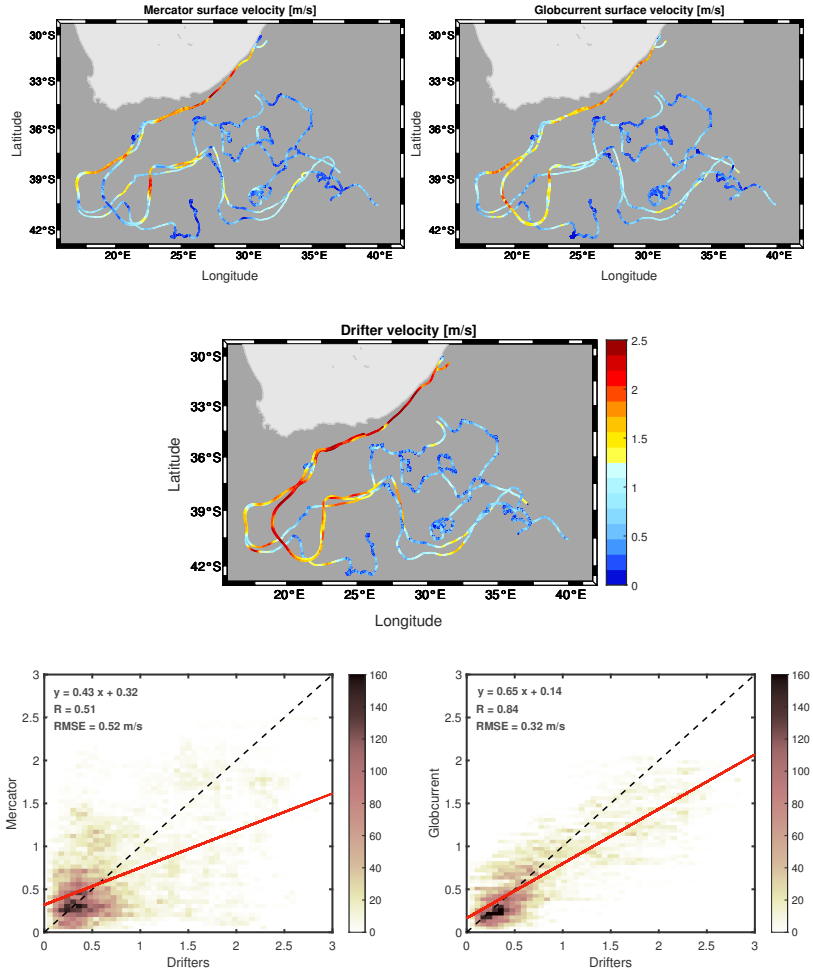

Figure 4.2: Surface current velocity interpolated along the six drifter trajectories from Mercator *(top-left)*, Globcurrent *(top-right)* and as measured by the drifters *(middle)*. Density plots of drifters' measurements versus Mercator *(bottom-left)* and Globcurrent *(bottom-right)*. A regression line is shown in red color. The dashed black line represents the line of equality when in situ = model [m s^{-1}].

Considering the variability in current strength in the study area, we analyze specific aspects for each drifter. Figure 4.3 presents scatter plots of surface speed for individual drifters, contrasting their measurements with those from the Mercator and Globcurrent products in the top and bottom panels, respectively. Notably, the four drifters deployed within the current core (AC-01, AC-02, AC-05, AC-06) show significantly better alignment with Globcurrent, exhibiting linear correlation coefficients ranging from 0.79 to 0.86, compared to Mercator's 0.32 to 0.60. In contrast, drifters located around eddies exhibit varying correlation patterns. Mercator shows very weak correlations, with coefficients of 0.10 and

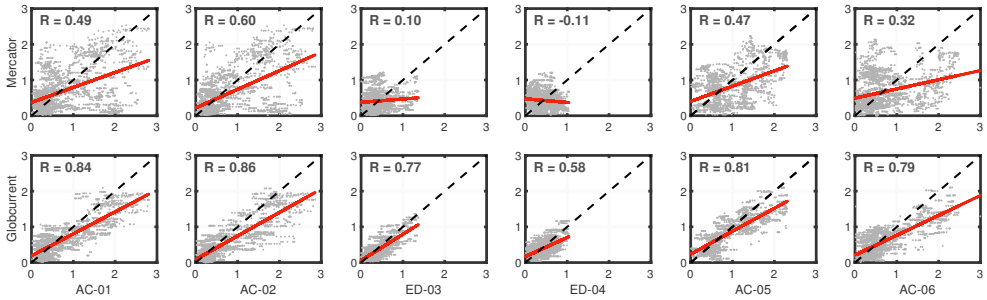

Figure 4.3: Scatter plots of drifter-derived surface current velocity versus Mercator *(top panels)* and Globcurrent *(bottom panels)* for each drifter separately. A regression line is shown in red color. The dashed black line represents the line of equality when in situ = model. Unit: $\mathrm{m\,s^{-1}}$

-0.11 for drifters ED-03 and ED-04, respectively, which are statistically well below the significance level. In contrast, Globcurrent maintains relatively good agreement, achieving moderate correlations of 0.58 and 0.77, respectively. As mentioned earlier, instances of near-surface inertial oscillations are revealed in Figure 4.1. These oscillations, driven by the Coriolis effect, lead to circular, counterclockwise trajectories in the southern hemisphere, and are particularly evident in the latter part of drifter ED-04's path.

4.3.2 Stokes Drift and Significant Wave Height

Although surface Stokes drift is expected to be significantly smaller than the geostrophic current in the Agulhas region, our primary focus is on evaluating the ERA5 and MFWAM operational products against in situ measurements. As shown in Figure 4.4, this analysis includes Stokes drifts derived from drifters, compared with ERA5 and MFWAM, along with their corresponding scatter plots. The analysis encompasses approximately 3,000 data points, which is notably fewer than those used in the surface current analysis. This is due to the less frequent sampling rate of wave spectra, which was set to 3 hours.

The drifters recorded surface Stokes drifts reaching up to approximately $0.3\,\mathrm{m\,s^{-1}}$, with both models consistently overestimating these values. Particularly ERA5 shows a pronounced tendency towards higher estimates. In evaluating model performance via correlation coefficients, both models demonstrated a reasonable alignment with drifter data: MFWAM achieved a correlation of 0.80, while ERA5 recorded a lower correlation of 0.72, albeit accompanied by notable variability. In terms of accuracy, assessed through RMSE, both models perform similarly, achieving 0.04 and $0.05\,\mathrm{m\,s^{-1}}$ for MFWAM and ERA5, with bias and standard deviation being comparable (see Table A1, supporting material).

Note, that as reported by Breivik *et al.* [125] and Ardhuin *et al.* [132], implementing an unidirectional approach may result in an overestimation of the Stokes drifts by approximately 15-19%, while in swell-dominated seas the impact is less. Therefore, this would lead to relatively larger discrepancies compared to wave models. However, given that the observed Stokes drifts do not exceed $0.3\,\mathrm{m\,s^{-1}}$, and considering that geostrophic forces,

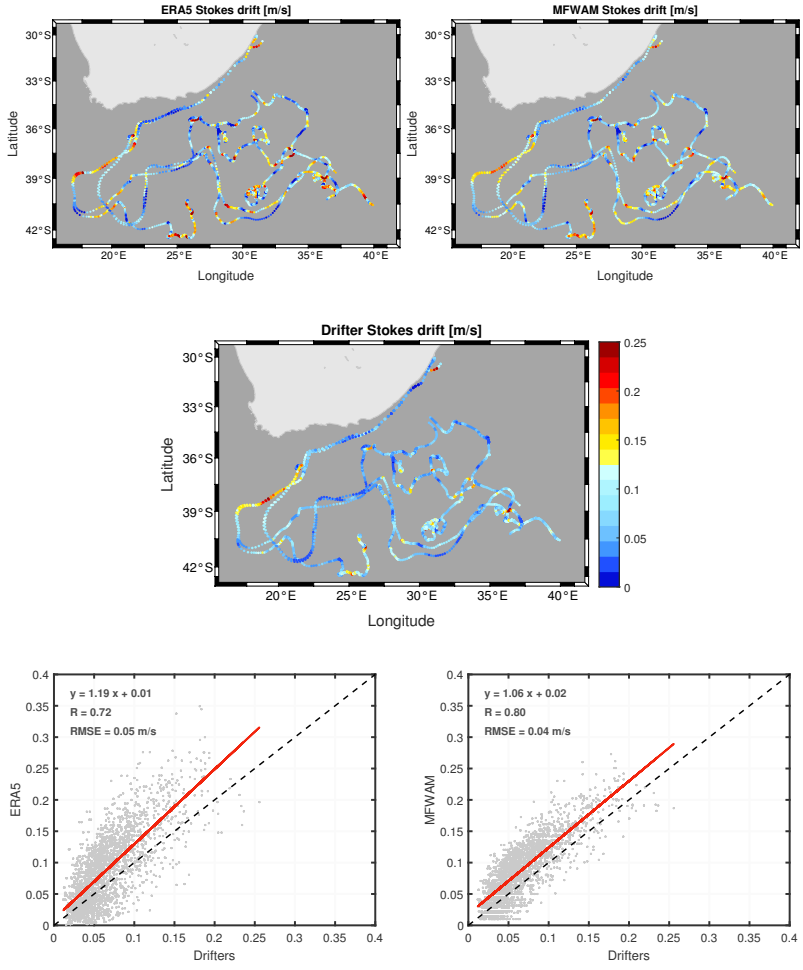

Figure 4.4: Surface Stokes drifts interpolated along the six drifter trajectories from ERA5 *(top-left)*, MFWAM *(top-right)* and as measured by the drifters *(middle)*. Scatter plots of drifters' measurements versus ERA5 *(bottom-left)* and MFWAM *(bottom-right)*. A regression line is shown in red color. The dashed black line represents the line of equality when in situ = model. Unit: $\mathrm{m\,s^{-1}}$

being predominant, can nearly be ten times stronger, the influence of our assumption is likely minimal. Thus, we deem this assumption to fall within the noise level of our measurements [133], rendering its impact negligible.

Various factors could contribute to the observed discrepancies, including differences in wave model setup and forcing parameters. For example, the relatively coarse spatial resolution of 1/2° in ERA5 might fail to capture small-scale dynamics influenced by local wind variations, aligning with the observed average Stokes drift direction [134]. An individual analysis of the drifters' trajectories indicates a comparable level of overestimation

across all data points, with linear correlations ranging from 0.69 to 0.85 for both models, with MFWAM achieving approximately 10% higher correlation. Detailed plots of these correlations can be found in the supporting material (see Figure A1).

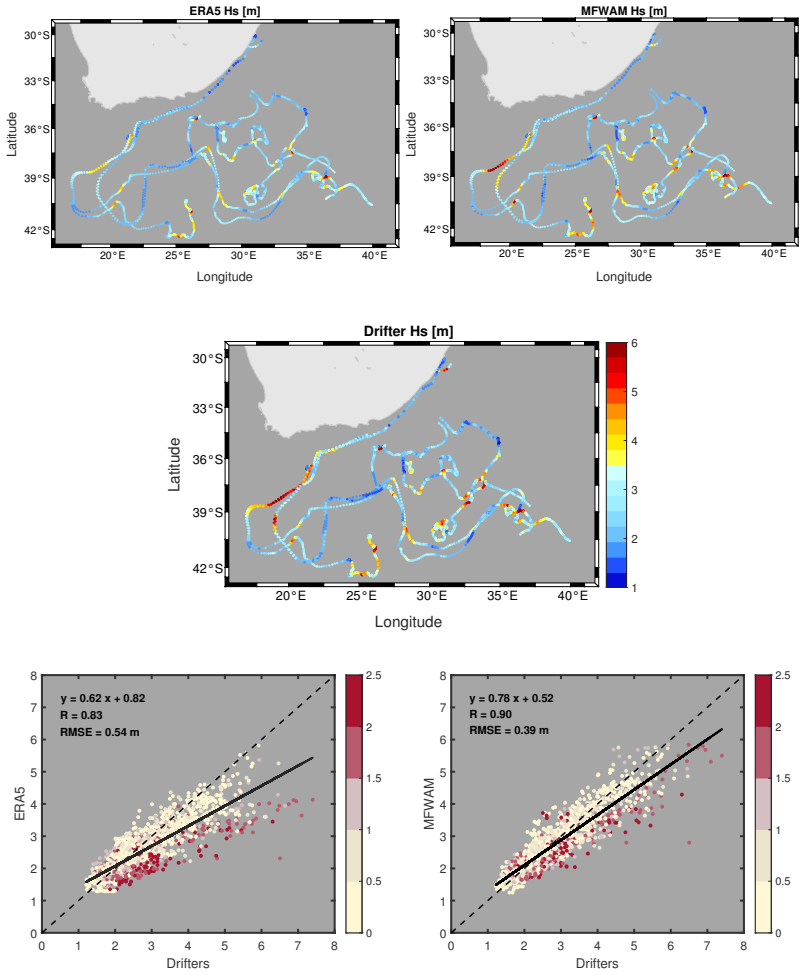

Figure 4.5: Significant wave height interpolated along the six drifter trajectories from ERA5 *(top-left)*, MFWAM *(top-right)* and as measured by the drifters *(middle)*. Scatter plots of drifters' significant wave height measurements versus ERA5 *(bottom-left)* and MFWAM *(bottom-right)*, colored to indicate the drifters' surface current speeds v_{dr} ($\mathrm{m\,s^{-1}}$). A regression line is shown in black color. The dashed black line represents the line of equality when in situ = model. Unit: m

Similar to the analysis of Stokes drifts, Figure 4.5 presents maps of significant wave height estimates as derived from both models against drifters. The maps suggest good correspondence for both models. In particular, correlations of 0.90 and 0.83 and RMSE

of the differences at 0.39 and 0.54 m are calculated between the drifters and MFWAM, and the drifters and ERA5, respectively. Notably, ERA5 exhibits larger discrepancies and a distinct trend of underestimation with increasing wave height, particularly for waves exceeding approximately 2.5 m. This trend can by described by a negative bias of 0.23 m for ERA5, compared to 0.04 m for MFWAM, while in terms of variability the standard deviation is estimated at 0.48 and 0.38 m, respectively (see Table A1, supporting material).

A considerable part of the underestimation in both MFWAM and ERA5 appears to be linked to the surface current strength, as indicated by the coloring of the scatter points based on drifter-measured current speeds. In particular, ERA5 does not incorporate surface current data into its simulations, overlooking the impact of currents on wave evolution. Specifically, ERA5's lack of accounting for wave refraction and steepening effects leads to larger discrepancies compared to MFWAM, with errors occasionally exceeding 2 m in extreme sea states. This observation underscores the critical role of incorporating current modeling within wave forecasting systems. An individual significant wave height analysis of the drifter trajectories reveals similar trends to Figure 4.5, with linear correlations ranging from 0.73 to 0.95 (see Figure A2, supporting material). MFWAM consistently outperforms ERA5, confirming the impact of current and eddies on wave height forecasts.

A comparison between significant wave height and Stokes drift results reveals contrasting trends: while significant wave heights are underestimated, Stokes drift shows a tendency to be overestimated with increasing sea states. In our study area, wave heights are primarily dominated by swells generated from distant storms. The underestimation of wave heights in high sea states suggests that wind speeds during these storm events may be underestimated, creating uncertainties in the initial wind-waves growth conditions and, consequently, affecting the transition to swell regime. In contrast, the overestimation of Stokes drift can be attributed to the use of a Phillips wave spectrum shape for the high-frequency part of the spectrum in both ERA5 and MFWAM, which tends to distribute excess energy in this range [135]. Additionally, the upper frequency cutoff for both models is significantly higher than that of the drifters (0.56 Hz for MFWAM and 0.55 Hz for ERA5, compared to 0.30 Hz for the drifters). Taking into account that Stokes drift estimates are sensitive to high-frequency components—magnified by the $\omega^3 = (2\pi f)^3$ factor (Eq. 4.4)—this suggests that noise will propagate into the final estimates, thereby amplifying inaccuracies.

Given the inherent complexities of absolute comparisons between different models, which are developed using varied wind, wave, and current forcing systems, along with different spatial and temporal resolutions as shown in Table 4.1, such comparisons can admittedly complicate interpretation of differences. While geostrophic currents dominate in the region, we must also acknowledge topographic steering and wind-driven small-scale ageostrophic components that are captured by the drifters but not necessarily by the models. Lastly, errors related to instrument performance and method implementation may also contribute to RMSE. Therefore, the next section discusses additional experiments, customizing MFWAM with different current forcing settings to assess the potential weaknesses and strengths inherent in each scenario.

4.4 Surface Current Impact on Wave Parameters and Ocean Wave Spectra

4.4.1 Significant Wave Height and Stokes drift

In this experiment, MFWAM is run with (a) the Mercator surface current product, (b) the Globcurrent surface current product, and (c) without currents. Figure 4.6 illustrates the fluctuations in significant wave heights along the path of each drifter per model from the date of deployment until February 28.

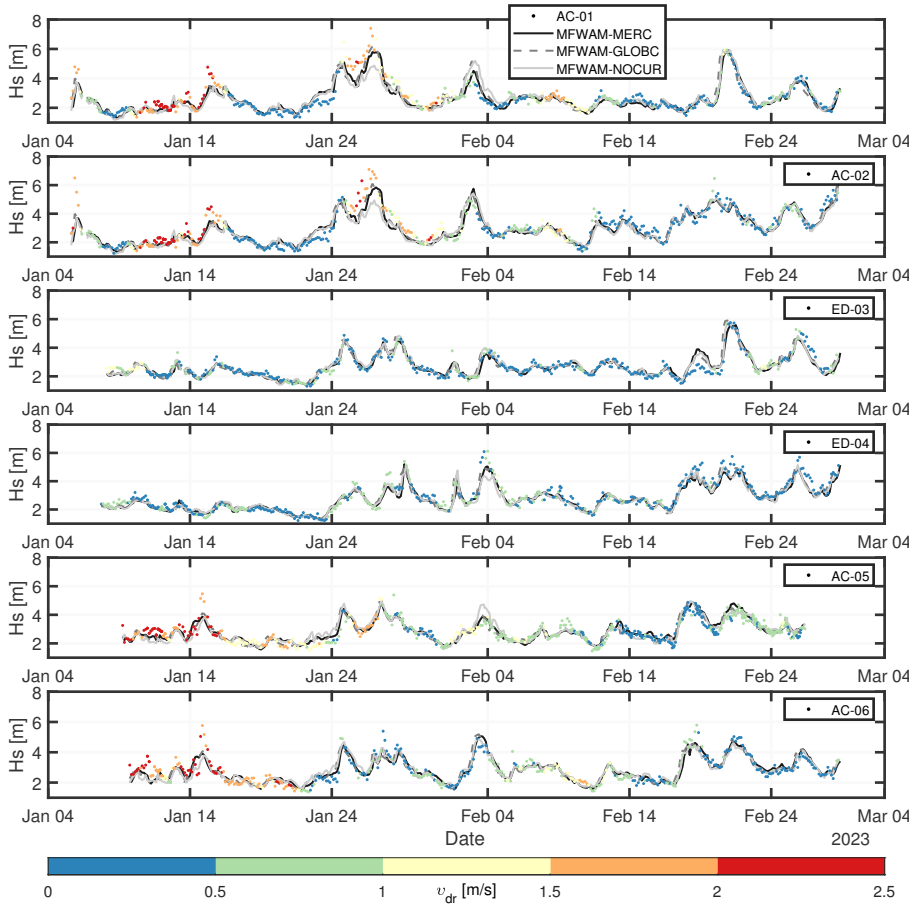

Figure 4.6: Time series of significant wave height derived from each drifter and the MFWAM products. The wave heights measured by the drifters are shown as dots, colored to indicate the corresponding surface current speeds (v_{dr}).

Overall, in relatively calm current conditions ($< 0.5\,\mathrm{m\,s^{-1}}$) and up to moderate significant wave height ($< 3\,\mathrm{m}$), the model runs align closely with in situ measurements. However, under higher wave conditions—particularly when wave heights exceed 4 m, likely indicating storm events—the models begin to diverge with increasing current speed. For instance, drifter AC-01 recorded two significant wave height peaks of around 6 m at the end of January and February, while experiencing current speeds above $1.5\,\mathrm{m\,s^{-1}}$ and below $1.0\,\mathrm{m\,s^{-1}}$, respectively. Notably, the first peak was also recorded by drifter AC-02. These instances indicate a pronounced underestimation of wave height associated with increased drifter speeds. This suggests that higher current speeds likely introduce significant uncertainties in wave forecasts when currents are not considered, with discrepancies sometimes exceeding 2 m in high sea states, as also shown in the analysis of ERA5 data (Figure 4.5) and further illustrated in Figure A3 of the supporting material. Conversely, the MFWAM run excluding current data can lead to an overestimation of wave height, as observed for AC-05 on February 3. This can be attributed to the alignment between wave and currents in this case, with a mean wave direction of 232° relative to North according to MFWAM and a current flow direction of 223° based on Globcurrent. When waves and currents propagate in the same direction the momentum flux to the waves is reduced, and, consequently, the exclusion of current in modeling can result in an overestimation of wave heights [32]. The impact of not including current data in the simulations is also evident in the RMSE, which increases to 0.45 m compared to 0.39 m when Mercator and Globcurrent current data are integrated into the model (see Table A1, supporting material). This result also suggests that both Mercator and Globcurrent perform equally well compared to drifters when current dynamics are considered.

Continuing our analysis of Stokes drifts, Figure 4.7 compares in situ measurements with the customized MFWAM results. Although all model runs generally capture the overall in situ trends, a systematic overestimation is evident across the models. A comparison between MFWAM-Mercator, MFWAM-Globcurrent and MFWAM-no-current runs reveals that current forcing has only a marginal impact, as Stokes drift is primarily driven by local winds. This suggests that the inclusion of current data does not significantly impact the overall accuracy of Stokes drift predictions. Overall, the discrepancies observed across the model experiments seem to be within the noise level, with the RMSE calculated to be about 10% of the mean modeled Stokes drifts, suggesting a relatively minor but still noticeable variance (see Table A1, supporting material).

As previously mentioned, Globcurrent is produced by combining geostrophic velocities, derived from altimeters, with modeled Ekman drifts, while neglecting the impact of Stokes drift. Given that Stokes drift reaches up to approximately $0.3\,\mathrm{m\,s^{-1}}$ according to our analysis, its contribution to the overall surface velocity is expected to be small. However, in scenarios with weaker currents, incorporating Stokes drift could potentially improve the agreement between satellite observations and in situ measurements.

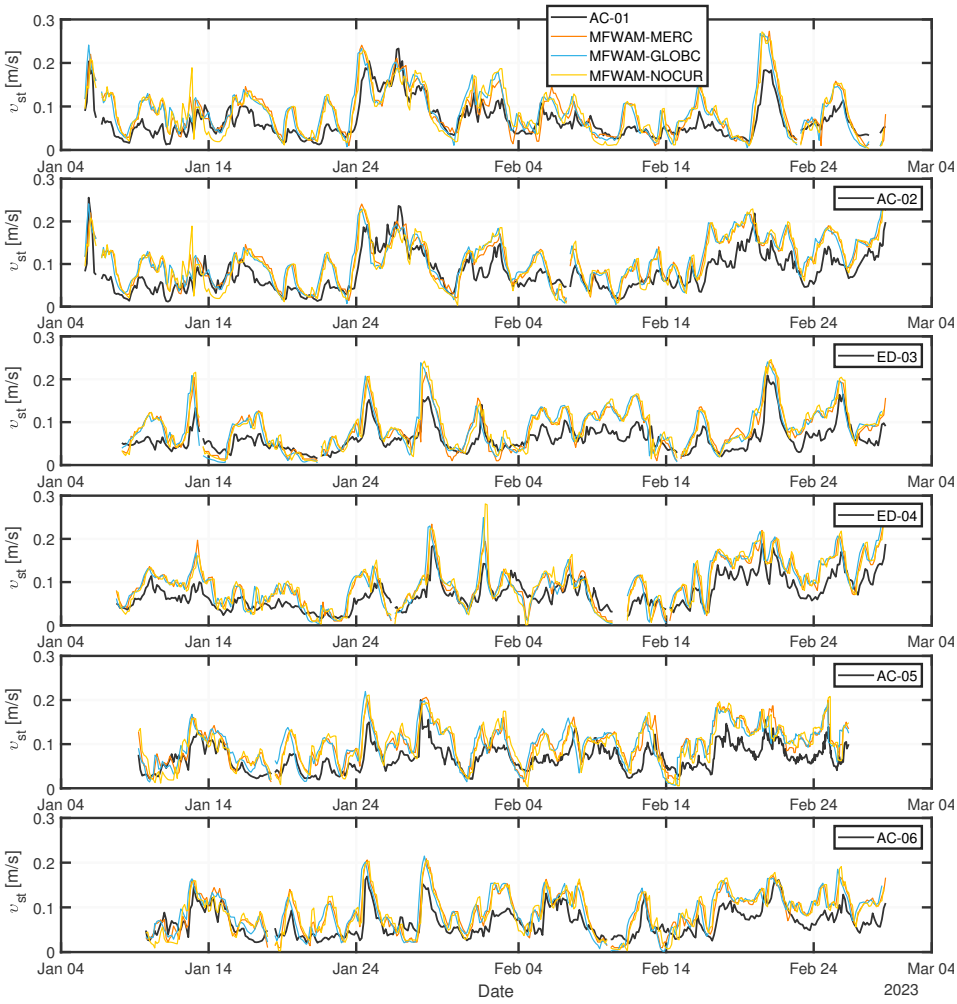

Figure 4.7: Time series of Stokes drift (v_{st}) derived from each drifter and customized MFWAM runs indicated by the different colors.

4.4.2 Ocean wave spectra

Taking into account the influence of currents on the wave field and the resulting energy transfer, we will now investigate the wave spectra computed by all three model experiments and drifters to highlight their impact. We focus on three areas for detailed examination, and, for simplicity, we concentrate on data from a single drifter, namely AC-01. As shown in Figure 4.1, this drifter followed the Agulhas current core, experiencing a wide range of current speeds, allowing us to evaluate the impact of varying current conditions. Averaged Mercator and Globcurrent surface velocities over the experiment period are shown in the top-left and top-right maps of Figure 4.8, respectively. The examined

zones are around the core of the Agulhas Current (zone A) and its retroflection (zones B and C). All cases represent collocations within 1 hour and 20 km distance between gridded MFWAM points and drifter locations to minimize the impact of local wind-wave condition differences. The unidirectional wave spectra from both drifters and MFWAM runs (panels a-c) as well as the MFWAM directional (panels d-l) wave spectra reveal distinct patterns and variations.

In zone A, with current speeds reaching about $2.4\,\mathrm{m\,s^{-1}}$, swells travel northeast at 41.7°, while long-period wind waves come from the opposite direction at 192.8°. The one-dimensional wave spectra provided by model runs with Globcurrent and Mercator closely match the drifter's significant wave height estimates, with discrepancies of 2 and 32 cm, respectively (panel a). Ignoring current refraction results in a more peaky wave spectrum for both swell and wind waves and an overestimation of the significant wave height by 73 cm. The impact of currents on waves is also captured in the MFWAM directional spread where wave energy is spread across frequencies and directions due to refraction (panels d, g vs j). Notably, wave energy decreases when current refraction is included, an observation that has also been reported in other studies [32, 136]. It is evident that when currents are accounted for, swells with a peak wave period of about 13 seconds are slightly shortened to 12 seconds under a current strength of $2.4\,\mathrm{m\,s^{-1}}$, without noticeable impact on their propagation direction.

In zone B, within the retroflection area, the current strength decreases to $1.6\,\mathrm{m\,s^{-1}}$. Swells dominate, traveling northeast at 51.6°, while wind waves are much weaker, traveling east-west at 89.9°. The drifter records a significant wave height for the swell at 7.4 m, with its one-dimensional wave spectrum featuring a high-energy swell peak nearly four times larger than those reported by all model runs, indicating a considerable underestimation of the significant wave height (panel b). Specifically, Mercator and Globcurrent underestimate the wave height by 1.9 and 1.4 m, respectively. Without current data, the underestimation reaches 2.6 m, a critical magnitude for accurate wave forecasting and marine safety. Overall, the observed wave height variability underscores the challenges of modeling dynamic marine environments and the need for ongoing refinement of model parameters, especially in extreme wave conditions. In contrast to zone A, the directional wave spectra show minor signs of wave energy spread, indicating that swells of the same order of magnitude, i.e., 13 seconds, can maintain their wavelength and propagation direction when current speeds reach $1.6\,\mathrm{m\,s^{-1}}$ (panels e, h vs k).

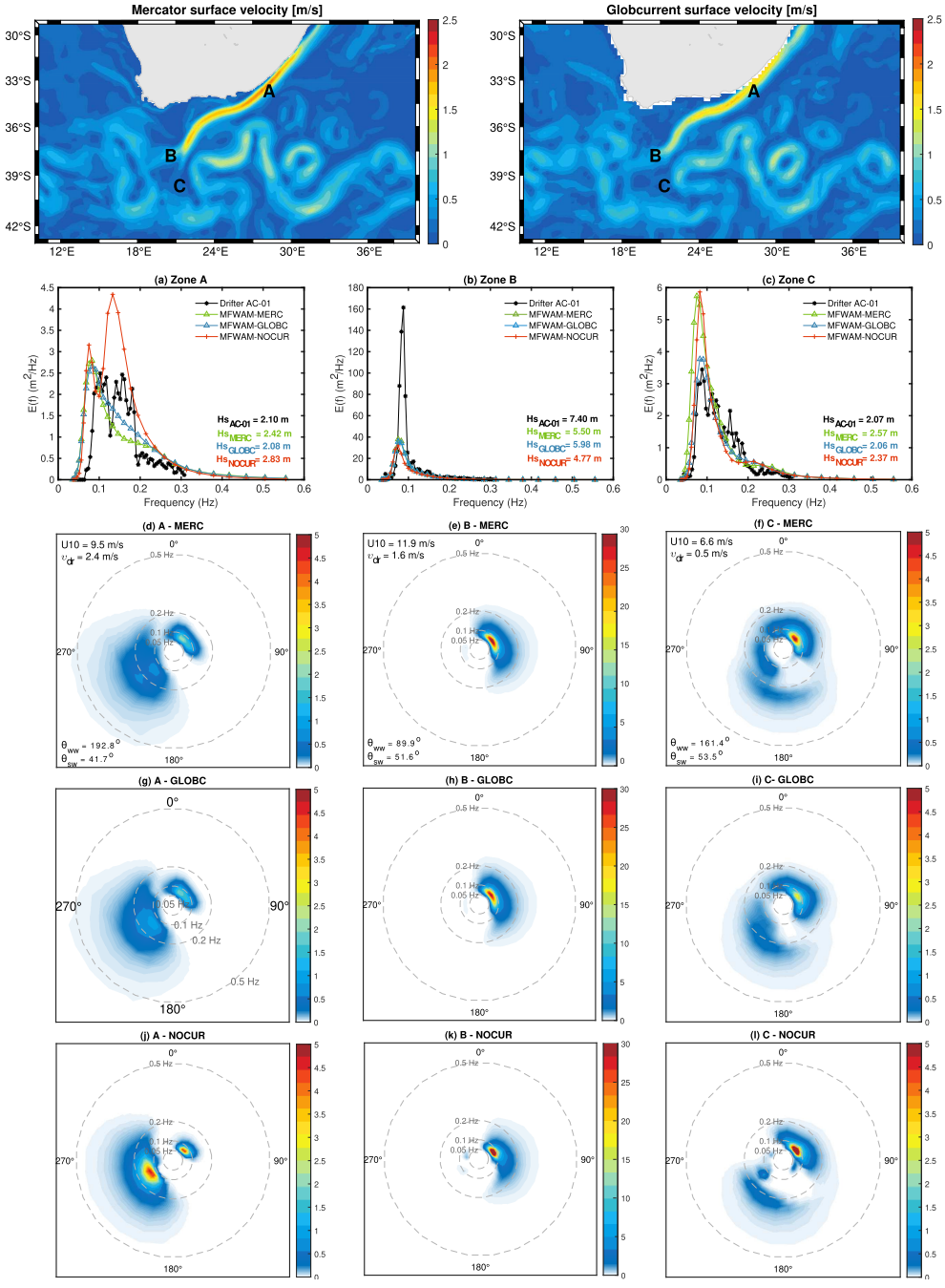

Figure 4.8: Maps of the Mercator *(top-left)* and Globcurrent *(top-right)* surface velocities averaged over January-February 2023. MFWAM and drifter-derived unidirectional *(a-c)* and MFWAM directional *(d-l)* wave spectra ($m^2/Hz/deg$) in the current core (A) and its retroflection (B,C) using Mercator (MERC), Globcurrent (GLOBC) and without current forcing (NOCUR). Parameters: MFWAM wind wave direction (θ_{ww}) and primary swell direction (θ_{sw}), ERA5 wind speed ($U10$) and drifter derived surface speeds (v_{dr}).

Continuing with the retroflection area, zone C involves a much weaker current, approximately $0.5\,\mathrm{m\,s^{-1}}$. Similar to zone A, swells travel northeast (53.5°), while a weaker wind sea originates from the opposite direction (161.4°). The significant wave height is recorded at 2.07 m, with Globcurrent providing an accurate forecast at 2.06 m (panel c). In contrast, both the Mercator and no-current scenarios reveal larger wave energy peaks, leading to wave height overestimations by 50 and 30 cm, respectively. Signs of wave energy spread are still evident when currents are included in the directional wave spectra, but they are much less pronounced than in zone A due to the weaker current strength (panels f, i vs l). In terms of swell modulations, the MFWAM-Globcurrent run aligns well with the no-current scenario, showing a 12-second peak wave period compared to 13 seconds for the MFWAM-Mercator product. However, the MFWAM-Globcurrent wave spectrum reveals a significant decrease in wave energy around the peak period. Consulting the drifter one-dimensional wave spectrum, it is evident that the MFWAM-Globcurrent run demonstrate better alignment with the drifter measurements.

Overall, the analysis of wave spectra between the standard MFWAM runs, using the Mercator current product, and those computed after forcing the wave system with satellite observations, i.e., Globcurrent, reveals that the latter shows better agreement with the in situ measurements. As discussed in detail in Section 4.3.1, the Mercator product underperforms compared to Globcurrent, showing extreme variability in the region of interest. Specifically, for drifter AC-01, which this analysis examines, the correlation between the drifter and the model was calculated at 0.49, while Globcurrent achieved a significantly higher correlation at 0.84 (Figure 4.3). Furthermore, some observed discrepancies can be attributed to Mercator's inability to effectively resolve mesoscale vorticity [32]. This shortfall may lead to significant errors, particularly in regions with strong currents like the Agulhas region.

4.5 Satellite Altimetry

4.5.1 Signatures of Current-Induced Wave Modulations

As previously mentioned, wave refraction is not a local process. Waves continue to be modulated by currents many kilometers away from their initial point of interaction [120]. While drifters are useful for validation and calibration activities, and essential for localised wave field monitoring, using them to monitor and study the impact of refraction across wide areas is impractical as one would need to deploy hundreds of drifters simultaneously to effectively capture its spatial extent. To investigate wave refraction on a broader scale, we use the Global Ocean L3 1-Hz significant wave height product from near-real-time satellite observations (`https://doi.org/10.48670/moi-00179`). This dataset includes data from Sentinel-3A/B, Sentinel-6, CFOSAT, ALTIKA, CryoSat-2, HY-2B, and Jason-3. These satellites provide comprehensive coverage that enables a detailed analysis of wave refraction patterns over extensive geographic areas and under various conditions.

To evaluate the performance of the satellites against drifters, we first conducted a comparative analysis. For the mono-mission satellite-based along-track significant wave

height measurements, collocations were implemented using constraints of a 15-minute time window and a 20-kilometer radius around each independent drifter record using the open-source WAVY software (`https://github.com/bohlinger/wavy`, Bohlinger *et al.* [137]). Figure 4.9 illustrates the significant wave height time series, demonstrating good agreement between in situ measurements and satellite observations across a wide range of wave conditions and regardless of whether the sensors were positioned around the core of the current or its associated eddies.

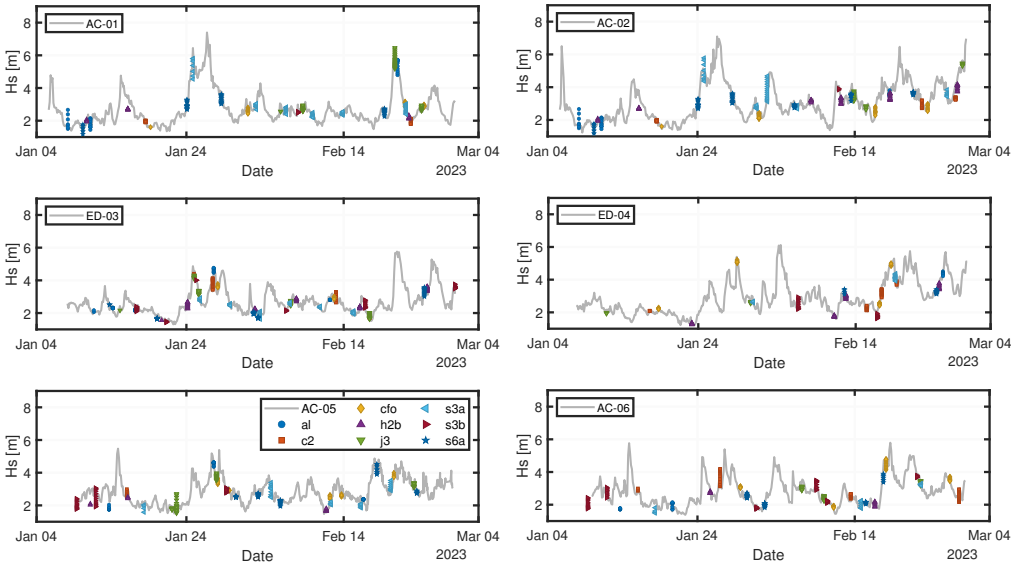

Figure 4.9: Time series of significant wave height measurements per drifter along with collocated satellite altimetry observations obtained from the Copernicus Global Ocean L3 Significant Wave Height product (1 Hz). Collocation criteria: 20 km and 15 min around each drifter measurement point. The satellite observations from Altika-SARAL (al), CryoSat-2 (c2), Jason-3 (j3), CFOSAT (cfo), HY-2B (h2b), Sentinel-3A/B (s3a/s3b), Sentinel-6A (s6a) are color coded.

To quantify this agreement, a comparison of the closest satellite records to each drifter position was performed, revealing a correlation of 0.97 and an RMSE of 24 cm. Since no interpolation was applied to match the exact drifter positions, part of the discrepancies may be attributed to wave height modulations induced by wave-current interactions, including refraction effects that continue to develop several kilometers away from the drifters' locations. It is noteworthy that the satellites demonstrate good performance even in high sea-state conditions. For instance, Sentinel-3A and Jason-3 along with Altika measured wave heights up to 6 m on January 24 and February 20, respectively, observations in line with drifer AC-01's measurements. Similarly, between 25 and 29 January CFOSAT, CryoSat-2, Jason-3 and Altika captured wave heights of approximately 4.5 and 5 m around the eddies, aligning well with the measurements from drifters ED-03 and ED-04.

Figure 4.10 provides insights into the evolution of refraction. Estimates of significant wave heights along the paths of drifters AC-05 (left panel) and ED-03 (right panel) are illustrated, superimposed on Mercator current velocities averaged over the period January-February 2023. In this deep-water region, collocated altimeter tracks extend hundreds of kilometers from the drifters' points, demonstrating how the wave heights are modulated by the Agulhas Current and its surrounding eddies. Notably, waves, regardless of their initial height, exhibit pronounced modulations when traversing the area of current return and the observed eddy. In contrast, tracks that span regions outside the influence of the current, where surface speeds are reported below $0.5\,\mathrm{m\,s^{-1}}$ (h2b1, h2b4), show only minor variations in wave height. Within the eddies, waves are observed to either steepen (h2b$_3$) or flatten (s3b). Several studies have reported that these dynamics are significantly influenced by the direction in which the waves encounter the current [32, 132, 114]. Considering the additional information acquired by the drifters in our study, this collocation experiment provides clear evidence of the importance of using multi-source data to map the complex interactions between waves and currents as well as their spatial extent in regions with strong currents.

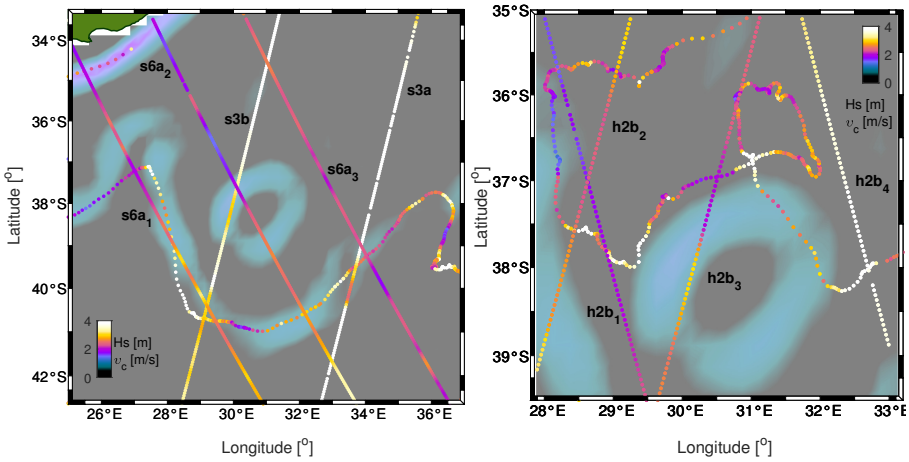

Figure 4.10: Mean Mercator current velocities with superimposed significant wave height estimates from drifter AC-05 *(left panel)* between January 9, 2023 and February 28, 2023, and from drifter ED-03 *(right panel)* between January 9, 2023 and February 20, 2023. Collocated altimetry data from Sentinel-3A/B (s3a/s3b), Sentinel-6A (s6a), and HY-2B (h2b) are also illustrated, using as criterion a 15-minute acquisition time difference between satellite observations and drifters' measurements.

4.5.2 Evaluation of Intensity Modulation Spectra from Various Sensors

As discussed in Section 4.4.2, swell waves are only marginally affected by ocean currents. Given that, the analysis is extended by cross-comparing different remote sensing technologies providing long wave observations, using as reference in situ measurements. The

Sentinel-1 mission, a constellation of C-band SAR side-looking satellites launched in 2014, 2016 (early end of mission in 2022) and 2024, was designed to measure, among others, directional wave spectra by collecting radar images over the ocean in Wave Mode [138]. Notably, long waves can also be imaged in coastal areas, where Sentinel-1 operates in Extra Wide Swath Mode. Although no operational wave spectrum product is currently available for this data acquisition mode, preliminary comparisons of intensity modulation spectra with Sentinel-6A have shown good agreement in swell retrieval [100]. CFOSAT, launched in 2018, carries a wave spectrometer at Ku-band, named Surface Waves Investigation and Monitoring (SWIM), pointing at 6 incident angles between 0 and 10° with a rotating beam antenna over 360° [139]. The nadir-looking configuration provides wind speed and significant wave height estimates, while the off-nadir looking signals are used to compute directional wave spectra. Since the inversion of intensity modulation spectra into ocean wave spectra has not yet developed for SAR altimeters, we focus on cross-comparing modulation spectra products, using as reference drifter-derived wave spectra.

Case study 1: Sentinel-6A vs CFOSAT

On January 6, 2023, the drifter ED-04 recorded long swells with a peak wave period of about 16 sec (0.063 Hz) and an overall (wind and swells) significant wave height of 2.3 m. A crossover was identified between CFOSAT and Sentinel-6A at a distance of approximately 100 km from the drifter (34.10° S, 34.45° E), as illustrated in Figure 4.11. The time difference between acquisitions from both satellites and drifter was less than 1 hour. The white box represents the processing window (70 x 90 km) used for the computation of the CFOSAT SWIM modulation spectrum, which was freely downloaded by the AVISO+[4] website. The purple lines represent the processing window of Sentinel-6A (3 x 90 km). The Sentinel-6A modulation spectrum was computed as described in Altiparmaki *et al.* [84] using level-1A products from the EUMETSAT's[5] data catalogue. To match the area covered by CFOSAT, the Sentinel-6A modulation spectrum was computed by averaging six consecutive spectra, each computed in windows of 15 km along-track.

Figure 4.12 presents both the satellite-derived modulation spectra and drifter-derived frequency wave spectrum. Similar to SAR imaging, CFOSAT's spectra exhibit a directional ambiguity of 180° [57], while the SAR altimeter reveals two additional peaks caused by receiving signals from both sides of the ground footprint, resulting in inseparable returned signals, as detailed in Altiparmaki *et al.* [84]. Since the source of these replicas was investigated in detail in Chapter 2, their interpretation will be excluded from the discussion. The drifter's wave spectrum reveals a narrow low-frequency swell peak that is about four times larger than the high-frequency wind-wave components, indicating swell dominance at the time of acquisition. However, wind speeds recorded by both CFOSAT and Sentinel-6A, shown in Figure 4.11, exceed 15 m/s, suggesting the presence of high sea states around the crossover area. Examining peak wave period estimates, both satellites align closely with in situ measurements, with recorded values of 15.5, 15.2, and 15.8 seconds for Sentinel-6A,

[4] https://www.aviso.altimetry.fr/en/missions/current-missions/cfosat/access-to-data.html

[5] https://www.eumetsat.int/sentinel-6

CFOSAT, and the drifter, respectively.

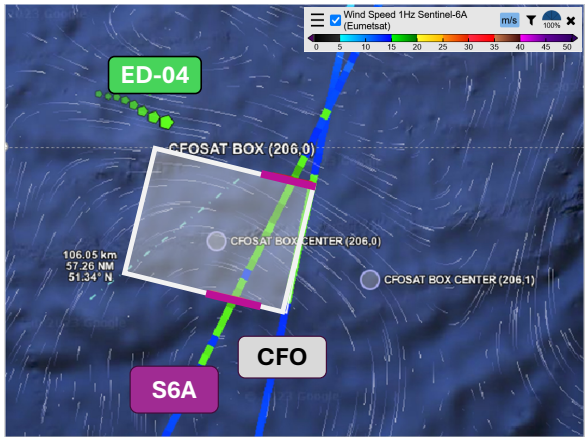

Figure 4.11: Sentinel-6A (S6A) and CFOSAT (CFO) passes, depicting wind speed observations, on the 16th of January 2023, visualized in Ocean Virtual Laboratory (OVL), OceanDataLab. The white box represents the processing area used for the CFOSAT modulation spectrum acquisition, while the purple lines represent the boundaries of the processing window for Sentinel-6A. The ED-04 drifter trajectory is visualized with the green hexagon markers. In the background the geostrophic surface current streamlines from Globcurrent are shown. Snapshot from OVL: `https://odl.bzh/hQ93fvMz`.

In terms of peak wave direction, CFOSAT and Sentinel-6A capture peaks at 229° (or 49°) and 210° (or 30°) with respect to North, demonstrating reasonably good agreement. As no directional data are available from the in situ measurements, the true swell direction cannot be confirmed. Additionally, a slightly weaker peak appears in both modulation spectra at lower frequencies, around 240-250°, suggesting the presence of a secondary, less energetic swell system, also captured in the drifter's spectrum at around 17 sec (0.058 Hz).

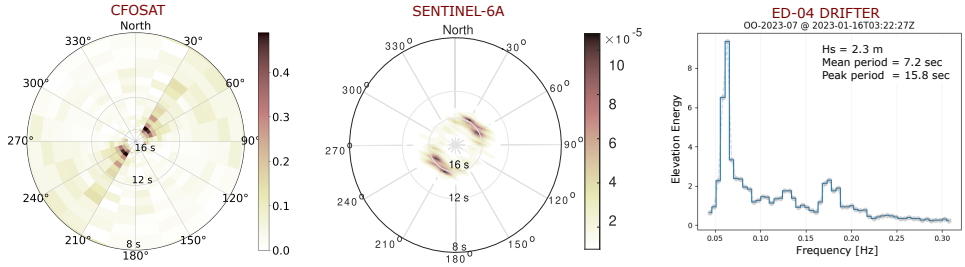

Figure 4.12: Directional modulation spectrum from CFOSAT *(left panel)*, directional modulation spectrum from Sentinel-6A *(middle panel)* and frequency wave spectrum from the ED-04 drifter *(right panel)* on 16 January 2023. The values in the colorbar represent power spectral density.

Case study 2: Sentinel-3B vs Sentinel-1A

On January 16, 2023, the drifter ED-03 measured swell waves with a peak period of about 14 sec (0.070 Hz) and an overall significant wave height of 2.6 m. Around 100 km from the drifter's location (35.70° S, 28.39° E), a Sentinel-3B pass coincided with a Sentinel-1A radar image acquired in Extra Wide Swath Mode, as illustrated in Figure 4.13. The acquisition time difference between the spaceborne observations and the in situ measurements was less than 4 hours. The white box represents the processing window for Sentinel-1A (20 x 20 km). For consistency, the Sentinel-3B window was set to the same length along-track, with a cross-track ground coverage window of 3 km (3 x 20 km).

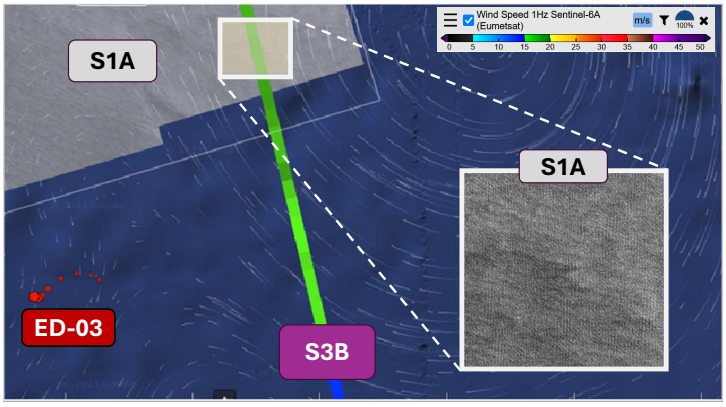

Figure 4.13: Sentinel-3B (S3B) pass, depicting wind speed observations, and Sentinel-1A (S1A) Extra Wide Swath Mode acquisition on the 16th of January 2023, visualized in Ocean Virtual Laboratory (OVL), OceanDataLab. The white box represents the processing area used for the Sentinel-1A and Sentinel-3B modulation spectra computation. The ED-03 drifter trajectory is visualized with the red hexagon markers. In the background the geostrophic surface current streamlines from Globcurrent are shown. Snapshot from OVL: `https://odl.bzh/dILfrjIj`.

Figure 4.14 compares the intensity modulation spectra from Sentinel-3B's nadir-looking SAR and Sentinel-1A's side-looking SAR, alongside the drifter's frequency wave spectrum. The latter reveals two high-energy peaks at frequencies below 0.10 Hz, indicating the presence of two distinct swell systems, along with a significantly lower peak at higher wind-driven frequencies. Wind speed measurements from Sentinel-3B suggest relatively high local wind sea conditions with values exceeding 15 m/s.

Sentinel-3B and Sentinel-1A show good agreement in measuring the peak wave period, with values of 14.4 and 14.8 seconds, respectively, while the drifter records slightly shorter waves at 13.7 seconds. However, there is a notable difference in peak wave direction: Sentinel-1A registers the most energetic peak at 273° (or 93°) relative to North (swell 1), while Sentinel-3B's peak is captured at 220° (or 40°). Examining the Sentinel-1A spec-

trum more closely, a second, weaker peak is observed around 220° (swell 2), which aligns well with Sentinel-3B. The fact that Sentinel-3B does not capture the most energetic swell system can be attributed to the large cutoff wavelength in the cross-track direction, where resolution loss can be more pronounced than in the along-track direction under moderate and high sea state conditions, and is proportional to significant wave height [96]. The dashed orange arrow, representing the satellite azimuth, confirms that the swell 1 system is traveling nearly in the cross-track direction. Considering that the significant wave height reaches 2.6 m according to drifter data, the cross-track cutoff wavelength could exceed 300 m (Eq. 29, Kleinherenbrink *et al.* [96]), which is comparable to the estimated peak wavelength in this case (a 14.4 sec wave period corresponds to a wavelength of approximately 325 m using linear wave theory). This example highlights the advantage of using a larger cross-track measurement window for retrieving swell spectra, as discussed for Sentinel-6A in Chapter 2.4.2. Lastly, although Sentinel-1A is capable of measuring wind waves with wavelengths at least as short as 30 m when it operates in Wave Mode, no high-frequency signals are observed in this case. This could be attributed to the resolution of the radar image used in this analysis, which was acquired in Extra Wide Swath Mode and has a lower ground resolution compared to Wave Mode (20 x 40 m versus 5 x 5 m).

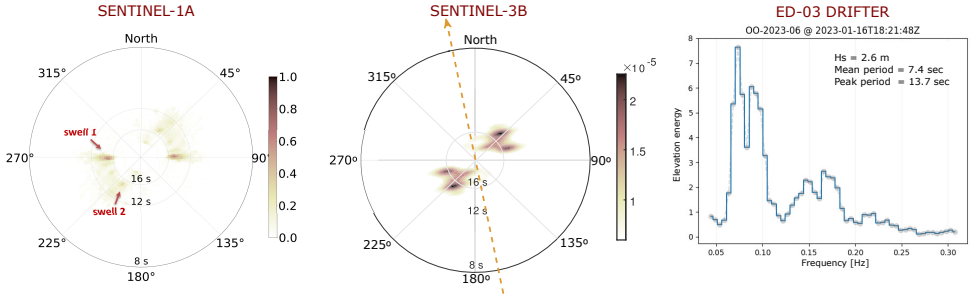

Figure 4.14: Directional modulation spectrum from Sentinel-1A *(left panel)*, directional modulation spectrum from Sentinel-3B *(middle panel)* and frequency wave spectrum from the ED-03 drifter *(right panel)* on 16 January 2023. The values in the colorbar represent power spectral density.

4.6 Conclusions and Recommendations

This study has investigated in situ wave measurements collected in the Agulhas Current during the ESA-PECO2 Advanced Ocean Training Course 2023, part of the One Ocean Expedition 2021-2023, to evaluate the influence of wave-current interactions on wave models and altimetry-derived products. In January 2023, six OpenMetBuoy drifters were deployed in the Indian Ocean, in and around the Agulhas Current. Over approximately two months, these drifters recorded wave spectra and their location, enabling the estimation of significant wave height and Stokes drift along their paths. Additionally, drifter speeds were estimated using GPS data, allowing estimates of surface current speeds, as the drifters experienced minimal direct windage due to their high immersion ratio.

The analysis first focused on surface current products. The Copernicus ESA Globcurrent product combines altimetry-derived geostrophic currents with Ekman drift computed from atmospheric forecasts. We found that this product tends to underestimate surface velocities exceeding approximately $0.5\,\mathrm{m\,s^{-1}}$. A similar underestimation with a significantly greater variability was observed for the Mercator surface current product. Moreover, circular trajectories indicative of inertial oscillations were observed over periods of days, likely driven by rapid changes in wind speed and direction.

Further, we compared modeled surface Stokes drift and significant wave height from ERA5 and MFWAM with the in situ measurements. ERA5 consistently underestimated significant wave heights over 2.5 m, while MFWAM demonstrated good agreement with drifter data. Both models tended to overestimate the Stokes drift, with ERA5 showing greater variability. The absence of current forcing in ERA5, coupled with its coarser spatial resolution ($1/2°$) compared to MFWAM ($1/12°$), likely contributes to the decreased accuracy of ERA5 in areas with strong currents, emphasizing the complexities and challenges in accurately modeling wave-current interactions in dynamic regions like the Agulhas Current.

A customized MFWAM run which excludes current forcing revealed an underestimation of wave height, occasionally exceeding 2 m as current velocities increase compared to drifter current estimates. A comparison of the directional MFWAM wave spectra, both with and without current data, demonstrated how current-induced refraction alters the shape of the wave spectra. The refraction bends the waves, causing them to become steeper or flatter and directionally more spread. Furthermore, the MFWAM model forced with Globcurrent surface currents tends to align closely with drifter observations and even outperforms the operational MFWAM model that uses Mercator-derived currents.

The study continued with a comparative analysis of significant wave heights from the drifters with those from collocated satellite altimeter observations from various missions, showing good correspondence. Notably, current-induced wave refraction patterns are observed along the satellite tracks, with wave heights being significantly modulated when crossing eddies or the current core. These findings highlight the need for high-resolution models and multi-source data integration to achieve accurate wave forecasts.

Moreover, a multi-mission analysis of swell parameters demonstrated good agreement between various remote sensing technologies and in situ data. While Sentinel-1 and CFOSAT provide accurate swell observations through well-established techniques, no operational swell data are currently available from SAR altimeters. With four SAR altimeters currently in orbit (Sentinel-3A/B, Sentinel-6A, and CryoSat-2) and the anticipated launches of two more (Sentinel-6B in 2025 and Sentinel-3C in 2026), a synergistic approach could substantially enhance wave products, offering high temporal and spatial resolution data crucial for oceanographic studies and forecasts.

Lastly, the authors would like to emphasize that the data analyzed in this study were collected during the Australian summer, a period with comparably milder storm activity relative to the winter season in the southern region. A year-round field campaign would be necessary for a comprehensive validation of satellite products and models, as it would capture a wider spectrum of sea states and current variability, including extreme conditions associated with storm periods, where the examined products demonstrated increased sensitivity.

4.7 Supporting Material

This section provides supplementary information regarding the analyses between wave models, satellite observations and in situ measurements. In particular, Figure A1 presents scatter plots illustrating the relationship between Stokes drift values estimated by drifters and those estimated by the ERA5 (top panels) and MFWAM (bottom panels) models. Each subplot represents collocated data in both time and space for each drifter separately. The scatter plots highlight areas of agreement and discrepancy, providing a visual representation of models performance.

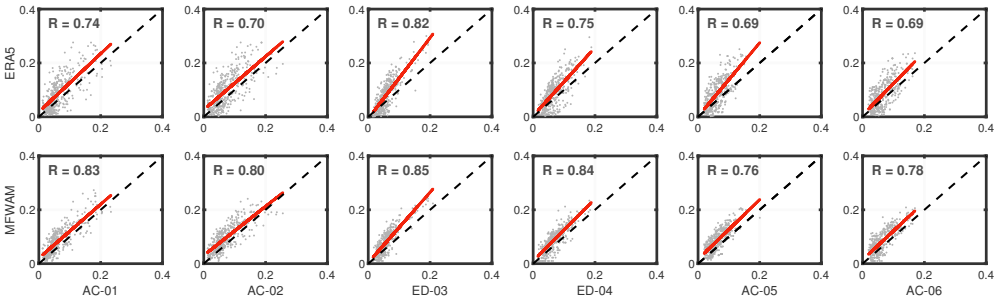

Figure A1: Scatter plots of surface Stokes drift versus ERA5 *(top panels)* and MFWAM *(bottom panels)* for each drifter separately. A regression line is shown in red color. The dashed black line represents the line of equality when in situ = model. Unit: $\mathrm{m\,s^{-1}}$

Similarly, Figure A2 depicts scatter plots for significant wave height, comparing the drifter measurements with those derived from the ERA5 (top panels) and MFWAM (bottom panels) models.

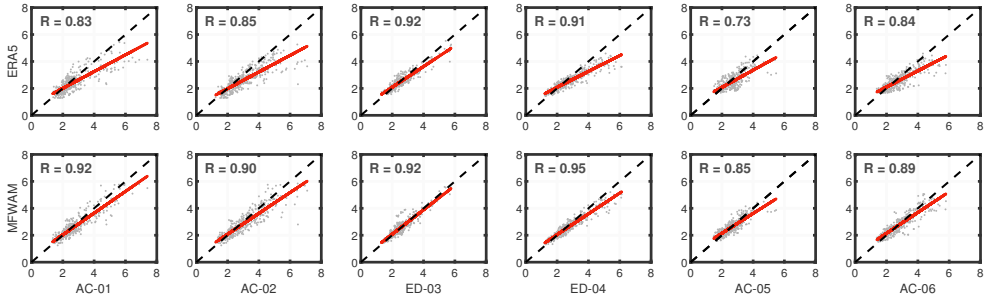

Figure A2: Scatter plots of significant wave height from drifters versus ERA5 *(top panels)* and MFWAM *(bottom panels)* for each drifter separately. A regression line is shown in red color. The dashed black line represents the line of equality when in situ = model. Unit: m

Table A1 summarizes statistics of all examined scenarios. Key metrics, including root

mean square error (RMSE), mean (bias), and standard deviation (Std. Dev.), provide a quantitative assessment of the performance of all the examined current and wave products against drifters. The correlation coefficients (Corr. Coef.) further indicate the strength of the linear relationship between models, satellite observations and in situ measurements. In addition, Figure A3 presents scatter plots of significant wave height (left-panel) and Stokes drifts (right-panel) as obtained from the drifters and the customized MFWAM runs.

Table A1: Statistics of the differences and correlation coefficients of wave models and satellite-derived products against in situ measurements from the OpenMetBuoy (OMB) drifters.

	Bias	**Std.Dev.**	**RMSE**	**Corr. Coef. (-)**
Surface current speed [$\mathrm{m\,s^{-1}}$]				
Mercator – OMB	-0.06	0.52	0.52	0.51
Globcurrent – OMB	-0.09	0.31	0.32	0.84
Surface Stokes drift [$\mathrm{m\,s^{-1}}$]				
ERA5 – OMB	0.03	0.04	0.05	0.72
$\mathrm{MFWAM_{MERC}}$ – OMB	0.02	0.03	0.04	0.80
$\mathrm{MFWAM_{GLOBC}}$ – OMB	0.03	0.03	0.04	0.75
$\mathrm{MFWAM_{NOCUR}}$ – OMB	0.03	0.03	0.04	0.78
Significant wave height [m]				
ERA5 – OMB	-0.23	0.48	0.54	0.83
$\mathrm{MFWAM_{MERC}}$ – OMB	-0.04	0.38	0.39	0.90
$\mathrm{MFWAM_{GLOBC}}$ – OMB	-0.04	0.39	0.39	0.91
$\mathrm{MFWAM_{NOCUR}}$ – OMB	-0.06	0.45	0.45	0.88

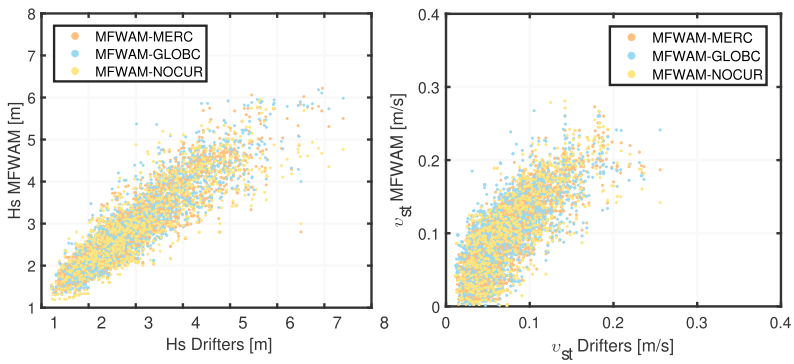

Figure A3: Scatter plots of significant wave height *(left-panel)* and surface Stokes drifts *(right-panel)* as obtained from the drifters and the customized MFWAM runs.

5

Conclusions and Recommendations

This chapter synthesizes the key conclusions of this research and suggests potential directions for future studies. For a detailed discussion of the conclusions, the reader is referred to Chapters 2, 3, and 4.

The primary objective of this PhD dissertation was to investigate the imaging capabilities of near-nadir looking SAR altimeters over ocean surfaces. To achieve this, the first step involved exploiting intensity modulations revealed in off-nadir full-focused SAR signals to develop and evaluate a method for characterizing long waves generated by storms, commonly referred to as swells. Next, the imaging limitations of the instrument were examined, focusing on resolution loss. Given the strong correlation between sea state conditions and resolution loss, this analysis also enabled the estimation of an independent sea-state parameter: the variance of wave orbital velocities. The secondary objective involved leveraging ground-truth data to assess the performance of altimetry products and wave models in the dynamic marine environment of the Agulhas Current, where waves interact strongly with ocean currents.

5.1 Conclusions

Exploring off-nadir signal modulations in fully-focused SAR altimetry for swell retrieval.

This study introduced a novel method for retrieving swell wave properties from fully-focused SAR altimetry data. Fully-focused SAR radargrams from CryoSat-2 revealed power modulations in the trailing edge of waveforms induced by swells. By normalizing the intensity and re-projecting the range bins to cross-track ground locations, a spectral analysis, similar to that used for side-looking SAR systems like Sentinel-1, was applied to compute intensity modulation spectra. This analysis was supported by a detailed description of the modulation mechanisms, using both analytical and numerical models. Unlike side-looking SAR spectra, which exhibit a 180-degree directional ambiguity, fully-focused SAR

altimetry spectra show power in four quadrants due to signal reception from both sides of the ground footprint. Range bunching was identified as a dominant mechanism in the RAR response, often surpassing velocity bunching, depending on the wave propagation angle. Overall, comparisons with buoy-derived directional wave spectra demonstrated good agreement. Among the SAR altimeters, Sentinel-6A's full-beam footprint offers distinct advantages in swell retrieval, especially for waves propagating in or near the cross-track direction, leveraging an extended observational window and increased ground resolution compared to its operational truncated data. With four active SAR altimetry missions, CryoSat-2, Sentinel-3A/B, and Sentinel-6A, and their successors anticipated in the near future, satellite-based swell observations can be significantly enhanced globally, especially benefiting the study of waves radiating from tropical cyclones. This is particularly important given that only two currently operational spaceborne instruments, onboard Sentinel-1 and CFOSAT, provide wave spectra products.

Investigating the wave imaging limitations and sea-state characterization in fully-focused SAR altimetry using azimuth cutoff analysis.

The demonstration of acquiring swell-induced intensity modulation spectra from fully-focused SAR data led to the next research objective: the wave imaging limitations of SAR altimeters. This was addressed by estimating the azimuth cutoff wavelength, a proxy for the shortest waves detectable by the SAR system across a wide range of sea states and measurement geometries. First, using a well-established approach implemented in the spatial domain in side-looking SAR, the azimuth cutoff was estimated by minimizing the residuals between the along-track autocorrelation function of fully-focused SAR radargrams and a fitted Gaussian function. Sentinel-6A data from a 10-day repeat cycle were used for the analysis and the results were compared with model-derived values from ERA5 and MFWAM. The analysis revealed that the satellite effectively captures waves longer than approximately 100 meters in calm wind and sea states. However, increasing wind speed and significant wave height led to underestimations, an observation also reported in relevant side-looking SAR studies, such as Stopa *et al.* [27]. This study showed that the spatial domain approach performs well under moderate wind and wave conditions, with azimuth cutoff values exceeding 200 meters. When swells dominate the sea state, abnormal overestimations of the azimuth cutoff were observed, with errors strongly influenced by the swell propagation angle relative to the satellite azimuth. In particular, cross-track traveling waves introduced larger discrepancies than along-track traveling waves, which aligns with findings from relevant side-looking SAR studies. To investigate the mitigation of swell-related errors, an alternative method was developed in the wavenumber domain. This approach involved fitting a high-order polynomial to the decaying part of the spectral autocorrelation function and identifying the fall-off width using an empirically defined threshold. As a result, azimuth cutoff estimates improved correlations with modeled-derived values by 10% (from 0.70 to 0.80). Next, considering the high correlation between resolution loss and sea-state conditions, previously reported in SAR imaging, the azimuth cutoff parameter was used to derive an independent sea-state parameter: the variance of wave orbital velocities. Wave orbital velocity statistics offer valuable insights into wave climate by isolating wave components associated with developing seas. Comparisons with ERA5 and MFWAM showed velocity variance root mean square errors ranging from 0.22 to

$0.26\ m^2\ s^{-2}$, with the smallest errors observed in comparisons with MFWAM. Lastly, knowing that nadir-looking altimeters capture only a small portion of the total distribution of vertical wave particle velocities, as reported in Buchhaupt *et al.* [86], the underestimation trend in high sea states for both azimuth cutoff and wave orbital velocity variance suggests that this is an inherent limitation of the measurement geometry.

Assessing the reliability of wave and ocean current products from models and remote sensing observations in current-dominated oceanic environments.

This study utilized in situ wave measurements collected in the Agulhas Current region during the One Ocean Expedition in January 2023 to evaluate the impact of wave-current interactions on wave products from models and satellite altimeters. The analysis showed that the ocean surface current products from Mercator and the altimetry-derived Globcurrent underestimated velocities exceeding 0.5 m/s, with Mercator exhibiting significantly higher variability. Modeled Stokes drifts from ERA5 and MFWAM were found to be overestimated compared to drifter measurements, likely due to the use of a Phillips wave spectrum shape for the high-frequency range in both models, which tends to distribute excess energy in this part of the spectrum. ERA5 consistently underestimated wave heights above 2.5 m, while MFWAM demonstrated good agreement with drifter data. This discrepancy was attributed to the absence of ocean current forcing in ERA5. Customized MFWAM runs without current forcing further supported this observation, particularly in regions with strong currents and high sea states. The inclusion of current data showed that refraction significantly alters wave spectra, making waves steeper or more flattened depending on the relative direction of currents and waves. Among the models tested, MFWAM forced with the altimetry-derived Globcurrent product aligned most closely with drifter measurements, outperforming the operational MFWAM model that relies on Mercator currents. Additionally, comparisons of significant wave height between satellite altimeter observations and drifters showed good agreement, with clear evidence of current-induced wave refraction patterns along satellite tracks. A multi-mission analysis of intensity modulation spectra, involving Sentinel-1, CFOSAT, and SAR altimeters, demonstrated good agreement with in situ data, particularly for swell retrieval. This further enhances the potential for synergistic use of these instruments in operational oceanographic applications and climate studies.

5.2 Recommendations

Based on these conclusions, recommendations for future developments and research are summarized below:

- **Development of a Swell Wave Spectrum Product from SAR Altimetry Data**
  While SAR altimeters were not originally designed for imaging applications, this dissertation has demonstrated that off-nadir signals, previously considered as nuisance, contain valuable information about ocean surface features. Future research should focus on further refining the retrieval of fully-focused SAR modulation spectra, with an emphasis on their inversion into ocean wave spectra. Although retrieving the full wave spectrum from near-nadir looking systems is not feasible due to resolution limitations [84, 140, 96], significant potential exists for developing a new operational swell product. When combined with Sentinel-1 and CFOSAT data, this product could enhance our understanding of how swell waves are radiating from storms. This development could also represent a major milestone in the field of satellite altimetry: the estimation of significant wave height for swells. By combining the proposed trailing-edge analysis with conventional leading-edge analysis, which provides total significant wave height observations, would, for the first time, allow the separation of swell and wind waves in satellite altimetry.

- **Re-evaluation of the Onboard Signal Truncation in Sentinel-6**
  As discussed in Chapter 2.4.2, Sentinel-6A employs an onboard signal truncation processor, reducing the data rate by a factor of two. This dissertation demonstrated that this truncation affects swell retrieval, particularly when waves travel across-track, thereby limiting its applicability and, consequently, its performance for future operational use. Although this truncation is implemented to manage data volume downlink, the availability of RAW (non-truncated) SAR data should be reconsidered to fully utilize the instrument's capabilities. A potential solution, inspired by the Sentinel-1 Wave Mode, could involve defining an additional acquisition mode mask for RAW SAR data over targeted ocean regions where swells are known to dominate throughout the year. Using linear wave propagation theory, such data could then be used not only to track the evolution of swell systems, but also to identify their generation regions, supporting both forecasting and hindcasting applications.
- **Synergestic Use of Remote Sensing Technologies**
  Collaborative analysis of wave spectra between SAR altimeters, side-looking SAR systems and CFOSAT should be further expanded to enhance the understanding of scattering mechanisms and spectral responses. Leveraging crossovers between these technologies offers a unique opportunity to refine and cross-validate observations. For instance, applying the azimuth cutoff autocorrelation method to Sentinel-3 and Cryosat-2 requires careful consideration of their operational mode. Unlike Sentinel-6A's open-burst mode, these satellites operate in closed-burst mode, which introduces azimuthal ambiguities every approximately 90 m [6], and is expected to affect the shape of the azimuth autocorrelation function. Investigating the extent of this effect is crucial for assessing the ability of these satellites to provide reliable wave orbital velocity statis-

tics. Moreover, cross-validation campaigns are essential for developing consistent operational products that complement the strengths and address the limitations of each spaceborne sensor.

- **Improvement of Wave Models in Current-Dominated Marine Environments**

  Providing accurate wave data to users and scientists is essential, from supporting maritime navigation to operational planning and climate studies, especially as extreme weather events become more frequent. This dissertation demonstrated that operational wave products, widely used for forecasting and climate studies, often lack accuracy when currents are not properly modeled, particularly in extreme sea states. Therefore, high-resolution wave models and reanalysis products that integrate multi-source data should continue to be developed, with a focus on regions experiencing strong wave-current interactions. Incorporating accurate ocean current data into wave models, particularly in dynamic marine environments like the Agulhas Current region, is expected to significantly enhance the reliability of forecasts.

- **Year-Round Field Campaigns to Enhance Satellite Observations and Wave Model Reliability**

  As our planet faces an escalating climate crisis with increasingly frequent extreme events, the need to monitor and understand these phenomena for predicting their future occurrence has never been more critical. With the growing number of Earth Observation missions focused on ocean monitoring, each incorporating advanced technological innovations, there is a clear need for continuous calibration and validation of spaceborne sensors to ensure the reliability of their products. Year-round field campaigns covering diverse sea states, including extreme storm conditions, are strongly recommended to comprehensively validate satellite observations and enhance the performance of wave models through data assimilation. The use of low-cost drifters, like those deployed during the One Ocean Expedition, offers a practical way to extend observational coverage while minimizing operational expenses.

Bibliography

[1] L.-L. Fu and A. Cazenave, eds., *Satellite Altimetry and Earth Sciences: A Handbook of Techniques and Applications*, International Geophysics, Vol. 69 (Academic Press, San Diego, CA, 2000).

[2] C. L. MacArthur, *The Seasat Radar Altimeter,* Johns Hopkins APL Technical Digest **16**, 223 (1986).

[3] R. Raney, *The delay/Doppler radar altimeter,* IEEE Trans. Geosci. Remote Sens. **36**, 1578–1588 (1998).

[4] A. Egido and W. H. F. Smith, *Fully Focused SAR Altimetry: Theory and Applications,* IEEE Transactions on Geoscience and Remote Sensing **55**, 392 (2017).

[5] F. Schlembach, F. Ehlers, M. Kleinherenbrink, M. Passaro, D. Dettmering, F. Seitz, and C. Slobbe, *Benefits of fully focused SAR altimetry to coastal wave height estimates: A case study in the North Sea,* Remote Sensing of Environment **289**, 113517 (2023).

[6] M. Kleinherenbrink, M. Naeije, C. Slobbe, A. Egido, and W. Smith, *The performance of CryoSat-2 fully-focussed SAR for inland water-level estimation,* Remote Sensing of Environment **237**, 111589 (2020).

[7] P. Rieu, T. Moreau, E. Cadier, M. Raynal, S. Clerc, C. Donlon, F. Borde, F. Boy, and C. Maraldi, *Exploiting the Sentinel-3 tandem phase dataset and azimuth oversampling to better characterize the sensitivity of SAR altimeter sea surface height to long ocean waves,* Advances in Space Research **67**, 253 (2021).

[8] D. B. Chelton, J. C. Ries, B. J. Haines, L.-L. Fu, and P. S. Callahan, *Chapter 1 Satellite Altimetry,* in *Satellite Altimetry and Earth Sciences*, International Geophysics, Vol. 69, edited by L.-L. Fu and A. Cazenave (Academic Press, 2001) pp. 1–ii.

[9] G. Brown, *The average impulse response of a rough surface and its applications,* IEEE Transactions on Antennas and Propagation **25**, 67 (1977).

[10] G. Hayne, *Radar altimeter mean return waveforms from near-normal-incidence ocean surface scattering,* IEEE Transactions on Antennas and Propagation **28**, 687 (1980).

[11] L. Bao, Y. Lu, and Y. Wang, *Improved retracking algorithm for oceanic altimeter waveforms,* Progress in Natural Science **19**, 195 (2009).

[12] M. Passaro, P. Cipollini, S. Vignudelli, G. D. Quartly, and H. M. Snaith, *ALES: A multi-mission adaptive subwaveform retracker for coastal and open ocean altimetry,* Remote Sensing of Environment **145**, 173 (2014).

[13] S. Dinardo, L. Fenoglio-Marc, C. Buchhaupt, M. Becker, R. Scharroo, M. Joana Fernandes, and J. Benveniste, *Coastal SAR and PLRM altimetry in German Bight and West Baltic Sea,* Advances in Space Research **62**, 1371 (2018), the CryoSat Satellite Altimetry Mission: Eight Years of Scientific Exploitation.

[14] T. Moreau, N. Tran, J. Aublanc, C. Tison, S. Le Gac, and F. Boy, *Impact of long ocean waves on wave height retrieval from SAR altimetry data,* Advances in Space Research **62**, 1434 (2018), The CryoSat Satellite Altimetry Mission: Eight Years of Scientific Exploitation.

[15] F. Reale, E. Carratelli, I. Laiz, A. Di Leo, and F. Dentale, *Wave Orbital Velocity Effects on Radar Doppler Altimeter for Sea Monitoring,* J. Marine Sci. Eng. **8 (6)** (2020), 10.3390/jmse8060447.

[16] R. Torres, P. Snoeij, M. Davidson, D. Bibby, and S. Lokas, *The Sentinel-1 mission and its application capabilities,* in *2012 IEEE International Geoscience and Remote Sensing Symposium* (2012) pp. 1703–1706.

[17] W. G. Carrara, R. S. Goodman, and R. M. Majewski, *Spotlight Synthetic Aperture Radar: Signal Processing Algorithms* (Artech House, Boston, MA, 1995).

[18] M. Raynal, T. Moreau, N. Tran, F. Labroue, F. Boy, P. Féménias, and F. Borde, *Assessment of the SARM processing sensitivity to swell,* Ocean Surface Topography Science Team Meeting 2018 (2018).

[19] F. Reale, F. Dentale, E. Carratelli, and F.-M. L., *Influence of Sea State on Sea Surface Height Oscillation from Doppler Altimeter Measurements in the North Sea,* Rem. Sens. **10** (2018), 10.3390/rs10071100.

[20] P. Rieu, T. Moreau, M. Raynal, E. Cadier, P. Thibaut, F. Borde, C. Donlon, F. Boy, N. Picot, and C. S., *First SAR altimeter tandem phase: a unique opportunity to better characterize open ocean SAR altimetry signals with unfocused and focused processing,* Ocean Surface Topography Science Team Meeting 2019, 21-25 October 2019 (2019).

[21] F. Collard, F. Ardhuin, and B. Chapron, *Routine monitoring and analysis of ocean swell fields using a spaceborne SAR,* (2009), arXiv:0812.2318 [physics.ao-ph] .

[22] W. R. Alpers, D. B. Ross, and C. L. Rufenach, *On the Detectability of Ocean Surface Waves by Real and Synthetic Aperture Radar,* Journal of Geophysical Research: Oceans **86**, 6481 (1981).

[23] K. Hasselmann and S. Hasselmann, *On the nonlinear mapping of an ocean wave spectrum into a synthetic aperture radar image spectrum and its inversion,* Journal of Geophysical Research: Oceans **96**, 10713 (1991).

[24] D. R. Lyzenga, R. A. Shuchman, J. D. Lyden, and C. L. Rufenach, *SAR imaging of waves in water and ice: Evidence for velocity bunching,* Journal of Geophysical Research: Oceans **90**, 1031 (1985).

[25] K. Hasselmann, R. K. Raney, W. J. Plant, W. Alpers, R. A. Shuchman, D. R. Lyzenga, C. L. Rufenach, and M. J. Tucker, *Theory of synthetic aperture radar ocean imaging: A MARSEN view,* Journal of Geophysical Research: Oceans **90**, 4659 (1985).

[26] V. Kerbaol, B. Chapron, and P. W. Vachon, *Analysis of ERS-1/2 synthetic aperture radar wave mode imagettes,* Journal of Geophysical Research: Oceans **103**, 7833 (1998).

[27] J. E. Stopa, F. Ardhuin, B. Chapron, and F. Collard, *Estimating wave orbital velocity through the azimuth cutoff from space-borne satellites,* Journal of Geophysical Research: Oceans **120**, 7616 (2015).

[28] G. Valenzuela, *Theories for the interaction of electromagnetic and oceanic waves — A review,* Boundary-Layer Meteorology **13**, 61–85 (1978).

[29] M.-H. Rio, S. Mulet, and N. Picot, *Beyond GOCE for the ocean circulation estimate: Synergetic use of altimetry, gravimetry, and in situ data provides new insight into geostrophic and Ekman currents,* Geophysical Research Letters **41**, 8918 (2014).

[30] Y. Quilfen, M. Yurovskaya, B. Chapron, and F. Ardhuin, *Storm waves focusing and steepening in the Agulhas current: Satellite observations and modeling,* Remote Sensing of Environment **216**, 561 (2018).

[31] J. R. E. Lutjeharms, *Three decades of research on the greater Agulhas Current,* Ocean Sci. , 129–147 (2007).

[32] S. Ponce de León and C. Guedes Soares, *Extreme Waves in the Agulhas Current Region Inferred from SAR Wave Spectra and the SWAN Model,* Journal of Marine Science and Engineering **9** (2021), 10.3390/jmse9020153.

[33] Y. Li and A. Chabchoub, *How Currents Trigger Extreme Sea Waves. The Roles of Stokes Drift, Eulerian Return Flow, and a Background Flow in the Open Ocean,* Geophysical Research Letters **51**, e2023GL107381 (2024), e2023GL107381 2023GL107381.

[34] S. Ponce de León, I. R. Young, T. Waseda, and A. R. Osborne, *Extreme Waves,* Journal of Marine Science and Engineering **10** (2022), 10.3390/jmse10050697.

[35] D. Irvine, *Extreme waves in the Agulhas - A case study in wave-current interaction,* Johns Hopkins APL Technical Digest **8** (2013).

[36] H. A. Dijkstra and W. P. M. de Ruijter, *On the Physics of the Agulhas Current: Steady Retroflection Regimes,* Journal of Physical Oceanography **31**, 2971 (2001).

[37] T. Moreau, S. Labroue, S. Labroue, P. Thibaut, L. Amarouche, F. Boy, and N. Picot, *Sensitivity of SAR mode Altimeter to swells: Attempt to explain sub-mesoscale structures (0.1-1 km) seen from SAR,* CryoSat Third User Workshop, Dresden. 12-14 March (2013).

[38] L. Aouf and L. Phalippou, *On the signature of swell for the CryoSat-2 SAR-mode wave data,* Ocean Surface Topography Science Team Meeting 2015, October 19-23 (2015).

[39] C. Bellingham, M. Srokosz, C. Gommenginger, P. Cipollini, and H. Snaith, *Jason-CS SAR mode Sea State Bias Study,* EUMETSAT Invitation to Tender 14/209556 Final Report version 1.0 (2016).

[40] S. Abdalla and L. Dinardo, *Does Swell Impact SWH from SAR Altimetry?* 2016 SAR Altimetry Workshop, La Rochelle, France, 31 October 2017 (2016).

[41] D. Cotton, T. Moreau, M. Naeije, and C. Bellingham, *Study into the Impact of Swell on SAR Altimeter Data,* Tech. Rep. (SCOOP_ESA_D2.7_WP5300, Project reference, 2018).

[42] R. K. Raney, *Synthetic Aperture Imaging Radar and Moving Targets,* IEEE Transactions on Aerospace and Electronic Systems **AES-7**, 499 (1971).

[43] T. Larson, L. Moskowitz, and J. Wright, *A note on SAR imagery of the ocean,* IEEE Transactions on Antennas and Propagation **24**, 393–394 (1976).

[44] W. Alpers and C. Rufenach, *The effect of orbital motions on synthetic aperture radar imagery of ocean waves Altimeter for Sea Monitoring,* IEEE Transactions on 285 Antennas and Propagation **27** (1979), 10.1109/TAP.1979.1142163.

[45] F. Ardhuin, J. Stopa, B. Chapron, F. Collard, M. Smith, J. Thomson, and M. Doble, *Measuring Ocean Waves in Sea Ice Using Sar Imagery: A Quasi-Deterministic Approach Evaluated with Sentinel-1 and in Situ Data,* Remote Sens. Environ. 2016 **189**, 211–222 (2017).

[46] W. Alpers and K. Hasselman, *The Two frequency Microwave Technique for Measuring Ocean - Wave Spectra from an Airplane or Satellite,* Boundary - Layer Meteorology **13**, 215 (1978).

[47] P. Guccione, M. Scagliola, and D. Giudici, *2D Frequency Domain Fully Focused Sar Processing for High PRF Radar Altimeters,* Remote Sens. **10** (2018), 10.3390/rs10121943.

[48] P. B. Hansen, *The Fast Fourier Transform,* Electrical Engineering and Computer Science, Technical Reports. **130** (1991).

[49] G. Engen and H. Johnsen, *SAR-ocean wave inversion using image cross spectra,* IEEE Transactions on Geoscience and Remote Sensing **33**, 1047–1056 (1995).

[50] H. Krogstad, *A Simple Derivation of Hasselmann's Nonlinear Ocean-Synthetic Aperture Radar Transform,* Journal of Geophysical Research **300 97, 2421** (1992), 10.1029/91JC03010.

[51] H. Krogstad, O. Samset, and P. W. Vachon, *Generalizations of the non-linear ocean-SAR transform and a simplified SAR inversion algorithm,* Atmosphere-Ocean **32**, 61–82 (1994).

[52] S. Hasselmann, C. Bruning, K. Hasselmann, and P. Heimbach, *An improved algorithm for the retrieval of ocean wave spectra from synthetic aperture radar image spectra,* J. Geophys. Res. **101** (1996), 10.1029/96JC00798.

[53] J. Schulz-Stellenfleth and S. Lehner, *Spaceborne synthetic aperture radar observations of ocean waves traveling into sea ice,* Journal of Geophysical Research **107** (2002), 10.1029/2001JC000837.

[54] H. Li, A. Mouche, H. Wang, J. Stopa, and B. Chapron, *Polarization Dependence of Azimuth Cutoff From Quad-Pol SAR Images,* IEEE Transactions On Geoscience And Remote Sensing **57**, 9878 (2019).

[55] J. Schulz-Stellenfleth, S. Lehner, and D. Hoja, *A parametric scheme for the retrieval of two-dimensional ocean wave spectra from synthetic aperture radar look cross spectra,* Journal of Geophysical Research **110** (2005), 10.1029/2004JC002822.

[56] B. Chapron, H. Johnsen, and R. Garello, *Wave and wind retrieval from SAR images of the ocean,* Ann. Télécommun. **56**, 682–699 (2001) (2001).

[57] H. Li, D. Hauser, B. Chapron, F. Nouguier, B. Schippers, P. Zhang, J. Yang, and J. He, *Up-to-downwave asymmetry of the CFOSAT SWIM fluctuation spectrum for wave direction ambiguity removal,* IEEE Transactions on Geoscience and Remote Sensing, Institute of Electrical and Electronics Engineers (2021), 10.1109/TGRS.2021.3086483.

[58] F. Jackson, *The physical basis for estimating wave-energy spectra with the radar ocean-wave spectrometer,* Johns Hopkin s APL Technical Digest **8** (1987).

[59] W. Munk, *An Inconvenient Sea Truth: Spread, Steepness, and Skewness of Surface Slopes,* Annual Review of Marine Science **1**, 377 (2009).

[60] *Impact of vertical water particle motions on focused SAR altimetry,* Advances in Space Research **68**, 853 (2021), 25 Years of Progress in Radar Altimetry.

[61] R. E. Carande, *Estimating ocean coherence time using dual-baseline interferometric synthetic aperture radar,* IEEE Trans. Geosci. Remote Sens. **32**, 846–854 (1994).

[62] C. J. Donlon, R. Cullen, L. Giulicchi, P. Vuilleumier, C. R. Francis, M. Kuschnerus, W. Simpson, A. Bouridah, M. Caleno, R. Bertoni, J. Rancaño, E. Pourier, A. Hyslop, J. Mulcahy, R. Knockaert, C. Hunter, A. Webb, M. Fornari, P. Vaze, S. Brown, J. Willis, S. Desai, J.-D. Desjonqueres, R. Scharroo, C. Martin-Puig, E. Leuliette, A. Egido, W. H. Smith, P. Bonnefond, S. Le Gac, N. Picot, and G. Tavernier, *The Copernicus Sentinel-6 mission: Enhanced continuity of satellite sea level measurements from space,* Remote Sensing of Environment **258**, 112395 (2021).

[63] H. Hersbach, B. Bell, P. Berrisford, S. Hirahara, A. Horányi, J. Muñoz-Sabater, J. Nicolas, C. Peubey, R. Radu, D. Schepers, A. Simmons, C. Soci, S. Abdalla, X. Abellan, G. Balsamo, P. Bechtold, G. Biavati, J. Bidlot, M. Bonavita, G. De Chiara, P. Dahlgren, D. Dee, M. Diamantakis, R. Dragani, J. Flemming, R. Forbes, M. Fuentes, A. Geer,

L. Haimberger, S. Healy, R. J. Hogan, E. Hólm, M. Janisková, S. Keeley, P. Laloyaux, P. Lopez, C. Lupu, G. Radnoti, P. de Rosnay, I. Rozum, F. Vamborg, S. Villaume, and J.-N. Thépaut, *The ERA5 global reanalysis,* Quarterly Journal of the Royal Meteorological Society **146**, 1999 (2020).

[64] F. Jackson, W. Walton, B. Walter, and L. Baker, *Aircraft and satellite measurement of ocean wave directional spectra using scanning beam microwave radars,* J. Geophys. Res., Oceans **90**, 987–1004 (1985).

[65] F. Jackson, W. Walton, D. Hines, P. Walter, and C. Peng, *Sea surface mean square slope from ku-band backscatter data,* Journal of Geophysical Research: Oceans (1978-2012) **97**, 11411 (1992).

[66] F. Nouguier, A. Mouche, N. Rascle, B. Chapron, and D. Vandermark, *Analysis of Dual-Frequency Ocean Backscatter Measurements at Ku- and Ka-Bands Using Near-Nadir Incidence GPM Radar Data,* IEEE Geoscience and Remote Sensing Letters **13**, 1310 (2016).

[67] S. Li, D. Zhao, L. Zhou, and B. Liu, *Dependence of mean square slope on wave state and its application in altimeter wind speed retrieval,* International Journal of Remote Sensing **34**, 264 (2013).

[68] O. Phillips, *The Dynamics of the Upper Ocean,* Cambridge University Press (1977).

[69] F. Chapron, K. Katsaros, T. Elfouhaily, and D. Vandemark, *A Note on Relationships between Sea Surface Roughness and Altimeter Backscatter,* Air-Water Gas Transfer (1995).

[70] M. A. Srokosz, *On the joint distribution of surface elevation and slopes for a nonlinear random sea, with an application to radar altimetry,* Journal of Geophysical Research: Oceans **91**, 995 (1986).

[71] B. S. Yaplee, A. Shapiro, D. L. Hammond, B. Au, and E. A. Uliana, *Nanosecond radar observations of the ocean surface from a stable platform,* IEEE Transactions on Geoscience Electronics **9**, 170 (1971).

[72] N. Pires, M. J. Fernandes, C. Gommenginger, and R. Scharroo, *A Conceptually Simple Modeling Approach for Jason-1 Sea State Bias Correction Based on 3 Parameters Exclusively Derived from Altimetric Information,* Remote Sensing **8** (2016), 10.3390/rs8070576.

[73] *Sea state bias in altimetry measurements within the theory of similarity for wind-driven seas,* Advances in Space Research **68**, 978 (2021), 25 Years of Progress in Radar Altimetry.

[74] C. Gommenginger and M. Srokosz, *Sea state bias - 20 years on,* ESA Special Publication, In Danesy, D., editor, ESA Special Publication **614** (2006).

[75] Y. Cheng, Q. Xu, L. Gao, X. Li, B. Zou, and T. Liu, *Sea State Bias Variability in Satellite Altimetry Data,* Remote Sens. **11** (2019), 10.3390/rs11101176.

[76] E. Bronner, A. Guillot, N. Picot, and J. Noubel, *SARAL/AltiKa Products Handbook,* No. CNES: SALP-MU-M-OP-15984-CN (2013).

[77] L.-L. Fu and R. Glazman, *The effect of the degree of wave development on the sea state bias in radar altimetry measurement,* Journal of Geophysical Research: Oceans **96**, 829 (1991).

[78] P. Gaspar, F. Ogor, P.-Y. Le Traon, and O.-Z. Zanife, *Estimating the sea state bias of the topex and poseidon altimeters from crossover differences,* Journal of Geophysical Research: Oceans **99**, 24981 (1994).

[79] J. Guo, H. Zhang, Z. Li, C. Zhu, and X. Liu, *On Modelling Sea State Bias of Jason-2 Altimeter Data Based on Significant Wave Heights and Wind Speeds,* Remote Sensing **15** (2023), 10.3390/rs15102666.

[80] N. Tran, S. Labroue, S. Philipps, B. E., and N. Picot, *Overview and Update of the Sea State Bias Corrections for the Jason-2, Jason-1 and TOPEX Missions,* Marine Geodesy **33**, 348 (2010).

[81] J. Gourrion, D. Vandemark, S. Bailey, B. Chapron, G. P. Gommenginger, P. G. Challenor, and M. A. Srokosz, *A Two-Parameter Wind Speed Algorithm for Ku-Band Altimeters,* Journal of Atmospheric and Oceanic Technology **19**, 2030 (2002).

[82] C. P. Gommenginger, M. A. Srokosz, C. Bellingham, H. Snaith, N. Pires, M. Fernandes, N. Tran, D. Vandemark, T. Moreau, S. Labroue, and R. Scharroo, *Sea state bias: 25 years on,* In Proceedings of the Presentation at and Abstract in: 25 years of progress in radar altimetry, Ponta Delgada, Portugal, 24–29 September 2018. (2018).

[83] A. Egido and C. Ray, *On the Effect of Surface Motion in SAR Altimeter Observations of the Open Ocean,* OSTST 2019,Oct. 21st – 25th, Chicago, IL, USA (2019).

[84] O. Altiparmaki, M. Kleinherenbrink, M. Naeije, C. Slobbe, and P. Visser, *SAR altimetry data as a new source for swell monitoring,* Geophysical Research Letters **49** (2022), 10.1029/2021GL096224.

[85] F. Reale, F. Dentale, E. P. Carratelli, and L. Fenoglio-Marc, *Influence of Sea State on Sea Surface Height Oscillation from Doppler Altimeter Measurements in the North Sea,* Remote Sensing **10** (2018), 10.3390/rs10071100.

[86] C. Buchhaupt, A. Egido, W. H. Smith, and L. Fenoglio, *Conditional sea surface statistics and their impact on geophysical sea surface parameters retrieved from SAR altimetry signals,* Advances in Space Research **71**, 2332 (2023).

[87] Y. Liu, M.-Y. Su, X.-H. Yan, and W. T. Liu, *The Mean-Square Slope of Ocean Surface Waves and Its Effects on Radar Backscatter,* Journal of Atmospheric and Oceanic Technology **17**, 1092 (2000).

[88] F. Nouguier, A. Mouche, N. Rascle, B. Chapron, and D. Vandemark, *Analysis of Dual-Frequency Ocean Backscatter Measurements at Ku- and Ka-Bands Using Near-Nadir Incidence GPM Radar Data,* IEEE Geoscience and Remote Sensing Letters **13**, 1310 (2016).

[89] C. Cox and W. Munk, *Measurement of the roughness of the sea surface from photographs of the sun's glitter,* Journal of the Optical Society of America (1917-1983) **44**, 838 (1954).

[90] C. Cox and W. Munk, *Statistics of the sea surface derived from sun glitter,* Journal of Marine Research 13, (2) (1954).

[91] R. K. Raney, *Wave orbital velocity, fade, and SAR response to azimuth waves,* IEEE Journal of Oceanic Engineering **6**, 140 (1981).

[92] R. C. Beal, D. G. Tilley, and F. M. Monaldo, *Large-and small-scale spatial evolution of digitally processed ocean wave spectra from SEASAT synthetic aperture radar,* Journal of Geophysical Research: Oceans **88**, 1761 (1983).

[93] W. Alpers, C. Bruening, and K. Richter, *Comparison of Simulated and Measured Synthetic Aperture Radar Image Spectra with Buoy-Derived Ocean Wave Spectra During the Shuttle Imaging Radar B Mission,* IEEE Transactions on Geoscience and Remote Sensing **GE-24**, 559 (1986).

[94] G. Grieco, W. Lin, M. Migliaccio, F. Nirchio, and M. Portabella, *Dependency of the Sentinel-1 azimuth wavelength cut-off on significant wave height and wind speed,* International Journal of Remote Sensing **37**, 5086 (2016).

[95] D. R. Lyzenga, *Numerical Simulation of Synthetic Aperture Radar Image Spectra for Ocean Waves,* IEEE Transactions on Geoscience and Remote Sensing **GE-24**, 863 (1986).

[96] M. Kleinherenbrink, F. Ehlers, S. Hernández, F. Nouguier, O. Altiparmaki, F. Schlembach, and B. Chapron, *Cross-Spectral Analysis of SAR Altimetry Waveform Tails,* IEEE Transactions on Geoscience and Remote Sensing **62**, 1 (2024).

[97] F. Ardhuin, E. Rogers, A. Babanin, J. Filipot, R. Magne, A. Roland, A. van der Westhuysen, P. Queffeulou, L. J.M., L. Aouf, and F. Collard, *Semiempirical Dissipation Source Functions for Ocean Waves. Part I: Definition, Calibration, and Validation,* Journal of Physical Oceanography **40**, 1917 (2010).

[98] P. Janssen, L. Aouf, A. Behrens, G. Korres, L. Cavalieri, K. Christiensen, and O. Breivik, *Final report of work-package I in my wave project,* IEEE Transactions on Geoscience and Remote Sensing (2014).

[99] P. Rieu, S. Amraoui, and M. Restano, *Standalone Multi-mission Altimetry Processor (SMAP),* (2021).

[100] S. Amraoui, P. Guccione, T. Moreau, M. Alves, O. Altiparmaki, C. Peureux, L. Recchia, C. Maraldi, F. Boy, and C. Donlon, *Optimal Configuration of Omega-Kappa FF-SAR Processing for Specular and Non-Specular Targets in Altimetric Data: The Sentinel-6 Michael Freilich Study Case,* Remote Sensing **16** (2024), 10.3390/rs16061112.

[101] *Product User Manual For Global Ocean Wave Analysis and Forecasting Product, EU Copernicus Marine Service. Technical report,* (2023), Accessed on: December 2023.

[102] J. Xiong, Y. P. Wang, S. Gao, J. Du, Y. Yang, J. Tang, and J. Gao, *On estimation of coastal wave parameters and wave-induced shear stresses,* Limnology and Oceanography: Methods **16**, 594 (2018).

[103] T. Elfouhaily, B. Chapron, K. Katsaros, and D. Vandemark, *A unified directional spectrum for long and short wind-driven waves,* Journal of Geophysical Research: Oceans **102**, 15781 (1997).

[104] P. W. Vachon, R. B. Olsen, K. H. E., and A. K. Liu, *Airborne synthetic aperture radar observations and simulations for waves in ice,* Geophys. Res., 98 (C9), 16411– 16425 (1993), 10.1029/93JC00914.

[105] G. Engen and H. Johnsen, *A New Method for Calibration of SAR Images,* SAR Workshop: CEOS Committee on Earth Observation Satellites; Working Group on Calibration and Validation, Proceedings of a Conference held 26-29 October 1999, Toulouse, France. Edited by Robert A. Harris and L. Ouwehand. Publisher: Paris: European Space Agency, 2000. ESA-SP vol. 450, ISBN: 9290926414, p.109 (2000).

[106] CORDIS, *MyWave: A pan-European concerted and integrated approach to operational wave modelling and forecasting – a complement to GMES MyOcean services.Technical report,* (2014), Accessed on: December 2023.

[107] G. Marechal and F. Ardhuin, *Surface Currents and Significant Wave Height Gradients: Matching Numerical Models and High-Resolution Altimeter Wave Heights in the Agulhas Current Region,* Journal of Geophysical Research: Oceans **126**, e2020JC016564 (2021), e2020JC016564 2020JC016564.

[108] C. J. Donlon, R. Cullen, L. Giulicchi, P. Vuilleumier, C. R. Francis, M. Kuschnerus, W. Simpson, A. Bouridah, M. Caleno, R. Bertoni, J. Rancaño, E. Pourier, A. Hyslop, J. Mulcahy, R. Knockaert, C. Hunter, A. Webb, M. Fornari, P. Vaze, S. Brown, J. Willis, S. Desai, J.-D. Desjonqueres, R. Scharroo, C. Martin-Puig, E. Leuliette, A. Egido, W. H. Smith, P. Bonnefond, S. Le Gac, N. Picot, and G. Tavernier, *The Copernicus Sentinel-6 mission: Enhanced continuity of satellite sea level measurements from space,* Remote Sensing of Environment **258**, 112395 (2021).

[109] M. Kleinherenbrink, W. H. F. Smith, M. C. Naeije, D. C. Slobbe, and P. Hoogeboom, *The second-order effect of Earth's rotation on CryoSat-2 fully focused SAR processing,* Journal of Geodesy **94(1), [7]** (2020), 10.1007/s00190-019-01337-8.

[110] L. H. Holthuijsen, *Waves in oceanic and coastal waters,* Cambridge: Cambridge University Press (2007), 10.1017/CBO9780511618536.

[111] M. A. Barnes and C. Rautenbach, *Toward Operational Wave-Current Interactions Over the Agulhas Current System,* Journal of Geophysical Research: Oceans **125**, e2020JC016321 (2020).

[112] L. Ren, J. Yang, Q. Xiao, G. Zheng, and J. Wang, *On CFOSAT swim wave spectrometer retrieval of ocean waves,* in *2017 IEEE International Geoscience and Remote Sensing Symposium (IGARSS)* (2017) pp. 1966–1969.

[113] D. E. Irvine and D. G. Tilley, *Ocean wave directional spectra and wave-current interaction in the Agulhas from the Shuttle Imaging Radar-B Synthetic Aperture Radar,* Journal of Geophysical Research: Oceans **93**, 15389 (1988).

[114] Y. Quilfen and B. Chapron, *Ocean Surface Wave-Current Signatures From Satellite Altimeter Measurements,* Geophysical Research Letters **46**, 253 (2019).

[115] M. Krug, A. Mouche, F. Collard, J. A. Johannessen, and B. Chapron, *Mapping the Agulhas Current from space: An assessment of ASAR surface current velocities,* Journal of Geophysical Research: Oceans **115** (2010), 10.1029/2009JC006050.

[116] M. Marghany, *Four-dimensional wave refraction from Sentinel-1A satellite data,* IOP Conference Series: Earth and Environmental Science **169**, 012030 (2018).

[117] V. Kudryavtsev, M. Yurovskaya, B. Chapron, F. Collard, and C. Donlon, *Sun glitter imagery of surface waves. Part 2: Waves transformation on ocean currents,* Journal of Geophysical Research: Oceans **122**, 1384 (2017).

[118] H. Komijani and J. Monbaliu, *The wave-current interaction in the coastal area,* Journal of Marine Research **77** (2019).

[119] S. Pascolo, M. Petti, and S. Bosa, *Wave–Current Interaction: A 2DH Model for Turbulent Jet and Bottom-Friction Dissipation,* Water **10** (2018), 10.3390/w10040392.

[120] T. Halsne, K. H. Christensen, G. Hope, and Ø. Breivik, *Ocean wave tracing v.1: a numerical solver of the wave ray equations for ocean waves on variable currents at arbitrary depths,* Geoscientific Model Development **16**, 6515 (2023).

[121] M. Naeije, K. Wakker, R. Scharroo, and B. Ambrosius, *Observation of mesoscale ocean currents from GEOSAT altimeter data,* ISPRS Journal of Photogrammetry and Remote Sensing **47**, 347 (1992).

[122] J. Rabault, T. Nose, G. Hope, M. Müller, Ø. Breivik, J. Voermans, L. R. Hole, P. Bohlinger, T. Waseda, T. Kodaira, T. Katsuno, M. Johnson, G. Sutherland, M. Johansson, K. H. Christensen, A. Garbo, A. Jensen, O. Gundersen, A. Marchenko, and A. Babanin, *OpenMetBuoy-v2021: An Easy-to-Build, Affordable, Customizable, Open-Source Instrument for Oceanographic Measurements of Drift and Waves in Sea Ice and the Open Ocean,* Geosciences **12** (2022), 10.3390/geosciences12030110.

[123] R. T. Pollard, *Properties of Near-Surface Inertial Oscillations,* Journal of Physical Oceanography **10**, 385 (1980).

[124] K. E. Kenyon, *Stokes drift for random gravity waves,* Journal of Geophysical Research (1896-1977) **74**, 6991 (1969).

[125] Ø. Breivik, P. Janssen, and J. Bidlot, *Approximate Stokes Drift Profiles in Deep Water,* Journal of Physical Oceanography **44**, 2433 (2014).

[126] N. Ferry, E. Rémy, P. Brasseur, and C. Maes, *The Mercator global ocean operational analysis system: Assessment and validation of an 11-year reanalysis,* Journal of Marine Systems **65**, 540 (2007).

[127] L. Aouf, A. Dalphinet, D. Hauser, L. Delaye, C. Tison, B. Chapron, L. Hermozo, and C. Tourain, *On the Assimilation of CFOSAT Wave Data in the Wave Model MFWAM : Verification Phase,* in *IGARSS 2019 - 2019 IEEE International Geoscience and Remote Sensing Symposium* (2019) pp. 7959–7961.

[128] A. Dalphinet, L. Aouf, S. Law-Chune, and M. Tressol, *Product User Manual for Global Ocean Wave Analysis and Forecasting Product, EU Copernicus Marine Service (technical report),* (2023), Accessed on: December 2023.

[129] M. G. Hart-Davis, B. C. Backeberg, I. Halo, E. van Sebille, and J. A. Johannessen, *Assessing the accuracy of satellite derived ocean currents by comparing observed and virtual buoys in the Greater Agulhas Region,* Rem Sens Env **216**, 735 (2018).

[130] A. H. Murphy, *Skill Scores Based on the Mean Square Error and Their Relationships to the Correlation Coefficient,* Monthly Weather Review **116**, 2417 (1988).

[131] J. Lellouche, O. Le Galloudec, C. Regnier, S. Van Gennip, S. Law Chune, B. Levier, E. Greiner, M. Drevillon, and C. Szczypta, *Mercator Quality Information Document,* (2023), Accessed on: April 2023.

[132] F. Ardhuin, L. Marié, N. Rascle, P. Forget, and A. Roland, *Observation and Estimation of Lagrangian, Stokes, and Eulerian Currents Induced by Wind and Waves at the Sea Surface,* Journal of Physical Oceanography **39**, 2820 (2009).

[133] J. Rabault, M. Müller, J. Voermans, D. Brazhnikov, I. Turnbull, A. Marchenko, M. Biuw, T. Nose, T. Waseda, M. Johansson, Ø. Breivik, G. Sutherland, L. R. Hole, M. Johnson, A. Jensen, O. Gundersen, A. Babanin, P. Tedesco, K. H. Christensen, M. Kristiansen, G. Hope, T. Kodaira, V. de Aguiar, C. Taelman, C. P. Quigley, K. Filchuk, and A. R. Mahoney, *A Dataset of Direct Observations of Sea Ice Drift and Waves in Ice,* Sci. Data (2023), 10.1038/s41597-023-02160-9.

[134] A. J. Clarke and S. Van Gorder, *The Relationship of Near-Surface Flow, Stokes Drift and the Wind Stress,* Journal of Geophysical Research: Oceans **123**, 4680 (2018).

[135] Ø. Breivik, J.-R. Bidlot, and P. A. Janssen, *A Stokes drift approximation based on the Phillips spectrum,* Ocean Modelling **100**, 49 (2016).

[136] H. Rapizo, T. Durrant, and A. Babanin, *An assessment of the impact of surface currents on wave modeling in the Southern Ocean,* Ocean Dynamics **68** (2018), 10.1007/s10236-018-1171-7.

[137] P. Bohlinger, Ø. Breivik, T. Economou, and M. Müller, *A novel approach to computing super observations for probabilistic wave model validation,* Ocean Modelling **139**, 101404 (2019).

[138] Copernicus Sentinel-1, *Sentinel-1 Mission - Sentinel Online,* (2024), Accessed on: October 2024.

[139] AVISO, *CFOSAT - Instruments: SWIM,* (2024), Accessed on: October 2024.

[140] O. Altiparmaki, S. Amraoui, M. Kleinherenbrink, T. Moreau, C. Maraldi, P. N. A. M. Visser, and M. Naeije, *Introducing the Azimuth Cutoff as an Independent Measure for Characterizing Sea-State Dynamics in SAR Altimetry,* Remote Sensing **16** (2024), 10.3390/rs16071292.

Curriculum Vitæ

Ourania ALTIPARMAKI

25-11-1992 Born in Mytilini, Lesvos, Greece

Education

2020–2024 **PhD in Space Oceanography | Remote Sensing**
Delft University of Technology, The Netherlands
Thesis: Unlocking the Imaging Capabilities of Synthetic Aperture Radar Altimetry for Ocean Applications

2015–2017 **MSc in Geoinformatics**
Aristotle University of Thessaloniki, Greece
Thesis: CryoSat-2 SAR and SARIn contribution to height system unification and vertical datum optimization in Greece

2010–2015 **Diploma (Integrated Master's) in Rural and Surveying Engineering**
Aristotle University of Thessaloniki, Greece
Thesis: Study of deformation of the Earth's crust through GPS measurements in geodetic networks in the area of Thessaloniki

2007–2010 **Lyceum Apolytirio**
5th General Lyceum of Mytilini, Greece

2004–2007 **Gymnasium Apolytirio**
5th General Gymnasium of Mytilini, Greece

Work experience

2020-2024	**PhD Researcher** Department of Space Engineering, Delft University of Technology, The Netherlands
2021-2023	**Teaching assistant** Department of Space Engineering, Delft University of Technology, The Netherlands
2019–2020	**Geodetic Engineer** Seabed B.V., The Netherlands
2017–2018	**Research assistant** Department of Geodesy and Surveying, Aristotle University of Thessaloniki, Greece

Professional membership

2021-present	**Member of the Ocean Surface Topography Science Team (OSTST)** Research on radar remote sensing techniques and validation activities for Level-2 operational and experimental oceanographic products
2020	**Member of the ESA FFSAR Altimetry Validation Working Group** Involved in validation activities for Level-2 water level products from the "fully-focused SAR CryoSat-2" processor, available on ESA's EarthConsole Altimetry Virtual Lab

List of publications

Peer-reviewed journal publications

1. **Altiparmaki, O.**, Breivik ,O., Aouf, L., Bohlinger, P., Johannessen, J.A., Collard, F., Donlon, C., Hope, G., Visser, P.N.A.M., Naeije, M. (2024). *Influence of Ocean Currents on Wave Modeling and Satellite Observations: Insights from the One Ocean Expedition.* Journal of Geophysical Research:Oceans,129,e2024JC021581

2. **Altiparmaki, O.**, Amraoui, S., Kleinherenbrink, M., Moreau, T., Maraldi, C., Visser, P.N.A.M., Naeije, M. (2024). *Introducing the Azimuth Cutoff as an Independent Measure for Characterizing Sea-State Dynamics in SAR Altimetry.* Remote Sens. 2024, 16, 1292

3. Amraoui, S., Guccione, P., Moreau, T., Alves, M.,**Altiparmaki, O.**, Peureux, C., Recchia, L., Maraldi, C., Boy, F., Donlon, C. (2024).*Optimal Configuration of Omega-Kappa FF-SAR Processing for Specular and Non-Specular Targets in Altimetric Data: The Sentinel-6 Michael Freilich Study Case (2024).* Remote Sensing. 2024; 16(6):1112

4. Kleinherenbrink, K., Ehlers, F., Her/nández, S., Nouguier, F., **Altiparmaki, O.**, Schlembach, F., Chapron B. (2023).*Cross-Spectral Analysis of SAR Altimetry Waveform Tails,*IEEE Transactions on Geoscience and Remote Sensing, vol. 62, pp. 1-15, 2024, Art no. 4206615

5. **Altiparmaki, O.**, Kleinherenbrink, M., Naeije, M. C., Slobbe, D. C., Visser, P.N.A.M. (2022). *SAR altimetry data as a new source for swell monitoring.* Geophysical Research Letters, 49, e2021GL096224

Selected conference contributions

1. **Altiparmaki, O.**, Aouf, L., Rodet, L., Moreau, T., Maraldi, C., Naeije, M. (2024). *Enhancing Global Swell Monitoring through Synergistic Use of Satellite Observations from SAR Altimeters, Sentinel-1 and CFOSAT*. Presented at the 8th Workshop on Advanced RF Sensors and Remote Sensing Instruments, 4-6 November 2024, ESA-ESTEC, Noordwijk, Netherlands. Oral presentation in “Peformance” session

2. **Altiparmaki, O.** (2024). *Advancing Sea-State Characterization with fully-focused SAR Altimetry: Insights and Innovations.* Presented at the 30 Years of Progress in Radar Altimetry Symposium, 2-7 September 2024, Montpellier, France. Poster presentation in “S3 - S6 VT: The latest in Instrument Processing (Altimeter SAR and Radiometer)” session

3. Rodet, L., Moreau, T., **Altiparmaki, O.**, Ehlers, F., Maraldi, C., Boy, F., Picot, N. (2024). *Swell characterization from Sentinel-3 and Sentinel-6MF SAR altimetry data.* Presented at the 30 Years of Progress in Radar Altimetry Symposium, 2-7 September 2024, Montpellier, France. Oral presentation in “S3 - S6 VT: The latest in Instrument Processing (Altimeter SAR and Radiometer)” session

4. Rodet, L., Moreau, T., Piras, F., Ferrer, E., Gassot, O., **Altiparmaki, O.**, Buschhaupt, C., Maraldi, C., Boy, F., Picot, N. (2024). *New processing capabilities in the SPP chain for improving wave characterization from Sentinel-3 and Sentinel-6MF mission data.* Presented at the 30 Years of Progress in Radar Altimetry Symposium, 2-7 September 2024, Montpellier, France. Poster presentation in "S3 - S6 VT: The latest in Instrument Processing (Altimeter SAR and Radiometer)" session
5. Maraldi, C., Rodet, L., **Altiparmaki, O.**, Moreau, T. (2024). *SAR altimetry for swell detection.* Poster presentation in the WInd Waves in the Earth System (WISE) Meeting, 21-27 April 2024, Corsica, France
6. **Altiparmaki, O.**, Amraoui, S., Kleinherenbrink, M., Naeije, M., Moreau, T., Maraldi, C. (2023). *Estimating vertical velocity variances from fully-focused SAR altimetry.* Presented at the Ocean Surface Topography Science Meeting (OSTST) 2023, 7–11 November, 2023, San Juan, Puerto Rico. Oral presentation in "Instrument Processing: Measurement and Retracking" session
7. **Altiparmaki, O.**, Kleinherenbrink, M., Naeije, M. C., Slobbe, D. C., Visser, P. N. A. M. (2022). *Swell detection from fully-focused SAR altimetry data.* Presented at the Ocean Surface Topography Science Meeting (OSTST) 2022, 31 October – 4 November, 2022, Venice, Italy. Oral presentation in "Instrument Processing: Measurement and Retracking" session
8. **Altiparmaki, O.**, Kleinherenbrink, M., Naeije, M. C., Slobbe, D. C., Visser, P. N. A. M. (2022). *Swell detection from fully-focused SAR altimetry data: A Sentinel-6A case study.* Presented at the Living Planet Symposium 2022, 23-27 May, 2022, Bonn, Germany. Poster presentation in "A8.14 Remote-sensing of Ocean Waves and their Applications" session
9. Scagliola, M., **Altiparmaki, O.**, Bercher, L., Fenoglio-Marc, L., Nielsen, K., Passaro, M., Restano, M., Abis, B., Fornari., M., Sabatino, G., Benveniste, J. (2021). *Aresys FF-SAR Service for CryoSat-2 at ESA GPOD.* Presented at the CryoSat 10th Anniversary Conference 2021, 14-18 June, 2021, online
10. Nielsen, K., **Altiparmaki, O.**, Fenoglio-Marc, L., Passaro, M., Bercher, L., Scagliola, M., Abis, B., Fornari., M., Restano, M., Benveniste, J. (2021). *A New Fully-Focused SAR Altimetry Processor in the ESA G-POD SARvatore Family: Validation and Applications on Inland Waters.* Presented at the HYDROSPACE-GEOGloWS 2021, 7-11 June, 2021, Virtual Event from ESA-ESRIN, Frascati, Italy

Acknowledgements

Looking back on this journey, one of the longest and most exciting so far, I realize how many people have stood by me along the way. Finding the right words to express my gratitude has not been easy, but I hope I have chosen them well, as this chapter is dedicated to everyone who, in one way or another, helped make the road less heavy, the challenges more bearable and the good moments even more special.

I would like to start by expressing my gratitude to the ones who made this journey possible in the first place: my supervisory team, Pieter and Marc. I am deeply thankful to both of you for selecting me and for trusting me throughout this project. I want to thank you for fully supporting my side research activities, which I deeply believe have shaped not only my work but also myself as a researcher. Marc, beyond all these, I want to thank you for your unique supervisory approach, your endless support and the freedom you gave me to pursue my research. Most of all, I am especially grateful for the way you cared about me not only as a PhD candidate but also as Rania from day one.

Beyond my supervisory team, I would like to acknowledge Marcel Kleinherenbrink for his insightful contributions to my work. Although not officially my supervisor, working with you often felt like having a third one. Your input consistently brought new perspectives that helped me rethink and better understand complex concepts. The endless hours spent discussing, and especially challenging my results, pushed me beyond my comfort zone and helped me grow as a researcher.

Next, I would like to thank Ejo (Ernst Schrama), not only for reviewing my dissertation, but also for trusting me to co-supervise a master's thesis. I learned a lot from this experience and I am truly grateful for the opportunity. Special thanks also go to Erwin for all the advice throughout this journey and for helping me add the final touch to my thesis cover.

During my PhD, I had the privilege of collaborating with people outside TU Delft who undoubtedly shaped my research. In 2022, I conducted a research visit at CLS under the supervision of Thomas Moreau, where I also had the chance to work closely with colleagues from CNES. Thomas, thank you for your warm welcome and for integrating me into your team as an equal member, despite my short stay. I learned a lot from our discussions and truly appreciated your openness throughout. A special thank you goes to Claire Maraldi from CNES. Every meeting with you until today has been a pleasure.

Among the people I met during this research visit, I want to dedicate a few lines to someone whose presence meant a lot and with whom a professional connection quickly turned into a personal one: Samira. You already know that I have not found the right words to thank you for your unwavering support during my time in France. Your patience in explaining even the most complex concepts as if they were simple was truly invaluable. But above all, the friendship we built is the most lasting gift I took from there.

In 2023, I had the pleasure of meeting Øyvind Breivik aboard a sailing ship in the In-

dian Ocean, while participating in the One Ocean Expedition. This meeting ended up shaping one third of my PhD thesis. Øyvind, I feel truly fortunate that our paths crossed. Your openness to collaborate and your invitation for a research visit at MET later played a significant role in my work. Your ability to clarify aspects of oceanography that had previously felt blurry and your positive attitude not only accelerated my progress, but also sparked an unexpected passion for a topic I had not imagined exploring during my PhD.

Around the same time, I was lucky to have Lotfi Aouf from Météo-France join my PhD journey. Although we only briefly met at the Living Planet Symposium in 2022 in Bonn, I knew right away that I wanted to work with you. Your readiness to offer help, your energy and enthusiasm meant a great deal to me. I am really glad we had the chance to collaborate closely during the final year of my PhD and I am quite sure this is only the beginning.

I want also to acknowledge some wonderful people from the altimetry community, those familiar faces I was always happy to see at conferences. You made technical sessions feel lighter and the whole experience a lot more fun. Marco, Alejandro, Anna, Filomena, Salvatore, Laetitia, Christopher, Alessandro, and many others who will recognize yourselves among this crew: thank you for the advice, the laughs and for making conferences far less stressful and full of great memories every single time we met. And Marco (Fornari): thanks not just for the great company and laughs, but also for the much-needed RAW data support. Speaking of RAW data, I would also like to thank Remko Scharroo from EUMETSAT for making access to it feel far less mysterious.

These years would not have been nearly as fun (and survivable) without some truly amazing people I met along the way, people who made the chaos a lot more manageable and the journey a lot more enjoyable. Sam and Livio, we started and finished our PhD almost side by side. It always felt like we had our own secret language — one hug could say it all and in moments of panic, we were always perfectly in sync! Rewa, you are one of the kindest and most grounded people I know. Thank you for being there every single moment I needed you. Andrea, thank you for bringing just the right amount of chaos when things got too quiet. And no, you are not getting rid of me anytime soon, deal with it. Natalia, thank you for our endless chats and for not working too close to me, because our coffee breaks would have lasted forever. Yaël, you made me realize a bunch of things, but the one I needed most was not to take things so seriously — even when I swore I had to. You being there meant a lot, though I suspect you already knew that. Fernando, Michal, Linh, Caroline, Allard and Sabin, I have so many good memories with each of you. It is impossible to fit them all here, but thank you for the fun, the support and all the good vibes. Looking forward to more reasons to celebrate together — deadlines optional, good food mandatory! I can only hope I will always have colleagues who become friends, like you guys.

It also feels important to honor some truly special people whose presence has been a constant in my life. Marina, Kassiani, Parsec, Marania, Ioanna and Labrini — you have been by my side for over 15 years, and thankfully, we are still counting. Even though we have spent most of our friendship apart, I have never once felt far from you. Thank you for being there through it all and for checking in on my well-being and progress more often than I ever found the courage to bring it up myself.

Some contributions are silent yet invaluable. My deepest gratitude goes to someone whose presence truly shaped this journey. Dimitri, I have thought a lot about how to put this into words, but nothing seems quite enough. Your encouragement and steady presence helped carry me through more than you probably believe. Your support is woven into every page of the dissertation (hopefully the quality lives up to it!), and for that, I will always be grateful.

It would not feel right to end this chapter without mentioning the ones who matter most to me. Vasia, you are the sister everyone wishes they had. You have taught me more than you will ever realize, just by being yourself. Mum, if I had to thank you for one thing, it would be for encouraging me to spread my wings and find my own way, always knowing you were right there beside me. I miss you both every single day, but I find comfort in knowing that, no matter what, you are always there with open arms when I need you the most.

Ευχαριστώ!

Ourania Altiparmaki
Delft, March 2025